technische universität
dortmund

MAX PLANCK INSTITUTE
OF MOLECULAR PHYSIOLOGY

Tissue-intrinsic control of AVE differentiation in stem cell models

Sina Schumacher

Fakultät für Chemie und Chemische Biologie
Technische Universität, Dortmund

Zur Erlangung des akademischen Grades eines
Doktors der Naturwissenschaften (Dr. rer. nat.)

April 2024

Declaration

Vorgelegt im April 2024

von Sina Schumacher

Gutachter:

Prof. Dr. Philippe Bastiaens

Prof. Dr. Britta Trappmann

The work presented in this thesis
was performed in the group of Dr. Christian Schröter
at the Department of Systemic Cell Biology, Max Planck Institute of Molecular Physiology,
Dortmund, Germany

Sina Schumacher was affiliated
to the International Max Planck Research School for Living Matter,
Dortmund, Germany

The work described in this thesis has been partly included in the following publication:

Schumacher, S., Fernkorn, M., Marten, M., Chen, R., Kim, Y.S., Bedzhov, I., Schröter, C. (2023): Tissue-intrinsic beta-catenin signals antagonize Nodal-driven AVE differentiation. bioRxiv doi: 10.1101/2023.05.19.541432

Abstract

Differentiation and patterning in the early mammalian embryo depend on interactions between embryonic and extraembryonic lineages. One critical cell population specified through these interactions is the anterior visceral endoderm (AVE). Situated within the visceral endoderm (VE), the AVE serves as a pivotal signaling center during embryonic development by determining the body axis, ultimately positioning the head and tail within the underlying epiblast (Epi).

The prevailing model for AVE differentiation in the mouse embryo posits that the AVE is induced by a uniform signal from the Epi, but an external inhibitory gradient from another extraembryonic tissue restricts its formation to a specific location beyond the gradient. In this thesis, I used mouse embryonic stem cells to establish an embryo-like aggregate system that challenged this model for AVE differentiation. These aggregates consist of an inner Epi core surrounded by a VE layer, thus resembling the embryo around the time of AVE formation but lacking the external gradient for AVE restriction. Remarkably, contrary to the established model, these aggregates manifest a spatially restricted AVE region within their VE compartment. Through single-cell RNA sequencing data analysis, I identified Nodal signaling as the critical signal from the Epi inducing AVE formation in the outer VE. Building upon this discovery, I initiated AVE differentiation in a homogeneous culture of VE cells, resulting in the development of a 2D AVE model. Activation of Nodal signaling within this model led to the formation of spatially constrained AVE clusters, unveiling a novel intrinsic mechanism within VE cells for spatially regulating AVE differentiation. To delineate the signal antagonizing AVE differentiation, I explored the role of different signaling networks in this tissue-intrinsic mechanism and identified β-catenin as the counteracting signal for AVE differentiation.

Together, the findings shed light on an unexplored aspect of self-organization in AVE differentiation, potentially complementing the existing model of an inhibitory gradient mechanism in AVE formation.

Zusammenfassung

Die Differenzierung und Musterbildung im frühen Säugetierembryo werden durch Interaktionen zwischen embryonalen und extraembryonalen Zelllinien koordiniert. Eine entscheidende Zellpopulation, die aus einer solchen Interaktion resultiert, ist das anteriore viszerale Endoderm (AVE). Das AVE bildet sich innerhalb des viszeralen Endoderms und fungiert als wichtiges Signalzentrum während der Embryonalentwicklung, indem es die Körperachse festlegt und die zukünftigen Regionen für Kopf und Schwanz im Epiblasten (Epi) positioniert.

Das vorherrschende Modell der AVE-Differenzierung im Mausembryo besagt, dass das AVE durch ein uniformes Signal aus dem Epi induziert wird. Allerdings wird seine Bildung durch einen externen inhibierenden Gradienten von einem anderen extraembryonalen Gewebe an einen bestimmten Ort begrenzt. In dieser Arbeit habe ich murine embryonale Stammzellen verwendet, um ein Aggregatsystem zu etablieren, das dieses Modell der AVE-Differenzierung herausfordert. Diese Aggregate bestehen aus einem inneren Epi-Kern, der von einer VE-Schicht umgeben ist und somit dem Embryo um die Zeit der AVE-Bildung ähnelt, jedoch den externen Gradienten für die AVE-Restriktion nicht aufweist. Bemerkenswerterweise zeigen diese Aggregate entgegen dem etablierten Modell eine räumlich begrenzte AVE-Region innerhalb ihrer VE-Schicht. Mithilfe der Einzelzell-RNA-Sequenzierung konnte ich Nodal als entscheidendes Signal aus dem Epi identifizieren, welches die AVE-Bildung im äußeren VE induziert. Unter Nutzung dieser Erkenntnis habe ich die AVE-Differenzierung in einer reinen Kultur von VE-Zellen induziert und so ein 2D-AVE-Modell entwickelt. Die Aktivierung des Nodal-Signalwegs in diesem Modell führte zur Bildung von AVE-Clustern, was auf einen neuartigen gewebespezifischen Mechanismus der VE-Zellen hinweist, der die AVE-Differenzierung räumlich begrenzt. Um das Signal zu bestimmen, das der AVE-Differenzierung entgegenwirkt, habe ich die Rolle verschiedener Signalnetzwerke in diesem Modell untersucht und β-Catenin als den gewebespezifischen Gegenspieler der AVE-Differenzierung identifiziert.

Zusammenfassend tragen diese Ergebnisse dazu bei, einen bisher unerforschten Aspekt der Selbstorganisation in der AVE-Differenzierung aufzudecken, der das bestehende Modell eines inhibierenden Gradientenmechanismus in der AVE-Bildung potenziell ergänzen könnte.

Table of Contents

Declaration II

Abstract III

Zusammenfassung IV

List of Figures VII

1 Introduction 1

1.1 Early mouse embryonic development 2
1.1.1 Development into the peri-implantation embryo 2
1.1.2 Patterning in the post-implantation embryo 4

1.2 Signaling in the post-implantation embryo 5
1.2.1 Nodal and BMP4 signaling pathways 6
1.2.2 Wnt/β-catenin signaling 7
1.2.3 Nodal and BMP antagonism mediates AVE differentiation 9

1.3 Patterning mechanisms in the embryo 11
1.3.1 Positional information in a gradient 12
1.3.2 Self-organization 14

1.4 Model systems to study post-implantation development 16
1.4.1 Derivation of stem cells 16
1.4.2 Post-implantation embryo models 18

1.5 Objectives 21

2 Methods 23

2.1 Cell lines and cultivation 23

2.2 Embryos 23

2.3 Mutant and transgenic cell lines 23
2.3.1 Mutant cell lines 23
2.3.2 H2B-Cerulean label 25
2.3.3 Cer1:H2B-Venus reporter 25

2.4 Formation of Epi cysts 26

2.5 Formation of BELAs 26

2.6 Formation of VE cysts 27

2.7 AVE differentiation 27

2.8 Immunocytochemistry 28

2.9 In situ HCR 29

2.10 Sytox stain 29

2.11 Imaging 30

2.12 Computational staining analysis 30

2.13 Flow cytometry 31

2.14 Single-cell RNA sequencing 32
2.14.1 Sample preparation and collection of single cells 32
2.14.2 Library preparation and sequencing 32
2.14.3 Single cells RNA sequencing data analysis 33

2.14.4 Cell-cell communication analysis 34
2.15 Statistics 34
3 Results 36
3.1 Bilayered embryo-like aggregates (BELAs) 36
3.1.1 Mixtures of Epi and PrE cells spontaneously form organized aggregates 36
3.1.2 Bilayered aggregates resemble part of the peri-implantation embryo 38
3.2 Epi and PrE cells exchange signals for survival and morphogenesis 39
3.2.1 PrE cells depend on FGF4 from the Epi 39
3.2.2 Epi cells require binding to extracellular matrix 42
3.3 scRNA seq reveals AVE differentiation in BELAs 45
3.3.1 VE cells segregate potential AVE cluster 46
3.3.2 AVE cells from BELAs resemble transcriptome of an E6.25 AVE 48
3.3.3 AVE marker expression is spatially restricted in BELAs 49
3.4 Nodal is necessary and sufficient for AVE differentiation 51
3.4.1 Inhibition or mutation of Nodal abrogates AVE differentiation 51
3.4.2 Addition of ActivinA during VE induction triggers AVE differentiation 53
3.4.3 Nodal and Lefty1 have only minor effects in spatial restriction of AVE cells 56
3.5 A new counteracting signal for AVE differentiation 58
3.5.1 BMP4 exhibits only mild effects on AVE differentiation 58
3.5.2 Tissue-intrinsic Wnt/β-catenin signals counteract AVE differentiation 60
3.5.3 Cell density can influence AVE differentiation 63
3.6 β-catenin acts independently of Wnt ligands 65
3.6.1 Mutation of single Wnt ligands does not affect AVE differentiation 65
3.6.2 Abrogating Wnt ligand secretion does not affect AVE differentiation 67
3.7 Effects of mechanical perturbations on AVE differentiation 70
3.7.1 E-cadherin is upregulated in cell junctions upon ActivinA treatment 70
3.7.2 Blocking of E-cadherin binding sites promotes AVE differentiation 71
3.7.3 Lowering cell contractility promotes AVE differentiation 73
4 Discussion 77
4.1 Establishment of an embryo-like aggregate model 77
4.2 AVE differentiation in BELAs 79
4.3 A 2D AVE differentiation system 81
4.4 Signaling control of spatially restricted AVE differentiation 82
4.4.1 The effect of BMP on AVE differentiation 82
4.4.2 Nodal and Lefty as activator-inhibitor pair 84
4.4.3 β-catenin as new antagonist for AVE differentiation 85
4.5 Conclusions and future directions 87
5 References 90
6 Acknowledgements 100
7 Eidesstattliche Versicherung 102

List of Figures

Figure 1: Development of a mouse embryo form fertilization to implantation. 3
Figure 2: Formation of the anterior visceral endoderm (AVE). 5
Figure 3: TGF-β (Nodal and BMP4) signaling network. 7
Figure 4: The role of β-catenin in Wnt signaling and cell adhesion. 9
Figure 5: Model for AVE induction. 11
Figure 6: Positional information model. 13
Figure 7: Mouse and human embryos in comparison. 13
Figure 8: The principles of reaction-diffusion. 15
Figure 9: Derivation of mouse embryonic stem cells. 17
Figure 10: Epi and PrE cells spontaneously form aggregates. 37
Figure 11: Aggregates resemble Epi and VE compartment of the peri-implantation embryo. 39
Figure 12: Epi and PrE cells exchange mutual survival signals. 40
Figure 13: Induced PrE cells spontaneously organize into VE cysts. 41
Figure 14: VE cysts are BELAs without the inner Epi core. 41
Figure 15: Validation of *Itgb1* mutant mESCs. 42
Figure 16: *Itgb1* mutant Epi cells show extensive cell death in BELAs. 43
Figure 17: Integrin plays an important role in patterning the Epi cells. 44
Figure 18: Single cell RNA seq of BELAs and its single compartments. 45
Figure 19: VE cells do not sort based on their origin. 46
Figure 20: scRNA seq identifies an AVE cluster within VE cells. 47
Figure 21: BELA-VE predominantly represents embryonic Epi-VE and AVE from E6.25. 48
Figure 22: Spatially restricted AVE markers are transiently expressed. 50
Figure 23: AVE reporter cell line shows spatially restricted AVE cells in BELAs. 51
Figure 24: BELAs fail to form an AVE in the presence of Nodal inhibitor. 52
Figure 25: *Nodal* mutant BELAs fail to form an AVE. 53
Figure 26: Nodal/Activin signals are sufficient for AVE differentiation. 54
Figure 27: AVE comparison in mouse embryo, BELA and 2D VE. 55
Figure 28: *Nodal* mutation in VE cells affects Cer1 reporter, but not OTX2 expression 57
Figure 29: *Lefty1* mutation does not lead to increased AVE induction. 58
Figure 30: No evidence for BMPs tissue intrinsic restriction of AVE differentiation. 59
Figure 31: Mouse embryo with TCF/Lef:H2B-GFP reporter expression in the VE. 60
Figure 32: Tissue intrinsic Wnt/β-catenin signaling counteracts AVE differentiation. 61
Figure 33: GATA6 expression is independent of ActivinA and Wnt/β-catenin signaling. 62
Figure 34: Cell density influences AVE differentiation. 64

Figure 35: Expression of Wnt ligands in BELAs. 66
Figure 36: Mutation of *Wnt4* and *Wnt11* cannot recapitulate the phenotype of XAV. 67
Figure 37: Validation of *Porcn* mutation phenotype. 68
Figure 38: Mutation of *Porcn* indicates Wnt ligand independent β-catenin signaling. 69
Figure 39: Cells in AVE nests seem to have stronger cell-cell adhesion. 71
Figure 40: E-cadherin blocking antibody increases number of AVE cells. 72
Figure 41: Blebbistatin increases number of AVE cells. 76

1 Introduction

To understand how an embryo develops is a huge intellectual challenge that has intrigued thinkers throughout history. In the fourth century BC, the Greek philosopher Aristotle proposed early ideas about how embryos develop (Zagris, 2022). He discussed two main theories: preformation, which suggested that all structures of the embryo were preformed from the very beginning and simply needed to grow larger during development; and epigenesis, which proposed that different structures of the embryo would arise sequentially. Although epigenesis would later be validated as the correct theory, the concept of preformation persisted until the nineteenth century. The discovery of cells as the basic unit of life and the realization that new cells are continually formed during development by division of preexisting cells shifted the focus towards epigenesis (Müller-Wille, 2010; Wolpert et al., 2019).

Today, we understand that the embryo is formed from a single fertilized egg cell, and as Aristotle correctly described, the ontogenetic structures are not preformed in the egg. Instead, cells gradually acquire distinct specialized functions and structures as the embryo progresses. To organize the different structures of the developing embryo, the formation of body axes is crucial during development. These axes help determine the orientation and positioning of various body parts, such as the head and tail. Notably, the formation of the head-to-tail axis is an important developmental process that occurs early in development.

The formation of the head-to-tail axis has been extensively studied in various model organisms, such as the fly. However, the process by which mammals, including humans, establish the anterior-posterior axis is less understood. In mammals, this axis is established by a small signaling center known as the anterior visceral endoderm (AVE) (Stower & Srinivas, 2018). Therefore, to understand how the axis is established in mammals, one must investigate the formation of the AVE.

1.1 Early mouse embryonic development

1.1.1 Development into the peri-implantation embryo

The early stages of mouse embryonic development are a complex and highly regulated process that begins with fertilization of the egg cell and culminates in the formation of the blastocyst which implants into the uterus. These initial phases are characterized by intricate cell divisions and differentiation events, laying the foundation for the embryonic lineage, which ultimately gives rise to the entire embryo. Simultaneously, two supporting extraembryonic lineages are formed, playing vital roles in shaping and organizing the embryonic lineage, albeit without directly contributing to the embryo proper (Saiz & Plusa, 2013).

Following fertilization of the egg cell, the zygote undergoes cleavage, rounds of divisions to produce smaller blastomeres in its protective proteinaceous shell (zona pellucida, Figure 1). After three rounds, the embryo reaches the eight-cell stage at E2.5 and undergoes a process called compaction in which the blastomeres change from a rather lose (grape-like) to a compact arrangement (mulberry-like) by tightening of cell-cell adhesion via E-cadherin (Turlier & Maître, 2015). Following another round, the first lineage bifurcation takes place. At E3.0, the outer-residing cells give rise to the extraembryonic trophectoderm (TE) and the inner cells form the inner cell mass (ICM) (Mihajlović & Bruce, 2017). Decedents of TE cells will later mediate contact from the embryo to the uterus wall of the mother essential for implantation and will also contribute to the embryonic part of the placenta (Bevilacqua & Abrahamsohn, 1989).

At E3.5 through the process of cavitation, the morula transforms into the fluid-filled blastocyst (early blastocyst, Figure 1) (Kim & Bedzhov, 2022). The water influx is required for the embryo to hatch from the zona pellucida necessary for directly contacting the maternal tissue and also for creating the first asymmetry in the embryo by pushing the ICM towards one pole of the blastocysts. The ICM then undergoes the second lineage bifurcation in an FGF4-dependend manner and gives rise to the embryonic epiblast (Epi), that will form the embryo proper, and to the primitive endoderm (PrE), the second extraembryonic tissue, that will influence the inner Epi in patterning and differentiation and will later form the yolk sac (Simon et al., 2018). The Epi and PrE

cells first arise in a salt and pepper like pattern and then sort into distinct layers with the PrE facing the cavity (late blastocyst, Figure 1). Having completed the formation of embryonic lineage Epi and the two extraembryonic lineages TE and PrE in the blastocyst, the embryo is ready to implant into the uterus at around E4.5.

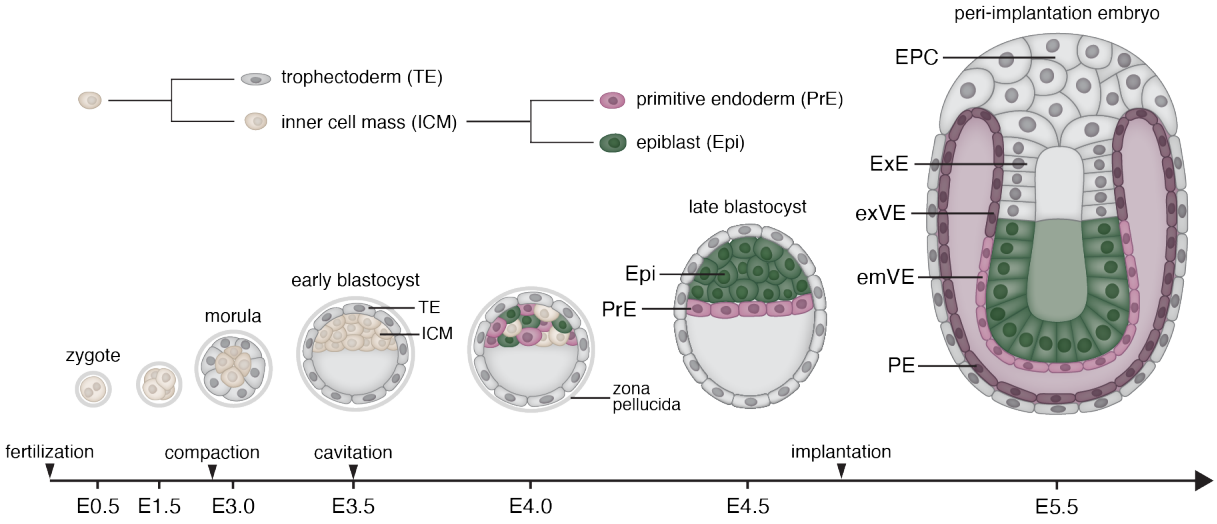

Figure 1: Development of a mouse embryo form fertilization to implantation.
Before implantation, the fertilized egg cell (zygote) undergoes cleavage and two cell lineage bifurcations to form the liquid-filled blastocyst. First, the blastomeres compact and the outer cells give rise to the extraembryonic trophectoderm (TE), while the inner cells become the inner cell mass (ICM). Following cavitation and formation of the blastocyst, the ICM undergoes the second lineage bifurcation into embryonic epiblast (Epi) and the extraembryonic primitive endoderm (PrE). Initially, the two cell types arise in a salt and pepper like pattern but then sort so that the PrE cells form a border between the Epi cells and the cavity. The embryo hatches form the zona pellucida and during implantation undergoes a massive shape change. The TE cells further divide and form the ectoplacental cone (EPC) and ExE on one side of the embryo. The PrE cells migrate and cover as parietal visceral endoderm the TE cells and the ExE and Epi cells as extraembryonic or embryonic visceral endoderm, respectively. Together with the ExE cells, the Epi cells elongate and form a cavity that is called the egg cylinder.

During implantation, the embryo undergoes a massive change in its architecture (Rivera-Pérez & Hadjantonakis, 2014). The TE in contact with the Epi cells, continues to divide forming the ectoplacental cone (EPC) and extraembryonic ectoderm (ExE), which will both contribute to the placenta (peri-implantation embryo, Figure 1). Some cells of the PrE migrate and cover the whole inner surface of the TE, which is called parietal endoderm. The remaining PrE cells become the visceral endoderm and overlay the ExE and Epi cells, which is then distinguished as exVE and emVE, respectively. The exVE and emVE cells build a basement membrane composed of laminin, collagen

and fibronectin (Brown, 2011). At the same time, the Epi and ExE cells form a cavity in their center, the proamniotic cavity, and elongate, so that they become U-shaped when seen in cross-section. Both, Epi and PrE cells form a single layered epithelium on top of each other with apicobasal polarity. All further lineages composing the mature animal will be formed from the epiblast.

1.1.2 Patterning in the post-implantation embryo

The initial step in establishing the head-to-tail axis in the embryonic egg cylinder begins with the emergence of a distinct cell population at the bottom tip within the VE, referred to as the distal visceral endoderm (DVE, Figure 2A) (Rivera-Pérez & Hadjantonakis, 2014; Stower & Srinivas, 2018). These cells undergo a morphological change from cuboidal to columnar shape (Kimura et al., 2000) and express specific marker genes as Sfrp1, Sfrp5, Dkk1, Lefty1 and Cer1, all antagonistic signals for Wnt, Nodal, and Bmp signaling (Figure 2B). The DVE then migrates towards the side of the cup until it reaches the boundary between Epi and ExE cells. The cell population is considered then as the anterior visceral endoderm (AVE) and lays down the axis for anteroposterior polarity in the mouse embryo (Thomas & Beddington, 1996). Whether the DVE is the precursor of the AVE (Srinivas et al., 2004) or whether DVE and AVE are two separated lineages during post-implantation development is still under debate (Takaoka et al., 2011; Zhu et al., 2023). The AVE is not a static or homogenous cell population. Instead, different markers are expressed in different subpopulation and AVE marker-negative VE cells that enter the distal tip, acquire AVE gene expression and are newly recruited to join the AVE (Hoshino et al., 2015). Furthermore, current research findings suggest, that after a specific time AVE cells migrate laterally out and regain a VE character, pointing to a transient nature of AVE cells (Thowfeequ et al., 2021).

The AVE plays an essential role during embryonic development as it marks the start of the process by which the body plan is laid down. Through its secretion of antagonistic signals, the AVE protects the underlying Epi cells from BMP and Wnt signals that are expressed by the ExE cells and VE cells on the opposite side of the embryo (Figure

2B) (Acampora et al., 1995; Stower & Srinivas, 2018; Waldrip et al., 1998). Thereby the underlying Epi cells will form the neuroectoderm, mainly responsible for the head region, while the Epi cells on the opposite side will undergo epithelial to mesenchymal transition in the primitive streak region and will later form the meso- and endoderm. The process in which the three germ layers, ectoderm, mesoderm, and endoderm, are formed and positioned, is called gastrulation (Beddington, 1990). This process primes the system for organogenesis and therefore marks a critical step during embryonic development.

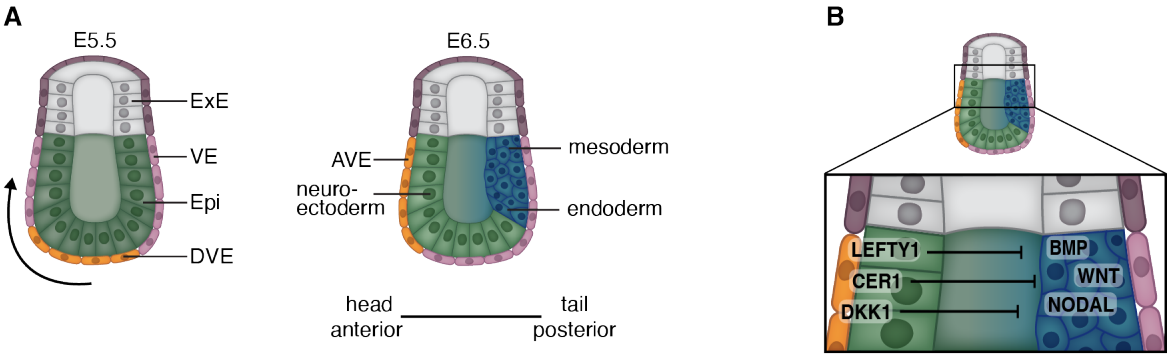

Figure 2: Formation of the anterior visceral endoderm (AVE).
A The formation of the antero-posterior axis in the embryo, which is also known as head to tail axis, is initiated through the formation of a specialized cell population within the VE cells at the distal tip. This population is first described as distal visceral endoderm (DVE), which then migrates towards the side until it reaches the ExE/Epi boundary and specifies the side as anterior. The cell population on the side of the cup is termed anterior visceral endoderm (AVE). Influenced by the AVE, the underlying cells of the epiblast will give rise to the neuroectoderm, while the cells on the other side will form the meso- and endoderm. **B** The AVE secretes a lot of molecules as LEFTY1, CER1 and DKK1, which are antagonistic signals for NODAL, WNT and BMP, so that the underlying tissue gets protected of this posteriorizing signals.

1.2 Signaling in the post-implantation embryo

The signaling networks essential for the proper development of the post-implantation embryo, particularly in the formation of the anterior-posterior axis, include Nodal, BMP and Wnt pathways. Here, I will provide an overview of these signaling networks, followed by an examination of their associated phenotypes and their interplay within the context of AVE differentiation.

1.2.1 Nodal and BMP4 signaling pathways

Activin, Nodal, and BMP4 are all members of the transforming growth factor β super-family ligands, but fulfil different roles in the development of the post-implantation embryo (Papanayotou & Collignon, 2014).

The Nodal signaling pathway can be activated by Activin or Nodal itself (Figure 3). Both ligands are secreted as dimerized precursors requiring processing by Furin or other proprotein convertases for signaling potential (Constam, 2014). Activins, homo- or heterodimers of βA or βB subunits, produce three variants: ActivinA, ActivinB, and ActivinC, collectively referred to as Activin. Unlike Activin, Nodal necessitates an EGF-CFC co-receptor called Crypto or Cryptic to activate the receptor complex (Gritsman et al., 1999). Activin/Nodal bind type I (Alk 4/7) and type II (ActRIIA or B) serine-threonine kinase receptors, where type II receptors phosphorylate and activate type I receptors (Chng et al., 2011). Signal transduction involves receptor-activated Smad2 and Smad3, forming a complex with Smad4, translocated to the nucleus to activate target gene expression, including Nodal, as a positive feedback loop. Activin/Nodal signaling also induces Lefty1 and Lefty2, antagonistic signals to Nodal, but not Activin (Schier, 2003). Lefty1 and Lefty2 directly interact with Nodal ligands and the co-factor Cripto, while Activin can be antagonized by Follistatin (Papanayotou & Collignon, 2014).

Bmp4 modulates Activin/Nodal signaling, interacting with a different type I (Alk 3/6) serine-threonine kinase receptor but sharing ActRII (Figure 3) (Furtado et al., 2008; Yamamoto et al., 2009). Bmp signal transduction involves Smad1/5/8 that form a complex with Smad4, potentially counteracting Activin/Nodal signaling by competition for a limited pool of type II receptor ActRII and Smad4. Additionally, there are other possibilities how Nodal and BMP signaling are antagonizing each other: Gdf1 and Gdf3 promote Nodal but inhibit Bmp signaling by forming heterodimers with Nodal or Bmp (Levine & Brivanlou, 2006). Inhibitory Smads 6 and 7 regulate both pathways, with Smad6 specifically inhibiting Bmp signaling.

For in vitro experiments, recombinant Nodal protein is often substituted with ActivinA due to its low bioactivity and cofactor requirements (Chng et al., 2011). Activin is thought to play no essential role in the early embryo and especially for AVE

differentiation as it is not expressed in the Epi or VE cells (Albano et al., 1993; Papanayotou & Collignon, 2014) and embryos lacking Activin βA or βB subunits show no early phenotype (Matzuk et al., 1995; Vassalli et al., 1994).

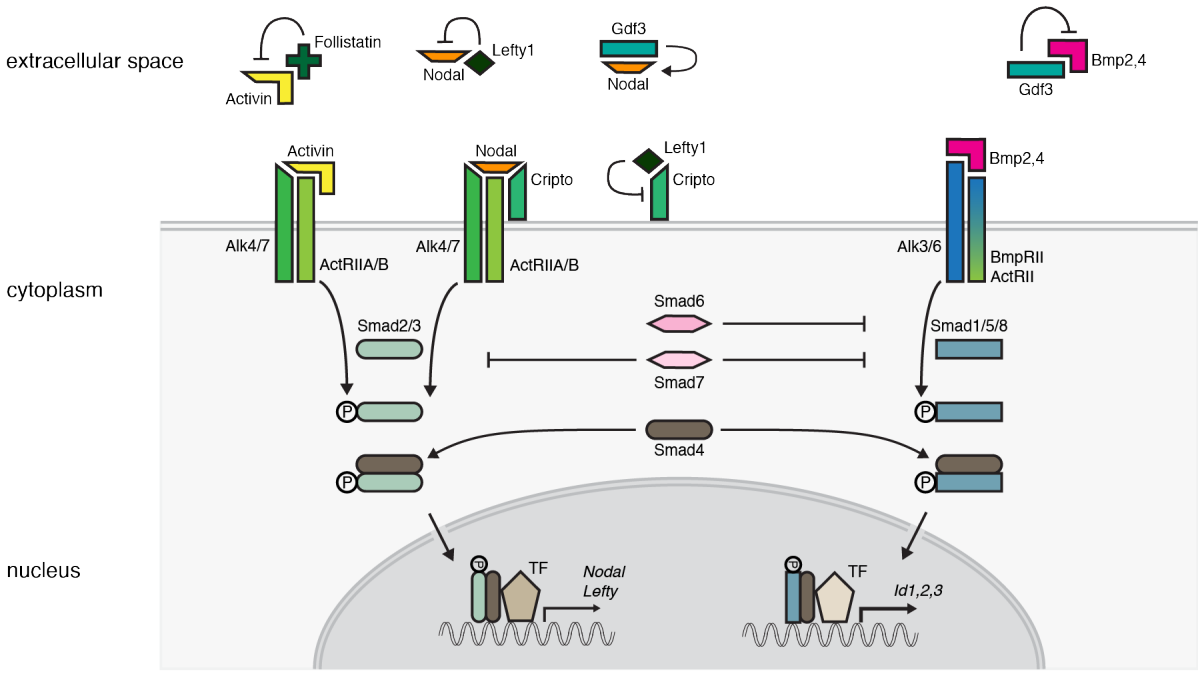

Figure 3: TGF-β (Nodal and BMP4) signaling network.
The Activin/Nodal pathway utilizes the same receptor complex, comprising a type I and a type II serine-threonine kinase receptor. Nodal, however, necessitates an additional cofactor, Cripto. Downstream signaling involves the phosphorylation of Smad2/3, which, in conjunction with Smad4 and tissue-specific transcription factors, activate Nodal target genes. These genes include Nodal itself, facilitating its own expression, and Lefty genes, which antagonize Nodal but not Activin. Bmp can counteract the Nodal signaling pathway due to similar signal transduction mechanisms and a limited pool of shared type II receptors and Smad4 molecules. See text for further details. Figure adapted from (Papanayotou & Collignon, 2014).

1.2.2 Wnt/β-catenin signaling

Intercellular Wnt signaling is named after the proteins encoded by the *wingless* gene in Drosophila and *Int* gene in mammals (Nusse et al., 1991). Comprising 19 distinct Wnt proteins, Wnt activates diverse intracellular signaling pathways, including the β-catenin-depend pathway, also known as the canonical pathway, and the β-catenin-independent pathways, such as the planar cell polarity pathway and the Wnt/Ca^{2+} pathway (Habas & Dawid, 2005). Given the focus of this study on β-catenin, Figure 4 illustrates solely the β-catenin-dependent Wnt signaling pathway. In the absence of Wnt

signaling, β-catenin associates with a destruction complex in the cytoplasm, comprising protein kinases CK1 and GSK3, Axin, and APC (Stamos & Weis, 2013). Phosphorylation by GSK3 and CK1 leads to β-catenin degradation via the ubiquitin/proteasome pathway. Consequently, β-catenin fails to reach the nucleus, where transcriptional co-repressors Groucho/TLE bind to TFC/LEF transcription factors inhibiting gene expression (Daniels & Weis, 2005). Upon Wnt ligand binding to the transmembrane receptor Frizzled, Dishevelled is recruited to the to the plasma membrane, facilitating the clustering of Frizzled and its co-receptor LRP5/6 and promoting phosphorylation of the cytoplasmic tail of LRP5/6 (Liu et al., 2022). Additionally, Dishevelled recruits Axin and GSK3 to the plasma membrane, disrupting the proper formation of the destruction complex. As a result, β-catenin avoids degradation, accumulates in the cytoplasm, and translocated into the nucleus, where it displaces the co-repressors and binds to TCF/LEF, leading to the expression of Wnt/β-catenin target genes.

However, β-catenin plays a dual role in the cell (Figure 4). Besides its role as a key effector of Wnt/β-catenin signaling, it is also integral to adherens junctions, where it links cell adhesion molecules to the cytoskeleton (van der Wal & van Amerongen, 2020). Adherens junctions, one of three classes of potential cell-cell adhesion, involve cell adhesion receptors binding to receptors on neighboring cells, including classical cadherins as E-cadherins and nectins. Cadherins bind to one another through the extracellular domain, leading to the clustering of cadherins at the contact site. The cytoplasmic tails of cadherins form a complex with β-catenin, α-catenin and p120-catenin, connecting cadherins to the actomyosin cytoskeleton composed of structurally dynamic actin filaments subject to tension generated by myosin II motors (Mège & Ishiyama, 2017). This cadherin-catenin complex is under constitutive actomyosin-generated tension, which is required to stabilize the linkage between the complex and the actin filaments and increase dissociation lifetime, described as a catch-bond mechanism (Buckley et al., 2014).

Overall, there are two functional pools of β-catenin: one is transcriptionally active, and the other is adhesive. However, the balance between these pools and their interaction remains a topic of debate (van der Wal & van Amerongen, 2020).

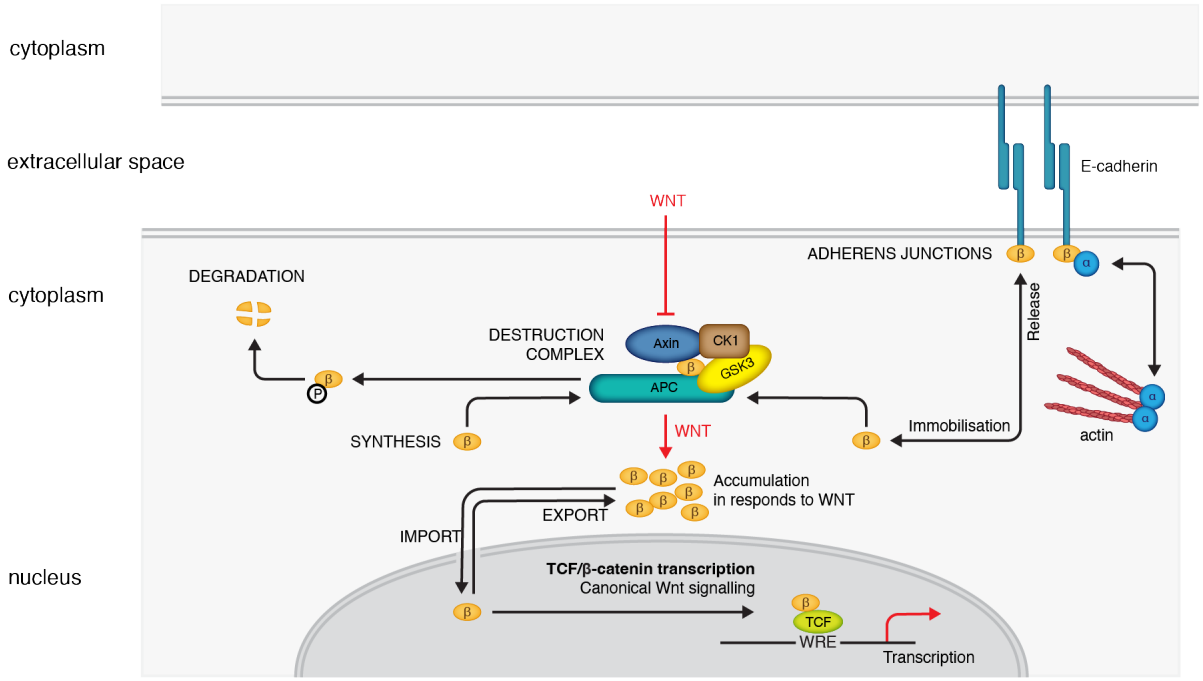

Figure 4: The role of β-catenin in Wnt signaling and cell adhesion.
There are two pools of β-catenin in cells: an adhesive pool and a transcriptional active pool. β-catenin plays a role in adherens junctions where it links the intracellular domain of E-cadherins to the actomyosin cytoskeleton. Additionlly, upon active Wnt signaling β-catenin is set free from the destruction complex and can translocate into the nucleus where it activates together with TCF/LEF Wnt target genes. Figure recreated after (Valenta et al., 2012).

1.2.3 Nodal and BMP antagonism mediates AVE differentiation

The process of AVE differentiation requires precise spatiotemporal interaction between the signaling networks described above within the distinct tissues of the post-implantation embryo. Although correctly referred to as DVE, in the context of AVE differentiation in this study, the term denotes the initial specification of AVE cells at the distal tip.

Early knockout experiments have demonstrated that embryos deficient for *Nodal* or his intracellular signaling transducer *Smad2* lack anterior identity, pointing to Nodal as the pivotal induction signal for AVE differentiation (Figure 5) (Brennan et al., 2001). Furthermore, Nodal expression in the epiblast is crucial for maintaining pluripotency and inducing Nodal expression in the VE (Mesnard et al., 2006). Later, Nodal becomes restricted to the posterior epiblast, controlling primitive streak formation and the induction of posterior genes. Therefore, *Nodal* mutant embryos exhibit anteroposterior axis

abnormalities and failed gastrulation (Brennan et al., 2001; Conlon et al., 1994; Iannaccone et al., 1992; Robertson, 2014).

Although Nodal is expressed throughout the epiblast at that stage, AVE specification is confined to the distal tip, indicating the presence of another signal that is spatially restricting AVE differentiation. These signals are thought to originate from the ExE, as surgical removal of the ExE from the mouse embryo, leads to an ectopic AVE marker expression throughout the VE (Rodriguez, 2005). Experimental evidence suggests BMP4 as this restricting signal, as it is expressed in ExE cells and its downstream signaling mediator Smad1 is absent in the distal VE region shortly before DVE formation (Figure 5) (Yamamoto et al., 2009). Furthermore, experiments involving chimeric explants containing an embryonic portion (Epi and VE) with a reporter for the DVE/AVE marker Hex and an extraembryonic potion (ExE and VE) support this hypothesis. Treatment of the extraembryonic explant with the BMP antagonist Noggin resulted in an expansion of the DVE region in the embryonic portion after combining. However, when this Noggin-treated extraembryonic portion was attached to the side of an embryo with an intact ExE region, DVE formation appeared normal, indicating that the DVE restricting signal from the ExE was abolished with Noggin treatment. BMP4, initially expressed in the ExE post-implantation, is involved in anteroposterior axis and primitive streak formation (Fujiwara et al., 2002; Roberts et al., 2022). *Bmp4* mutant embryos exhibit various defects in gastrulation and mesoderm formation (Winnier et al., 1995).

As a mechanism underlying AVE formation, an antagonism between Nodal-controlled Smad2 and Bmp-controlled Smad1 was proposed (Yamamoto et al., 2009). DVE formation requires the absence of Smad1 but presence of Smad2. This balance is thought to be regulated by the shared type II receptor ActRII and the shared signaling mediator Smad4 (Figure 3). Experimental validation of this hypothesis involved treating embryos with the Nodal inhibitor SB43, which led to a downregulation of phosphorylated Smad2 levels and slight upregulation of phosphorylated Smad1 levels at the distal tip. Conversely, treating embryo explants lacking an ExE with SB43 resulted in the loss of both phosphorylated Smad1 and Smad2, indicating the necessity of Smad2 signal and at the same time absence of Smad1 signaling for DVE formation.

The Wnt signaling pathway is not directly associated with AVE differentiation, as blocking Wnt ligand secretion resulted in no AVE related phenotype (Biechele et al., 2013). However, what is particularly intriguing is that APC mutant embryos, characterized by a hyperactive β-catenin, show a loss of AVE differentiation (Chazaud & Rossant, 2006).

Together, the formation of a spatially restricted AVE at the distal tip of the embryo requires Nodal as the induction signal expressed throughout the epiblast, along with BMP serving as the restriction signal expressed as gradient from the ExE. This regulatory network not only ensures the proper establishment of the AVE and subsequent formation of the anterior-posterior axis, but is also hypothesized to function as a growth control point (Mesnard et al., 2006; Orietti et al., 2021). In this context, the AVE can only be properly formed when the egg cylinder has elongated to a specific extend, positioning the VE cells at the distal tip out of reach of the inhibitory BMP gradient.

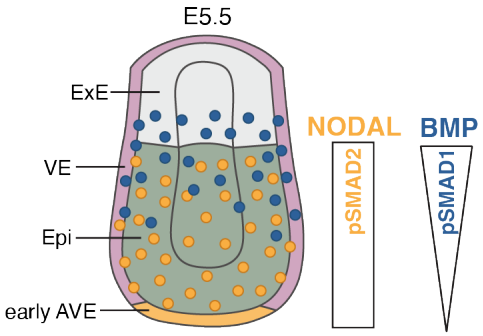

Figure 5: Model for AVE induction.
The model for spatially restricted AVE formation at the distal tip of the embryo (DVE) is based on the antagonism of the two signaling molecules, NODAL (orange) and BMP (blue). NODAL serves as the induction signal and is expressed form the entire epiblast able to induce an AVE in all of the overlain VE. BMP serves as the inhibitory signal and is expressed as a gradient from the ExE. Consequently, the proposed antagonism between the signaling transducer Smad2 (NODAL) and Smad1 (BMP) restricts AVE differentiation to the distal tip of the embryo (Yamamoto et al., 2009).

1.3 Patterning mechanisms in the embryo

Differentiation of the AVE within the VE tissue represents a crucial patterning process during embryonic development. Two generic models govern the establishment of such patterning: a gradient-based model or self-organization model. Patterning involves a series of coordinated events that occur in response to chemical and mechanical

signals. While mechanical cues rely on direct cell-cell contact, chemical signals, often mediated by diffusible proteins known as morphogens, can influence cells over longer distances. Morphogens act in a concentration-dependent manner, shaping spatial gradients and signaling centers that specify regional identities of cells along the embryonic axes (Briscoe and Small, 2015). The model for AVE differentiation described earlier involves BMP4 from the ExE serving as an external gradient, orchestrating VE patterning by confining AVE differentiation beyond this gradient.

In contrast, the formation of the anterior-posterior axis in mammals, which is equivalent to AVE differentiation, deviates from many other species where axis formation relies on pre-existing maternal egg patterning (Kimelman & Martin, 2012). A classic example is the establishment of the anterior-posterior axis in Drosophila.

1.3.1 Positional information in a gradient

In the Drosophila embryo, the anterior-posterior axis is formed by the first ever found morphogen, the anterior determinant Bicoid (Driever & Nüsslein-Volhard, 1988). Maternally inherited *bicoid* mRNA is anchored at the anterior tip of the oocyte and early embryo (Figure 6A) (Johnston et al., 1989). Translation of the *bicoid* mRNA begins upon egg laying resulting in a concentration gradient of the Bicoid protein via diffusion, with its highest concentration at the anterior tip gradually diminishing towards the posterior (Figure 6A) (Porcher & Dostatni, 2010). Bicoid functions as a morphogen gradient, crucial for establishing polarity along the embryonic anterior-posterior axis.

The concept how cells acquire different identities along a morphogen gradient is described by Lewis Wolpert as “positional information” (Figure 6B) (Wolpert, 1969). In this model, cells gain positional vales as in a coordinate system, which are then interpreted by thresholds to dictate diverse outcomes (Tkačik & Gregor, 2021). Wolpert’s famous French Flag model illustrates the interpretation of positional cues in a morphogen gradient by two thresholds (T1 and T2 in Figure 6B) that delineate three different discrete cell identities (depicted as blue, white and red reminiscent of the colors of the French flag).

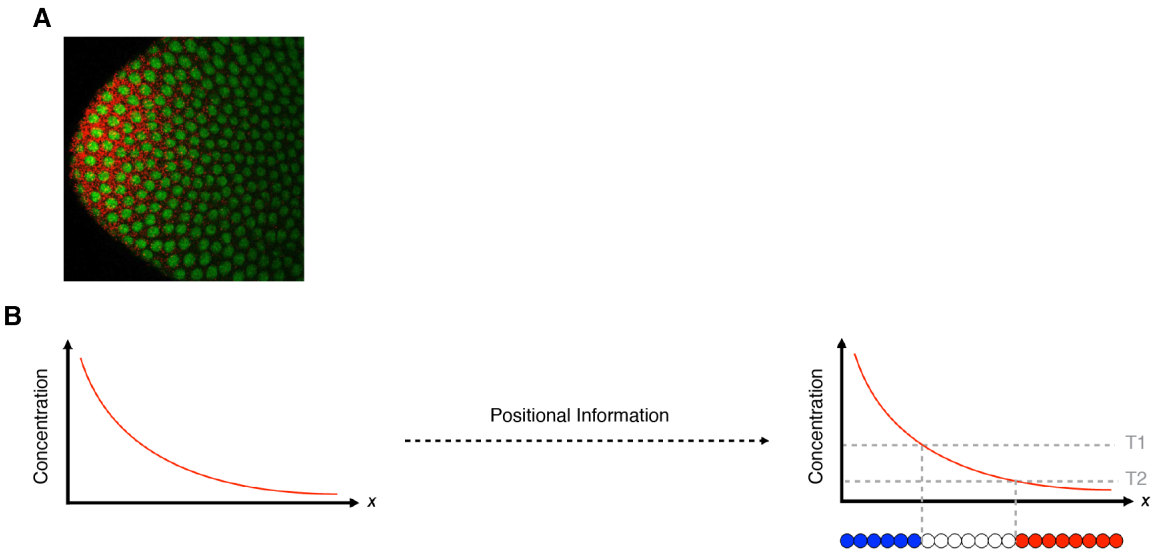

Figure 6: Positional information model.
A A gradient of Bicoid protein (green) is established from maternally deposited mRNA (red) at the anterior pole. **B** Within a single morphogen gradient along the linear x dimension (left), cells interpret their position based on thresholds (T1 and T2, right) in the morphogen gradient leading to the adaption of different cell identities (blue, white and red). Figure modified from (Tkačik & Gregor, 2021).

The model for AVE differentiation in mouse embryos is based on Wolpert's positional information concept, where VE cells acquire positional cues along the BMP4 gradient. However, in contrast to Drosophila, the BMP4 gradient in mammals is not preformed but established from an extraembryonic tissue, the ExE. Other mammalian embryos, such as primates and humans, may not exhibit this external BMP4 gradient due to their different structure, posing questions about their patterning mechanisms (Figure 7).

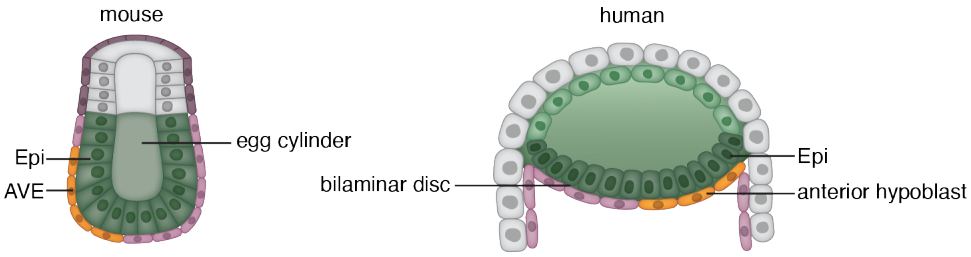

Figure 7: Mouse and human embryos in comparison.
Schematic representation of a part of the mouse and human embryo around the time of AVE and anterior hypoblast specification. While the mouse embryo is shaped like a cup, the human embryo forms a disc-like structure.

1.3.2 Self-organization

In contrast to Wolpert's positional information model, which relies on external cues such as external morphogen gradients or signaling centers to establish patterning, Turing proposed a model where cells autonomously create patterning through cell-cell communication without external clues (Turing, 1952). He introduced a reaction-diffusion model where diffusion could cause instability (Turing instability) of a spatially uniform state, leading to the formation of spatial patterns. Later, but unaware of Turing's described model, Meinhardt and Gierer formulated a theory explaining the emergence of polarity and pattern from near-uniform states by local self-enhancement and lateral inhibition (Gierer & Meinhardt, 1972). They proposed that patterning could be mediated by a combination of a short-range activator with strong self-enhancement capabilities coupled with a long-range inhibitor that restricts the expansion of the activator in the surrounding areas. While Turing's system can be conceptualized as a combination of short-range activators coupled with long-range inhibitors, Turing did not explicitly describe the fundamental concept of local self-enhancement and long-range inhibition in his paper, although it is inherent in his equations (Müller & Nüsslein-Volhard, 2016).

In an activator-inhibitor model, the patterning formation unfolds as follows (Figure 8) (Green & Sharpe, 2015): initially, the system exhibits an almost homogenous spatial pattern. However, even slight random fluctuation in gene expression can lead to the emergence of areas with higher activator concentrations. This increase is then further amplified by the positive feedback loop of the activator. Concurrently, the levels of the inhibitor also rise at the same position, but due to their differing diffusion rates, the secreted activator and inhibitor do not act within the same area. With a higher diffusivity than the activator, the inhibitor diffuses away from the activation area, inhibiting activation of neighboring regions. However, the activation area with lower inhibitor levels stabilizes. Depending on the inhibitor's diffusivity, new activation areas may form, beyond the reach of the inhibitor's repression from existing ones. This process results in a spatially periodic distribution of concentrations, characterized by alternating regions of activation and inhibition.

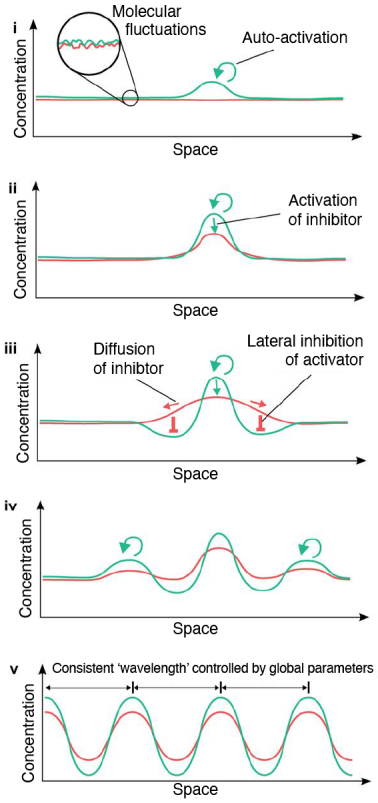

Figure 8: The principles of reaction-diffusion.
The activator-inhibitor model contains two diffusible molecules: the activator and its own inhibitor. Both promote their own expression, while the activator also promotes the expression of the inhibitor. Starting from a homogenous distribution of these molecules, molecular fluctuations will lead to cells with a slightly higher activator level, which will then auto-enhance its levels (i). But since the activator is also controlling the expression of its inhibitor, the inhibitor level will also rise (ii). The differential diffusivity of the two molecules, with the activator having a rather slow diffusion rate compared to fast diffusion rate of the inhibitor, will give rise to a spatial pattern of concentrations. The inhibitor will diffuse away and inhibit neighboring regions to enhance the activator, thus creating a repressing zone around the first peak, while the peak region itself can stabilize (iii). However, new peaks can form outside of the inhibitor influence regions (iv), which results in a regular array of peaks and valleys (v). Figure modified from (Green & Sharpe, 2015).

Nodal and Lefty were identified to act as an activator-inhibitor pair (Chen & Shen, 2004; Muller et al., 2012; Nakamura et al., 2006; Sekine et al., 2018). Nodal functions as the activator, promoting its own expression and also that of its own inhibitor, Lefty. Notably, Nodal exhibits a lower diffusion rate compared to Lefty (Muller et al., 2012). Together they orchestrate an activator-inhibitor mechanism in a reaction-diffusion system to establish left-right asymmetry in the lateral plate mesoderm (LPM) (Nakamura et al., 2006). Initially, low Nodal expression in the left LPM initiates its own activation and induces Lefty2 expression. Subsequently, it spreads to the midline, triggering Lefty1

expression there. Both Lefty2 and Lefty1 proteins diffuse faster than Nodal, leading to the inhibition of Nodal expression in the right LPM and establishing tissue asymmetry.

1.4 Model systems to study post-implantation development

In recent years, there has been a significant increase in the development of various stem cell-based embryo models, offering the potential to enhance our understanding of embryonic development, including processes such as patterning, differentiation, and morphogenesis.

1.4.1 Derivation of stem cells

Stem cells possess distinct characteristics that set them apart from somatic cells: they have the ability to proliferate, self-renew through division, and generate differentiated progenies (Blau et al., 2001). The differentiation potential of a stem cell determines its type, with higher potential indicating the capacity to generate more diverse cell types from various lineages.

At the earliest stages of mouse development, blastomeres from the fertilized zygote to the eight-cell stage exhibit the highest plasticity, known as totipotency. Totipotent cells can differentiate into all three germ layers of the embryo and extraembryonic tissues (Mitalipov & Wolf, 2009). In contrast, mouse embryonic stem cells (mESCs), also known as pluripotent stem cells (PSCs), from the ICM of an E3.5 embryo have reduced developmental potential and are pluripotent (Figure 9). They can give rise to cell types from all three germ layers but have a reduced capacity for extraembryonic differentiation. These cells were first successfully cultured in 1981 by the biologists Sir Martin John Evans and Mathew Kaufman using fibroblasts and Dulbecco's modified minimal essential medium supplemented with 10% fetal calf serum and 10% newborn calf serum (Evans & Kaufman, 1981). The key to their success was the co-culture with mouse embryo fibroblasts. These produce the cytokine leukemia inhibitory factor (LIF) which activates the transcription factor Stat3, thereby inhibiting ESC differentiation and promoting viability (Smith & Fox, 2001).

Since the original culturing protocol for mESCs, significant advancements have been made to identify signals that maintain the cell in their naïve pluripotent state and prevent them from priming for differentiation. The approach has shifted from using serum and fibroblasts to a fully chemically defined medium and extracellular matrix proteins such as fibronectin to which the cells can adhere (Ying et al., 2008). Studies have shown while stimulation of the Erk signaling pathway by FGF4 and other extrinsic stimuli primes ESCs for differentiation, inhibition of this pathway, along with an ancillary suppression of the glycogen synthase kinase 3 (GSK3) to activate transcriptionally activity of β-catenin using selective small molecule inhibitors, stabilizes and sustains mESCs in their pluripotent state (Anton et al., 2007; Burdon et al., 1999; Kunath et al., 2007). This combination of the two inhibitors (2i) and LIF, referred to as 2i+LIF, in a chemically defined medium known as N2B27, is sufficient to stabilize and sustain mESCs with full pluripotency (Ying et al., 2008).

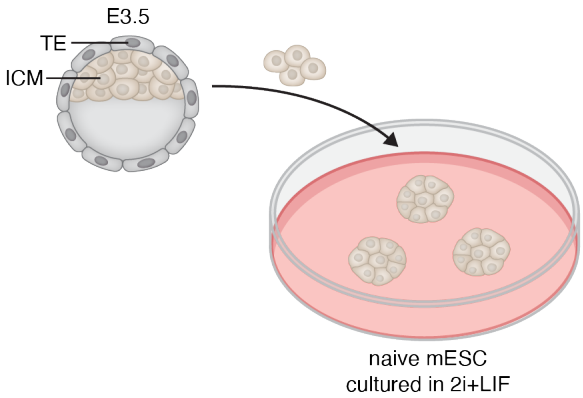

Figure 9: Derivation of mouse embryonic stem cells.
ICM cells from the mouse E3.5 embryo can be derived as naïve mouse embryonic stem cells (mESCs) in their pluripotent state. These cells are usually seeded on dishes coated with extracellular matrix proteins as fibronectin and maintained in the chemically defined medium N2B27 supplemented with MEK inhibitor, Wnt activator and LIF, referred to as 2i+LIF.

mESCs are distinguished by the expression of key transcription factors, including OCT3/4, SOX2, KLF4, and NANOG, which play essential roles in maintaining their pluripotency (Takahashi & Yamanaka, 2006). These cells typically grow in dome-shaped colonies, reflecting their undifferentiated state and robust proliferative capacity. As embryonic development progresses, stem cells progressively lose their developmental potential. Adult stem cells, considered as multipotent, are the only

remaining stem cell type in the adult body, capable of both self-renewal and differentiation into cell types from one or two lineages (Bhatt et al., 2013).

In addition, it is possible to derive cells of the PrE and TE from an E4.5 embryo as extraembryonic endoderm (XEN) and trophoblast stem cells (TSCs) and maintain them in a serum containing stem cell medium (Niakan et al., 2013). Alternatively, PrE, as well as TS cell lines, can be established by overexpression of specific transcription factors. To induce the differentiation of mESCs into PrE cells in vitro, the transcription factor GATA, the principal regulator of PrE fate, is overexpressed (Fujikura et al., 2002).

1.4.2 Post-implantation embryo models

Stem cells are a powerful tool to study the embryonic development serving both in 2D cultures and as the foundation for constructing 3D stem cell-based embryo models. In recent years, significant progress has been made in reliably modeling specific developmental processes, such as gastrulation, and various embryonic states from the blastocyst to the post-implantation embryo (Fu et al., 2021). These models can be broadly categorized into integrated stem cell-based embryo models, which mimic the entire embryo with all its lineages, and non-integrated stem cell-based embryo models, which focus on specific developmental processes using only ESCs without extraembryonic stem cells (Rossant & Tam, 2021).

One of the most well-known models utilizing only mESCs are gastruloids, where mESCs are aggregated in microwells and treated with a Wnt pulse to initiate axial organization resembling gastrulation (Beccari et al., 2018). While gastruloids can recapitulate some features of antero-posterior axis patterning in a self-organizing manner, they typically lack anterior structures such as brain cell types due to the absence of extraembryonic tissues (Beccari et al., 2018; Moris et al., 2020). However, recent advancements have led to more sophisticated versions of gastruloids capable of modeling events like somitogenesis. By substituting the Wnt pulse with treatment involving FGF2, ActivinA and Wnt inhibition, anteriorized gastruloids expressing primitive streak markers and neural precursors markers on opposite poles have been achieved

(Sullivan & Santos, 2023). Additionally, neural epithelial structures have been obtained by combining mESCs with XEN, indicating the enhanced developmental potential of embryonic stem cells with the addition of extraembryonic tissues (Bérenger-Currias et al., 2020).

Integrated stem cell-based embryo models, such as ETX embryoids, exhibit even greater similarity to embryos when mESCs are combined with stem cells from both extraembryonic lineages, trophoblast stem cells and XEN cells (Sozen et al., 2018; Zhang et al., 2019). When aggregated in microwells, these stem cells self-organize into structures resembling the morphology of a post-implantation embryo, albeit lacking the outermost extraembryonic tissues like trophectoderm and parietal endoderm. Within ETX embryoids, mESCs and TSCs form epiblast and ExE, respectively, as two joined cell masses on opposite poles with a connecting lumen. The surrounding XEN cells encompass the Epi and ExE compartments as VE cells, mirroring the egg cylinder structure of a post-implantation embryo. Improvements to ETX embryoids involved the use of iXEN cells, wherein mESCS with a GATA-inducible gene construct differentiate into VE cells (Amadei et al., 2021; Dupont et al., 2023). These iETX were then capable of differentiating the AVE within the VE compartment, which lays down the anterior-posterior axis, and the iETX embryoids gastrulate to form both embryonic and extraembryonic mesoderm, as well as definitive endoderm. With further advancement, it was demonstrated that iETX embryoids could be cultured for longer periods with adapted media and culture conditions, allowing them to progress into neurulation and heart development (Amadei et al., 2022; Lau et al., 2022; Tarazi et al., 2022).

In the past year, significant strides have been made in transferring the knowledge gained from mouse integrated stem cell-based embryo models to human systems. Researchers have focused on developing human integrated stem cell-based embryo models that closely resemble the post-implantation embryo (Oldak et al., 2023; Weatherbee et al., 2023). These models differ in how the extraembryonic lineages are formed, whether through the induction of specific genes (Weatherbee et al., 2023) or with small molecules in specific media conditions (Oldak et al., 2023). Human embryos, compared to mouse embryos, have a different structure. While mouse embryos typically form a cup- or cylinder-like structure, human embryos take on a disc-shaped

appearance (Figure 7) (Rossant & Tam, 2022). Regarding the differentiation of the AVE, studies have shown that both human embryos and their models develop a cell population reminiscent of the AVE in mouse embryos (Molè et al., 2021; Oldak et al., 2023; Weatherbee et al., 2023). However, due to their disc-like shape, human embryos likely lack the same inhibitory gradient that is supposed to restrict AVE differentiation to a specific location in mouse embryos. Consequently, a significant question in the field pertains to how the human embryo regulates AVE differentiation.

Exploiting the modularity of stem cell models allows researchers to recreate specific parts of the post-implantation embryo, such as the Epi and VE compartments (Amadei et al., 2021; Vrij et al., 2022). When induced XEN and mESCs are aggregated together, they form spheres with an inner epi layer including a lumen and an outer VE layer, resembling the mouse egg cylinder without the ExE. Recently, similar models derived from human embryonic stem cells and induced hypoblast (analogous to induced VE cells in mouse models) have been developed, presented in both attached and floating forms (Hislop et al., 2024; Okubo et al., 2024). These models, whether from mouse or human stem cells, provide a platform to study the interaction and morphogenetic potential of specific lineages under simplified conditions. However, they often require the induction of specific signaling pathways to compensate for the absence of various lineages.

1.5 Objectives

The formation of the embryo's anterior-posterior axis hinges on the precise positioning of the AVE. While Nodal triggers AVE differentiation in the VE (Brennan et al., 2001), its localization to the distal tip is directed by an inhibitory BMP4 gradient from the ExE (Yamamoto et al., 2009). Given the limitations of gradient-based models, I utilized stem cell-based approaches to uncover potential underlying mechanisms of AVE differentiation.

My primary objective was to establish an embryo-like model system using a mESC line engineered with a GATA4-inducible gene construct. Upon exposure to doxycycline, this line generated a mixture of Epi and PrE cells, precursors of the VE, which then spontaneously transitioned from a 2D layer into floating spheres. Referred to as bilayered embryo-like aggregates (BELAs), these spheres exhibited a bilayered structure reminiscent of the organization of the Epi and VE compartments of the peri-implantation embryo. I found that the Epi and PrE/VE cells communicate via FGF4 and extracellular matrix interactions to maintain survival and undergo morphogenetic events. Notably, single-cell RNA sequencing unveiled a subset of VE cells expressing AVE marker genes, which could be visualized in a spatially restricted location through different staining techniques. (Results 3.1-3.3)

As a second goal, I aimed to establish a 2D AVE differentiation protocol. Leveraging the single-cell RNA sequencing data obtained from BELAs, I identified Nodal signaling as the crucial AVE induction signal, a discovery corroborated through experiments involving Nodal inhibition and genetic mutation. Treatment with FGF4, coupled with the activation of the Nodal signaling pathway using ActivinA, was sufficient to initiate AVE differentiation in a pure layer of VE cells. Interestingly, I observed AVE differentiation occurring in clusters throughout the VE layer, revealing a tissue-intrinsic mechanism of VE cells to spatially regulate AVE differentiation. (Results 3.4)

For my third aim, I sought to identify the signal from VE cells that counteracts AVE differentiation. Initially, I examined the influence of BMP4 signaling, a known antagonist in the AVE differentiation model. While BMP4 impacted the number of cells expressing the AVE marker Cer1, there was no indication of tissue-intrinsic BMP4 counteracting

AVE differentiation. Subsequently, I explored Nodal and Lefty as a potential reaction-diffusion pair to spatially restrict AVE differentiation, yet mutations of Nodal and Lefty failed to produce the expected phenotypes. Finally, I uncovered that β-catenin antagonizes AVE differentiation independently of Wnt signaling, potentially regulated by mechanical cues in adherens junctions. (Results 3.4-3.7)

2 Methods

2.1 Cell lines and cultivation

All mouse embryonic cell lines (mESCs) utilized in this thesis originated from an E14tg2a background (Hooper et al., 1987). From the Tet::GATA4-mCherry (iGATA) inducible lines, previously characterized by (Raina et al., 2021), I used two different clones, C5 and C6, that differ in their induction rates. All iGATA4 cell lines, including their subclones, were maintained on fibronectin-coated dishes, except for *Itgb1* mutants, which were cultured on feeders or vitronectin. The culture medium consisted of N2B27 supplemented with 1 μM PD0325901 (SeleckChem), 10 ng/ml LIF (protein expression facility, MPI Dortmund), and 3 μM CHIR99021 (Tocris), commonly referred to as 2i+LIF (Ying et al., 2008). The N2B27 medium composition contained a 1:1 mixture of DMEM/F12 and Neuropan Basal Medium (both from PAN Biotech), supplemented with 1X N2 and 1X B27 supplements, 1X L-Glutamax, 0.0025% BSA, and 0.2 mM ß-mercaptoethanol (all from ThermoFisher). To prevent silencing of the inducible transgene, all iGATA4 cell lines and subclones were constantly maintained under selection with 200 μg/ml G418 (Sigma) at 37°C with 5% CO_2.

2.2 Embryos

Embryos shown in this thesis were kindly supplied and stained by the group of Dr. Ivan Bedzhov, Max-Plack-Institute for Molecular Biomedicine, Münster. For detailed methods see (Schumacher et al., 2023).

2.3 Mutant and transgenic cell lines

2.3.1 Mutant cell lines

All mutations were induced by using the CRISPR/Cas9 technology. Single guide RNAs (sgRNAs) were designed with CRISPick (Doench et al., 2016; Sanson et al., 2018),

Target gene	Cell line	sgRNA	Vector Addgene Selection	Primer
Itgb1 Exon2	iGATA4 cl. C6	5′-GTTATAGATGAATTTGCAAC-3′	PX459 #62988 Puromycin	5′-TGCCTATTAGGTTGAGAGCC-3′ 5′-CCTGACTATTTCTGCCTTCC-3′ 5′-CTGTGTAGATCAGACTGGCC-3′ 5′-CCAACTCATAACCAATTGAGC-3′
Nodal Exon2	iGATA4 cl. C6 Cer1:H2B-Ven	5′-CCCCATGGACATACCCACTG-3′ 5′-CCAGTCGAGCAGAAAAGTGT-3′	PX459 #62988 Puromycin	5′-GTGGACGTGACCGGACAGAACTG-3′ 5′-GGCATGGTTGGTAGGATGAAACTCC-3′
Lefty1 Exon1	Cer1:H2B-Ven	5′-AGGTTCAGCCAGAACCTTCG-3′ 5′-AAAGGGTCTTGAGTCTGCGG-3′	PX458 #48138 GFP	5′-TTACCACCCCTGTCCTGAATG-3′ 5′-ATGACTGACTCTGAGCACCAC-3′
Wnt4 Exon2	Cer1:H2B-Ven	5′-GTGATGGACTCAGTGCGCCG-3′ 5′-TTTGGGAAGGTGGTGACACA-3′	PX459 V2.0 #118055 Blasticidin	5′-CACAAGACCAGGGATGAGGCAG-3′ 5′-GCCACACAAGGTGTTCTGCAG-3′
Wnt 11 Exon5	Cer1:H2B-Ven	5′-GGCCGACAGGGCATACACGA-3′ 5′-CGGAAAACTTGGCCCCCATG-3′	PX459 V2.0 #118055 Blasticidin	5′-GTGCTATAATGCACTGATGAAGGAGGG-3′ 5′-CCAAGCTCTAGAGAGGGAGAAGC-3′
Porcn Exon9/10	Cer1:H2B-Ven	5′-GAAGGAGACAGCACTCTCGT-3′ 5′-ACAACTTCCACCATGGACCG-3′	PX459 V2.0 #118055 Blasticidin	5′-GGCCAACTTCCAGGCCCTC-3′ 5′-GGTACACACCCAGTTTGTACGTGG-3′

cloned into Cas9-expressing vectors using Bbs1 (NEB) according to (Ran et al., 2013), and transfected using Lipofectamine 2000 (Thermo Fisher Scientific) following manufacturer's instructions. After transfection, cells underwent selection with either 15 μg/ml blasticidin for 3 days, 1.5 μg/ml puromycin for 2 days or were selected via flow cytometry for GFP expression depending on the used vector. Afterwards, cells were seeded at clonal density and expanded as clonal lines. PCR amplification of a sequence surrounding the mutation site was performed. Clones yielding a truncated amplicon compared to the wild type were selected and subjected for Sanger sequencing to determine the exact mutation. For further details see table above and results section.

2.3.2 H2B-Cerulean label

To establish a constitutively labeled iGATA4 cell line, a CAG-driven H2B-Cerulean construct was incorporated with a blasticidin resistance cassette into a vector designed for PiggyBac transgenesis (Wang et al., 2008). Clonal transgenic lines were derived following co-transfection of the CAG-H2B-Cerulean-bsd vector with CAGG-pBASE. A suitable clone demonstrating uniform and moderate H2B-Cerulean fluorescence was chosen through epifluorescence microscopy.

2.3.3 Cer1:H2B-Venus reporter

To establish a Cer1 reporter in the iGATA cell line, I amplified the Cer1 promoter region situated 4kb upstream of the start codon from genomic DNA as described by (Morgani et al., 2018). Simultaneously, a puromycin resistance cassette and an H2B-Venus sequence were amplified from Sprouty4 targeting vectors (Raina et al., 2021). These three fragments underwent cloning via Gibson assembly using a HiFi DNA assembly kit (NEB) into a vector backbone containing PiggyBac transposition sites (Wang et al., 2008). The resulting Cer1:H2B-Venus reporter construct was co-transfected with CAG-pBASE, and cells were subjected to selection with 1.5 μg/ml puromycin, starting 24 hours post-transfection. Following transfection, cells were reseeded at clonal density and expanded as clonal lines. Positive clones were identified based on the co-

localization of Cer1 reporter activity and Cer1 mRNA, after cells were differentiated into AVE (Figure 23).

2.4 Formation of Epi cysts

Epi cysts were generated following the protocol outlined by (Bedzhov & Zernicka-Goetz, 2014). Briefly, mESCs were dissociated into single cells and resuspended in growth factor-reduced Matrigel (Corning), which was then dispensed in 25 μl drops onto μ-slides (Ibidi). The Matrigel drops were allowed to solidify by incubating the slides at 37°C for 5 minutes. Subsequently, the slides were filled with either N2B27 or 2i+LIF medium.

2.5 Formation of BELAs

BELAs spontaneously formed after inducing iGATA (clone C6) cells or subclones with 0.5 μg/ml doxycycline (Sigma-Aldrich) pulse in 2i+LIF for 8 hours. Following induction, the medium was changed to N2B27, and the cells were reseeded at a density of 30,000 cells/cm^2 onto dishes that were coated with 0.1% gelatin in PBS. Floating BELAs typically appeared after two days and were collected after three days unless otherwise indicated.

To block the Nodal pathway during BELA formation, iGATA4 cells were treated with 10 μM of the Nodal receptor inhibitor SB431542 (referred to as SB43; Biogems) starting from the initiation of the doxycycline pulse until the aggregates were examined for analysis.

Alternatively, it is also possible to differentiate Epi and PrE cells separately and subsequently mix them at the time of reseeding in a 30-70 ratio, respectively. To achieve this, iGATA4 mESCs or subclones were induced for 8 hours with 0.5 μg/ml doxycycline (in 2i+LIF, followed by 16 hours of treatment with 10 ng/ml FGF4 (PeproTech), 1 μg/ml heparin (Sigma Aldrich) and 0.5 μg/ml doxycycline in N2B27 to initiate the differentiation into PrE cells. Upon switching the medium to N2B27 for the PrE cells, the medium

of an uninduced culture of mESCs was also changed to N2B27. At the end of doxycycline treatment for the PrE cells, both PrE and Epi cells were counted and subsequently reseeded at a density of 30,000 cells/cm^2 in a 30-70 ratio on gelatin-coated dishes.

2.6 Formation of VE cysts

For VE cyst formation, a homogenous culture of PrE cells, the precursors of VE cells, is crucial. When using the iGATA4 C6 clone, cells were induced with a 0.5 μg/ml doxycycline (Sigma-Aldrich) pulse in 2i+LIF for 8 hours, followed by another pulse in N2B27 supplemented with 10 ng/ml FGF4 (PeproTech) and 1 μg/ml heparin (Sigma Aldrich) for 16 hours. In the case of the iGATA4 C5 clone, which exhibits a higher induction rate compared to C6, cells were induced with a 4-hour doxycycline pulse in 2i+LIF, followed by culture in N2B27 supplemented with FGF4 and heparin. Clone C5 was used for the data shown Figure 12C and Figure 14, in all other instances, clone C6 was used. Differentiated PrE cells were then seeded onto dishes coated with 0.1% gelatin at a density of 30,000 cells/cm^2 in N2B27 medium supplemented with 10 ng/ml FGF4 and 1 μg/ml heparin. Floating VE cysts typically appeared within three days.

2.7 AVE differentiation

For AVE differentiation, iGATA4 C6 cells and subclones were induced into PrE cells following the protocol described above. Upon reseeding, cells were plated at a density of 25,000 to 30,000 cells/cm^2 on fibronectin-coated dishes to maintain a 2D culture. The medium used for AVE differentiation consisted of N2B27 supplemented with 10 ng/ml FGF4 (PeproTech), 1 μg/ml heparin (Sigma Aldrich) and an additional 50 ng/ml ActivinA (Cell guidance systems). Unless otherwise indicated, cells were analyzed after three days after reseeding.

Concentrations and durations of additional treatments during AVE differentiation are as follows: 50 ng/ml BMP4 (PeproTech), 100 nM LDN (Sigma Aldrich), 3 μM Chiron (Sigma Aldrich), 2 μM IWP2 (Biogems), 20 μM XAV (Cell Guidance Systems), Blebbistatin (Tocris) were supplemented into the medium from the second doxycycline pules

onwards. 10 μg/ml DECMA E-cadherin blocking antibody (Invitrogen) was supplemented into the medium at the time point of reseeding the PrE cells.

2.8 Immunocytochemistry

BELAs and VE cysts were collected and centrifuged at 100 g for 1.5 minutes, then resuspended in 4% paraformaldehyde (PFA; Carl Roth) at room temperature for 1 hour. Subsequently, the samples were washed 5 times with phosphate buffered saline (PBS, PAN Biotech) for 5 mins each, followed by incubation in PBS containing 1% bovine serum albumin (BSA, Merck) and 0.1% Triton X-100 (PBT+BSA, Serva) at room temperature for 3 hours. Primary antibodies, appropriately diluted in PBT+BSA (see section below), were then added and incubated overnight at 4°C. The following day, samples were washed 5 times in PBT+BSA, before being incubated with secondary antibodies and a nuclear stain, also diluted in PBT+BSA, at 4°C overnight. After removal of the antibody solution, samples were washed 5 times in PBS containing Triton X-100 (PBT) and then resuspended in PBS on μ-slides (ibidi) for analysis.

Epi cysts, embedded in Matrigel drops in μ-slides, underwent extended wash times of 15 minutes. Cells grown as 2D cultures in μ-slides were fixed for only 15 minutes, with washing reduced to three steps of 15 minutes each. To protect the samples, they were covered in mounting medium consisting of 80% glycerol (Gerbu), 16% PBS and 4 % n-propyl-gallate (Sigma Aldrich).

Primary antibodies used were: anti-CER1 (R&D, MAB1986, 1:200) anti-E-cadherin (CDH1, Takara M108, 1:200), anti-GATA6 (R&D, RF1700, 1:200), anti-CD29 (ITGB1, BD Pharmingen 562153, 1:100), anti-LAM (Sigma L9393, 1:750), anti-Oct3/4 (POU5F1, Santa Cruz Biotechnology sc-5279 1:100), anti-OTX2 (Neuromics GT15095, 1:200), anti-pERM (Cell Signaling Technology #3141, 1:200), anti-PODXL (R&D MAB1556, 1:200), anti-SOX17 (R&D AF1924, 1:200), anti-ZO-1 (Invitrogen 61-7300, 1:100), and anti-GFP (Abcam ab13970, 1:200). Secondary antibodies used were all Alexa Fluor-conjugated and purchased from Invitrogen/Life Technologies (1:500). Hoechst was diluted 1:1000.

2.9 In situ HCR

All materials necessary for third generation in situ HCR were procured from Molecular Instruments, and mRNA staining was performed following the manufacturer's instructions (Choi et al., 2018). Samples were fixed for a duration ranging from 15 minutes to 1 hour, depending on sample type, using 4% paraformaldehyde. Post-fixation, the samples were washed four times with phosphate-buffered saline with 0.1% Tween 20 (PBST) and permeabilized overnight in 70% ethanol at -20°C. Following this step, the samples were washed twice with PBST and then incubated in probe hybridization buffer for 30 minutes at 37°C to achieve equilibration. Transcript-specific probes targeting Otx2 (NM_144841.5), Gata6 (NM_010258), and Cer1 (NM_009887.2) were custom-designed by Molecular Instruments and utilized at a final concentration of 4 nM in the probe hybridization buffer. Samples were then incubated overnight at 37°C with the probes. After the probe incubation period, the sample was subjected to four washes with probe wash buffer preheated to 37°C, followed by one wash with 5x SSC with 0.1% Tween 20 (SSCT). Subsequently, the samples were equilibrated in amplification buffer for 30 minutes at room temperature. Alexa Fluor-labeled amplifiers, at a final concentration of 60 nM, were applied along with Hoechst 33342 dye at 1 μg/ml, and incubated overnight at room temperature. To remove the amplifier solution, the samples were washed six times with 5x SSCT. Finally, stained BELAs were resuspended in PBS and mounted on an ibidi μ-slide for imaging. 2D cultures were mounted using 80% glycerol, 16% PBS, and 4% n-propyl-gallate.

2.10 Sytox stain

To detect dead cells, the samples were incubated in 0.5 µM Sytox green nucleic acid stain (Invitrogen) diluted in medium for 15 min. The Sytox-containing medium was replaced by a HEPES-buffered medium, and samples were immediately live imaged as z-stacks on a Leica SP8 confocal microscope with a 63x 1.4 NA lens. Sytox signal in BELAs was quantified by measuring the fluorescent intensity as integrated density (area x mean grey value) in the approximately middle plane.

2.11 Imaging

For recording of time-lapse movies, cells were seeded at a density of 30,000 cells/cm^2 on 6-well plates (Sarstedt) or on μ-slides (Ibidi) and allowed to attach for 1-2 hours. Cells were imaged using a 20x 0.5 NA air objective on an Olympus IX81 widefield microscope equipped with a stage top incubator (ibidi), LED illumination (pE4000, CoolLED), and a c9100-13 EMCCD (Hamamatsu) camera controlled by MicroManager software. To image a larger field of view grids were imaged, and the tiles stitched back together using the pairwise stitching plugin from FIJI (Preibisch et al., 2009).

Live VE cysts were imaged on a Leica DM IRB widefield microscope with a 20x 0.4 NA phase contrast objective.

Embryos, BELAs and 2D cultures, stained by immunochemistry or in situ HCR, were imaged on a Leica SP8 confocal microscope with a 63x 1.4 NA oil immersion objective.

For light sheet microscopy, stained BELAs were embedded in low melting agarose and positioned in 1.5 mm U-shaped capillaries (Leica). The capillaries were placed in 35 mm high glass bottom μ-dishes (Ibidi), fixed with blu tack (Bostik) and filled with water. For imaging, an HC Fluotar L 25x 0.95 NA water DLS TwinFlect 2.5 mm detection objective and an HC PL Fluotar 5x 0.15 NA illumination objective were used on a Leica TCS SP8 digital light sheet microscope.

All microscopy images were processed and analyzed using FIJI or Imaris.

2.12 Computational staining analysis

AVE marker expression and cell density were analyzed with an image processing pipeline originally developed by Pablo Casani Galdon (available at https://github.com/PabloCasaniGaldon/tilesegment; https://github.com/PabloCasaniGaldon/AVEDifferentiation).

For the analysis, large images were processed for easier handling. Images were padded into a square shape and divided into smaller tiles with specialized dimensions and overlapping regions. Within each tile, cells segmentation was performed using a

pretrained StarDisc2D model (Schmidt et al., 2018). Information such as outlines, masks, centers and diameters of the cell nuclei were then extracted. Smaller particles, such as cell debris, were identified based on their small diameters, detected through local minima in Gaussian mixture models fits and Kernel density estimation, and subsequently filtered out.

For fluorescence quantification of Cer1:H2B-Venus and OTX2, the mean grey values within each cell mask were computed. Histograms of the two markers revealed different distributions, leading to the application of distinct threshold methods. OTX2 exhibited a bimodal distribution, where the local minimum was used to set the threshold. However, Cer1:H2B-Venus displayed a more subtle distribution of fluorescent changes. Therefore, the threshold for Cer1:H2B-Venus was computed based on the negative control condition, using the mean of the top 1% mean grey values.

Local density calculation involved determining the nearest neighbors around each individual cell. Initially, the five closest cells to a center cell were located using the NearestNeighbor algorithm (Goldberger et al., 2004) and the mean distance was computed. The inverse of the squared mean of nearest neighbor distances was then plotted as average local density [μm^{-2}].

2.13 Flow cytometry

For flow cytometry analysis, cells were first singularized and then either directly resuspended in PBS containing 0.5% BSA (Merck) for live analysis or fixed in 4% paraformaldehyde for 15 minutes. Following fixation, the cells were washed with PBS to remove any residual fixative and incubated in PBS with 1% BSA and 0.25% Saponin (PBSap, Serva) for 30 minutes at room temperature to permeabilize the cell membranes. Next, cells were exposed to primary antibodies (see 2.8 Immunohistochemistry) that were appropriately diluted in PBSap and allowed to incubate overnight at 4°C. The following day, the cells were washed three times with PBSap to remove excess primary antibodies and then incubated with secondary antibodies, also diluted in PBSap, for at least one hour. Afterwards, samples were washed three times in PBSap, passed through a strainer to eliminate cell clumps and ensure a uniform suspension before being

promptly analyzed using an LSRII flow cytometer (BD Biosciences). A minimum of n=20,000 cells was analyzed for each condition in each biological replicate.

For the sorting of live cells, a FACS Aria Fusion (BD Biosciences) instrument was utilized. The flow cytometry data obtained was subsequently analyzed using FlowJo software (BD Biosciences).

2.14 Single-cell RNA sequencing

2.14.1 Sample preparation and collection of single cells

For single-cell RNA sequencing (scRNA seq), three samples were prepared: BELAs, Epi cysts, and VE cysts. BELAs were the primary focus of the analysis, while the cysts served as controls representing single-cell types incapable of communication with one another. 100-200 aggregates of BELAs and VE cysts were handpicked under a stereo microscope, adhering to criteria such as typical size and round shape. Within the VE cysts, some BELAs formed likely due to insufficient transgene induction, and care was taken to avoid selecting them during the sample preparation process. In the case of the Epi cyst sample, single cells were embedded in Matrigel drops and cultured for one day in 2i+LIF medium. The following day, the medium of all three sample types was simultaneously switched to N2B27, corresponding to the time point after the 8-hour doxycycline induction pulse for BEALs and VE cysts. After three days, Epi cysts were dissolved from Matrigel using a recovery solution (Corning). Next, cells from all three sample were singularized by incubating them with accutase at 37°C for 15 minutes, with intermittent mechanical dissociation. Subsequently, single cells were washed with PBS and resuspended in a small volume of PBS containing 0.5% BSA for downstream analysis.

2.14.2 Library preparation and sequencing

Aiming for 1,000 cells per cell type, which included 1,000 cells for each cyst sample and 2,000 cells for BELAs, cell counts were conducted, and the cells were

resuspended in an appropriate volume of H2O and RT master mix from Chromium Next GEM Single Cell 3' GEM, Library & Gel Bead Kit v3.1 (10x Genomics). The partitioning of cells with gel beads in emulsion was performed using a Chromium Controller (10x Genomics). Subsequently, reverse transcription, cDNA recovery and amplification, and sequencing library construction were carried out following the manufacturer's instructions (10x Genomics Chromium Next GEM Single Cell v3.1 Rev D protocol).

For cDNA amplification, 12 PCR cycles were selected, while 13 PCR cycles were chosen for index PCR. Concentration and insert size of sequencing libraries were determined using a BioAnalyzer High Sensitivity DNA Assay (Agilent). These libraries underwent paired-end Illumina sequencing on a NovaSeq6000 instrument with a read length of 150 bp.

Initially, sequencing was performed at a shallow depth targeting 10,000 reads per cell to ensure the capturing of an adequate number of high-quality single-cell transcriptomes. Following confirmation, deeper sequencing was conducted to achieve between 100,000 and 150,000 reads per cell.

2.14.3 Single cells RNA sequencing data analysis

All code used for analysis of the scRNA seq data was written by Max Fernkorn and can be found on GitHub at
https://github.com/Schroeterlab/BELAs_Schumacher_et_al.

Initially, CellRanger (10x Genomics, v4.00) was employed for demultiplexing, alignment to the mouse genome mm10 (GENCODE vM23/Ensemble 98, 10x Genomics), and read quantification. Further analysis was conducted in R using Seurat v4.1.1.42 (Hao et al., 2021). The analysis began with the filtering of cells with fewer than 4,000 distinct features and those with over 10% of mitochondrial genes. The count data was then normalized and scaled using SCTransform. For visualization through Uniform Manifold Approximation and Projection (UMAP) and clustering, shared cell populations were aligned across samples using Seurat's integration algorithm (Hao et al., 2021).

This algorithm employs reciprocal PCA to identify anchors. Differential expression analysis between the resulting clusters from Louvain clustering was performed using the FindMarker function, which operates on the SCTransform normalized data and sorts genes by fold-change.

Next, integration of clustered VE and AVE cells from the BELA scRNA seq data was accomplished using SCANPY (Wolf et al., 2018), leveraging scRNA seq data and annotations from an embryo data set specifically focused on AVE development (Thowfeequ et al., 2021). For this purpose, log1p-transforemd counts were utilized after normalization of the BELA data to 10,000 reads per cell. Asymmetric integration and label transfer were performed using the ingest method, and cell type proportions were visualized in R. Visualization was facilitated by a custom heatmap function based on pheatmap.

2.14.4 Cell-cell communication analysis

LIANA, a Ligand-receptor Analysis framework, was utilized to uncover active signaling pathways between Epi and VE cells, potentially investigating AVE differentiation (Dimitrov et al., 2022). Specifically, only transcriptomes from BELAs were analyzed, segregated into Epi and VE cell groups based on the clustering illustrated in Figure 19. Cluster 1 and 2 were assigned as Epi cells, while cluster 3 and 4 were attributed as VE cells. Subsequently, the consensus database for ligand-receptor interactions was mapped to its mouse ortholog genes using the omnipath database. Interactions were ranked according to their consensus rank obtained from LIANA, with the top 20 were plotted in an undirected adjacency graph.

2.15 Statistics

For each experiment, the number of repeats is specified in the figure legends, with N denoting the number of biological replicates and n indicating the number of independent samples within an experiment. Quantitative data are plotted as mean ± standard deviation (SD).

Statistical analysis was conducted using GraphPad Prism 8 (v8.4.3), using unpaired ratio t-tests or one-way Anovas with Bonferoni's multiple testing correction as specified in the figure legends. Significance levels are denoted by asterisks, with * indicating $p \leq 0.05$ and ** indicating $p \leq 0.005$.

3 Results

3.1 Bilayered embryo-like aggregates (BELAs)

The first steps of early embryonic development in a mouse embryo, akin to those of many other organisms, are critical as they lay the foundation for the body plan and the formation of all cell types that comprise the mature fetus.

In the initial days following fertilization, the embryo undergoes a rapid increase in cell number and differentiation into distinct cell types, including the embryonic lineage Epi and the two extraembryonic lineages TE and PrE (Figure 1A) (Arnold & Robertson, 2009). By this stage, the embryo is referred to as a blastocyst and begins the process of implantation into the uterus. Around E5.5, a significant architectural transformation occurs: the epiblast forms a cup-like structure with the TE progeny, known as the ExE, positioned above it, all surrounded by the PrE progeny, forming the VE. During this period, the initiation of the body plan commences through the formation of the AVE, a signaling center specified at the distal tip of the VE cells. This signaling center then migrates toward one side of the cup, determining the anteroposterior axis, ultimately leading to the onset of gastrulation.

Previous studies have demonstrated the ability to replicate such sequences of events from the peri-implantation embryo using embryo models made purely from stem cells (Amadei et al., 2021). While these models serve as powerful tools to study various aspects of the early embryonic development, their primary objective is to faithfully recreate an entire embryo with all of its lineages. Consequently, these models lack the capacity to uncover the autonomous potential of individual cell lineages for morphological and patterning processes.

3.1.1 Mixtures of Epi and PrE cells spontaneously form organized aggregates

In the embryo, the Epi and PrE cells differentiate from a common precursor, the ICM. To mimic this lineage decision and generate an embryo model consisting solely from Epi and PrE cells, I utilized mESCs containing a GATA4-mCherry inducible gene

construct (iGATA4, Figure 10A). This cell line has previously been demonstrated to differentiate into robust proportions of Epi and PrE cells upon transient GATA4 expression (Raina et al., 2021; Wamaitha et al., 2015).

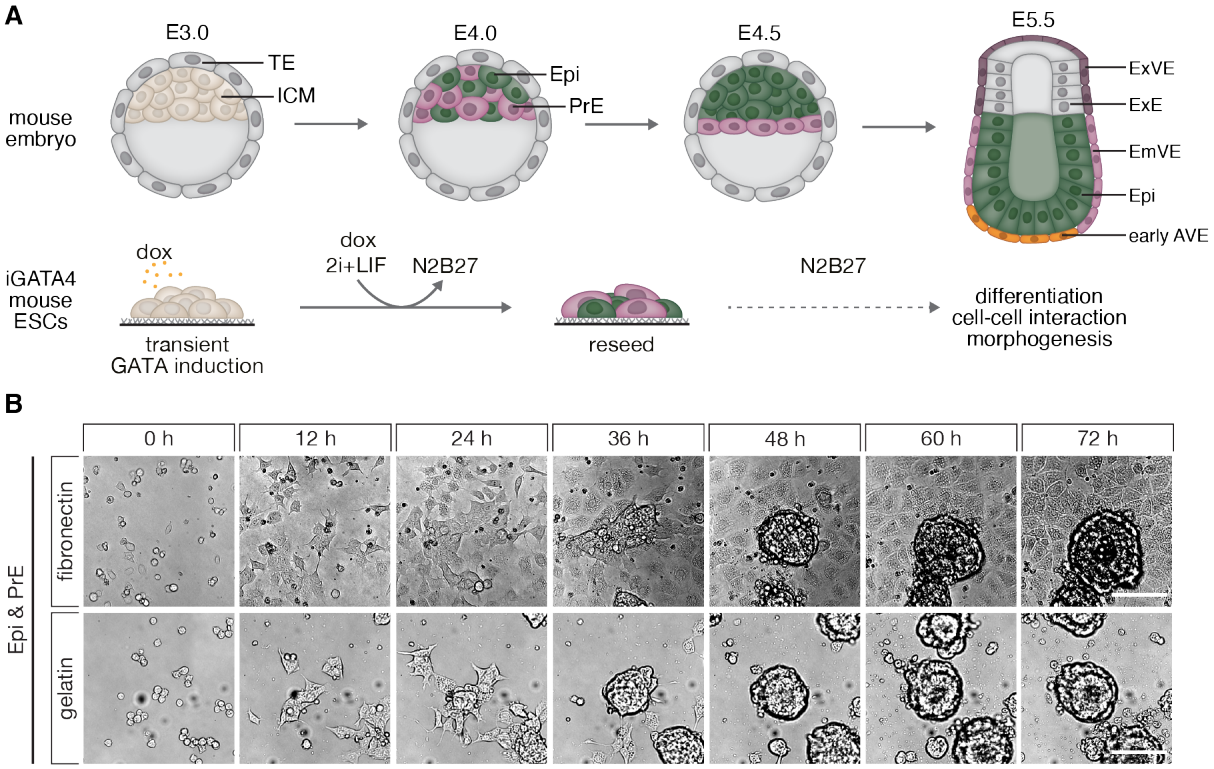

Figure 10: Epi and PrE cells spontaneously form aggregates.
A Schematic of the early mouse embryonic development from E3.0 to E5.5 (top) and experimental approach to study differentiation, cell-cell interaction and morphogenesis of Epi and PrE cells induced from iGATA4 mESCs (bottom). **B** Stills from time-lapse series of Epi and PrE cells growing in N2B27 medium on fibronectin (top) or gelatin (bottom). Scale bars: 50 μm.

The iGATA4 cells were cultured in defined media N2B27 supplemented with MEK inhibitor PD03, GSK3 inhibitor Chiron, and the cytokine LIF, referred to as 2i+LIF, to maintain their pluripotent state (Ying et al., 2008). To induce differentiation into a mixture of Epi and PrE cells, transient GATA4 expression was triggered by an 8-hour pulse of doxycycline (dox) in 2i+LIF, followed by a media change to pure N2B27. On the next day, 16-20 h after the dox pulse, the cells were reseeded at 30.000 cells per cm^2. When the tissue culture vessels were coated with a high concentration of fibronectin, part of the cells in the monolayer aggregated within two day, forming doomed-shape colonies (Figure 10B). These colonies exhibited organized structures consisting of two layers of

cells surrounding a central lumen. To promote observed cell-cell interactions of Epi and PrE cells, the adhesiveness of the coating was reduced by using a low concentration of gelatin instead of fibronectin. This time, nearly all cells contributed to the formation of bilayered aggregates which began detaching from the coating between 2 and 3 days. In contrast to growth on fibronectin, where aggregates remained attached, this suggested that yet unknown cell-cell interactions between Epi and PrE cells trigger a spontaneous formation of organized cell aggregates.

3.1.2 Bilayered aggregates resemble part of the peri-implantation embryo

To investigate the organization of the bilayered aggregates, I performed immunostainings for various cell types and structural markers. GATA6, a PrE/VE marker, was expressed in the outer cell layer of these closed spheres, while the inner cells displayed positive staining for the Epi marker OCT4 (POU5F1) (Figure 2A,B). Notably, the two layers seemed interconnected by a laminin-rich extracellular matrix, bound to by cells via integrin receptors (Figure 2C). Examination of apical polarity markers PODXL and pERM revealed polarization of both layers: inner Epi cells faced inwards with their apical domains, while outer PrE cells faced outwards, creating a basal-side to basal-side arrangement. This epithelial polarization was further confirmed by the localized expression of adherens junction molecule E-cadherin (CDH1) and tight junction-associated protein ZO-1 (Figure 2E). The distinctive morphology, comprising two opposing epithelial layers connected by a basement membrane and enclosing a central lumen, mirrors the Epi and VE compartments observed in peri-implantation embryos. Consequently, the cells within the aggregates appeared to progress from PrE to VE, resembling Epi and VE from the peri-implantation embryo. Due to their structure, the Epi/VE spheres were termed bilayered embryo-like aggregates (BELAs).

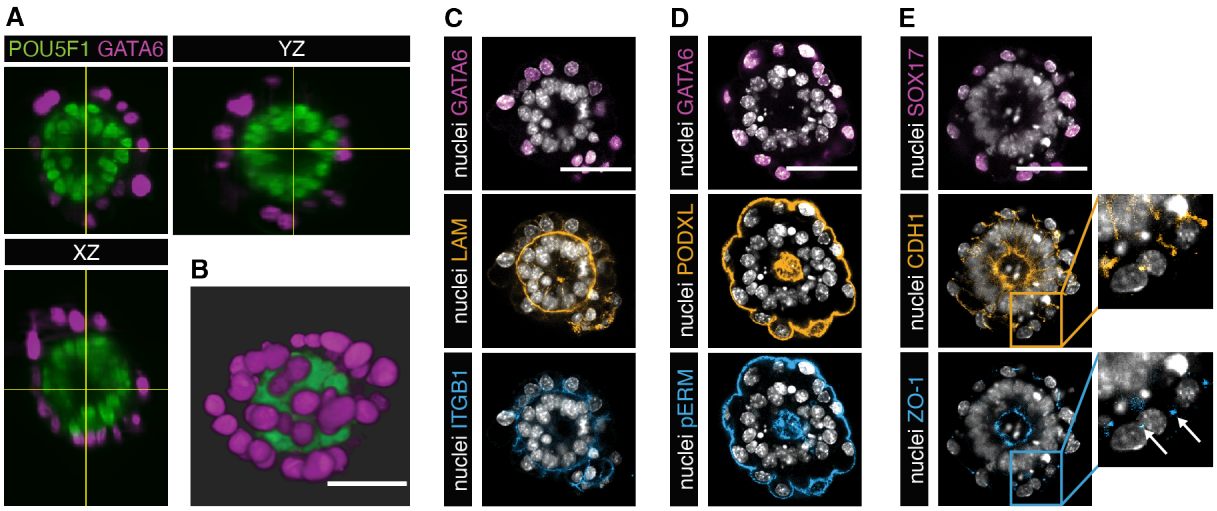

Figure 11: Aggregates resemble Epi and VE compartment of the peri-implantation embryo. **A,B** Light sheet microscopy recording of an Epi/PrE aggregate immunostaining shown as orthogonal views (A) and 3D volume rendering (B). POU5F1 (green) marks Epi identity and GATA6 (magenta) marks PrE/VE identity. Scale bar: 50 μm. **C,E** Epi/PrE aggregate immunostainings shown as sections. GATA6 and SOX17 (magenta) mark PrE/VE identity, PODXL (orange) and pERM (blue) mark the apical side of polarized cells, LAM (orange) and ITGB1 (blue) show the basement membrane/integrin connection and CDH1 (orange) and ZO-1 (blue) are epithelial markers. Arrows show punctuate ZO-1 staining as characteristic for tight junctions (E, inset). Scale bars: 50 μm.

3.2 Epi and PrE cells exchange signals for survival and morphogenesis

3.2.1 PrE cells depend on FGF4 from the Epi

The interaction of Epi and PrE cells triggers the spontaneous formation of BELAs that resemble part of the peri-implantation embryo. To identify the driver of this morphogenesis, I differentiated the iGATA4 mESCs into single populations of Epi and PrE cells (Figure 12A). For an Epi-only culture, the medium was changed from 2i+LIF to N2B27 without a prior dox pulse. To establish a PrE-only culture, a strongly inducible iGATA4 clone was used or the dox pulse was extended for 24 hours regardless of the media change to N2B27. 16 hours after switching to N2B27, the cells were reseeded onto gelatin-coated tissue culture vessels and recorded for three days using a widefield microscope with a stage top incubator. While an induced mixed population of Epi and PrE cells served as control group and formed BELAs over the time course of 3 days (top row), the single Epi and PrE cells experienced extensive cell death (row 2-3). To

assess cell survival, I conducted trypan blue exclusion assays 72 hours after reseeding to count the remaining living cells. All conditions started with the same initial cell count per well, regardless of whether the cells were seeded as mixture or pure populations. Compared to the control, the number of Epi cells decreased by approximately 50%, while almost no living PrE remained (Figure 12C). This drastic cell death observed for the PrE cells could be attributed to the absence of FGF4, which is typically secreted by Epi cells and is known to support PrE differentiation and survival (Raina et al., 2021; Wilder et al., 1997). Remarkably, supplementation of FGF4 into N2B27 rescued the PrE cells from extensive cell death and, surprisingly, resulted in similar non-adherent aggregate formation as observed in mixed cultures containing Epi and PrE cells (Figure 12A,B bottom row). These spheres contained only one cell layer that encapsulated a central lumen and were a bit smaller in size compared to BELAS, 93.4±18.8 μm to 112.8±30.4 μm respectively (Figure 13A,B).

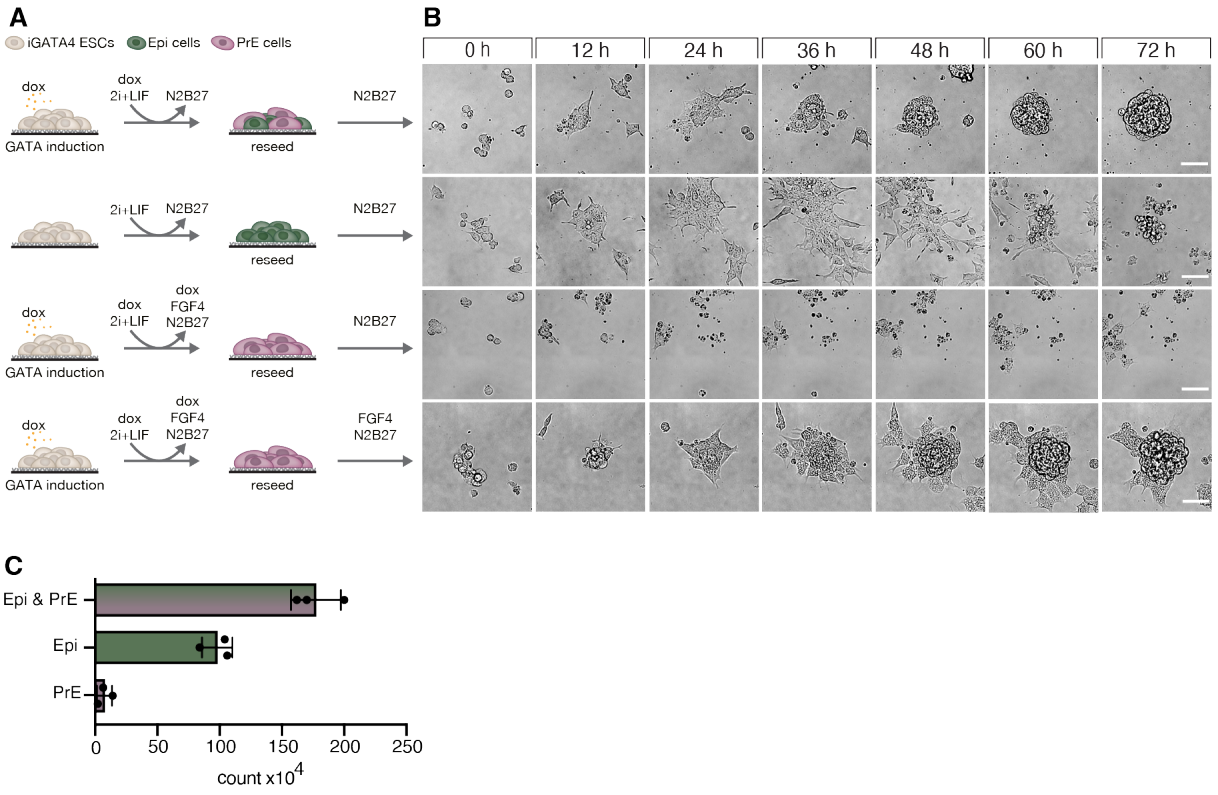

Figure 12: Epi and PrE cells exchange mutual survival signals.
A Schematic of experimental protocol to differentiate mixed populations of Epi and PrE cells, as well as pure populations of the pure cell types. **B** Stills from time-lapse series of differentiated cells shown as in (A) after reseeding in N2B27. Scale bars: 25 μm. **C** Quantification of living cells of a Epi and PrE mixed culture or pure cultures after 72 hours in N2B27. Bars indicate mean ±SD.

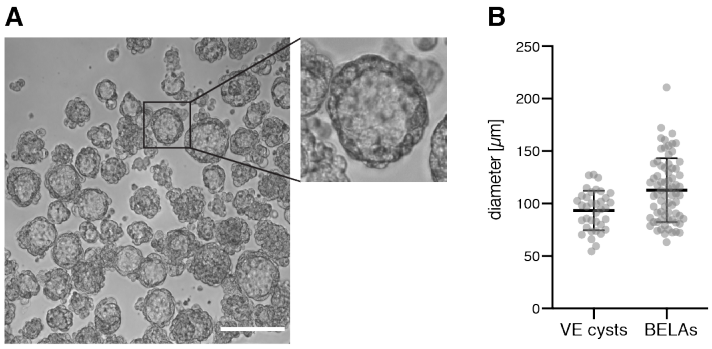

Figure 13: Induced PrE cells spontaneously organize into VE cysts.
A VE cysts formed from induced iGATA4 mESCs in N2B27 supplemented with FGF4. Scale bar: 200 μm. **B** Sizes of detached BELAs (n=72) and VE cysts (n=36) grown for three days after reseeding induced cells. Bars indicate mean ±SD.

Given their striking resembles to BELAs, I stained these structures for the same markers to investigate their organization. Although they contained no inner Epi cells, the single layer of GATA6-positive PrE cells secreted laminin towards the interior of the cysts and exhibited polarization, with the apical markers PAR6, PODXL and pERM confined to the outside of the cysts (Figure 14A,B). The presence of an epithelial organization was confirmed by the localized expression of the markers CDH1 and ZO-1 (Figure 14C). These observations collectively indicate that the spheres harbor the same structural organization as the outer VE layer of BELAs, concluding that the PrE cells adopted a VE identity. Furthermore, it appears that only FGF4 but not Epi cells per se, are necessary for the formation of this polarized cystic structure, which I term VE cysts.

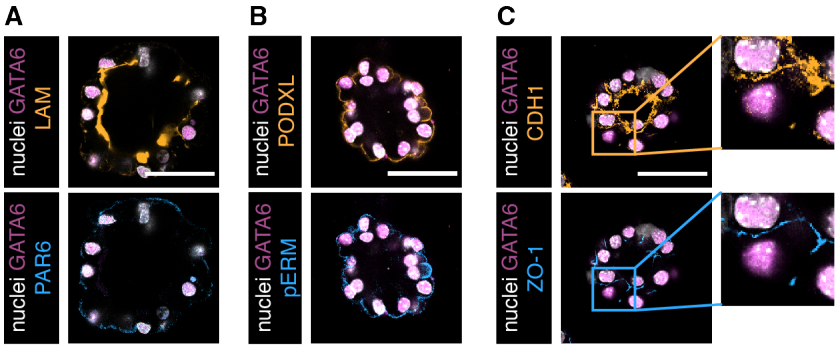

Figure 14: VE cysts are BELAs without the inner Epi core.
A-C VE cysts immunostainings shown as sections. GATA6 (magenta) marks PrE/VE identity, LAM (orange) marks the 41extracellular matrix, PAR6 (blue), PODXL (orange) and pERM (blue) mark the apical side of polarized cells, and CDH1 (orange) and ZO-1 (blue) are epithelial markers. Scale bars: 50 μm.

3.2.2 Epi cells require binding to extracellular matrix

The outer VE cells in BELAs depend on FGF4 from the Epi cells, which prompted the question of the specific factor provided by the PrE/VE cells that results in survival and patterning of the Epi cells. Culturing Epi cells in N2B27 on a low concentration of gelatin led to extensive cell death (Figure 12B,C), suggesting a lack of binding sites to extracellular matrix proteins, which PrE/VE cells, known to express for example high levels of laminin, may provide. To test this hypothesis, I mutated the beta 1 integrin gene (*Itgb1*) in the iGATA4 mESCs using the CRISPR/Cas9 system (Figure 15A) resulting in loss of the start codon ATG in the second exon for both alleles. The mutation of *Itgb1* leads to the disability of the cells to bind to extracellular matrix proteins as fibronectin (Bouvard et al., 2001), so that the Itgb1 mutant cells where cultured on feeder cells or vitronectin. Figure 15B shows cultivation of *Itgb1* mutant cells on a feeder cell with only the feeder cell expressing ITGB1.

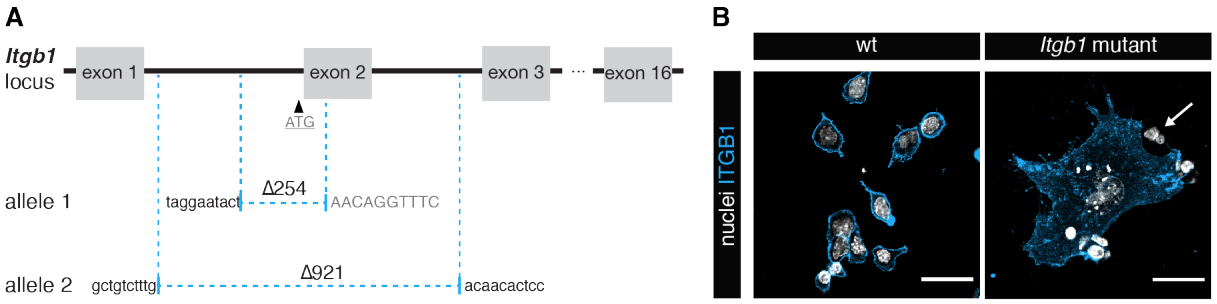

Figure 15: Validation of *Itgb1* mutant mESCs.
A Schematic illustrating the two *Itgb1* alleles present in the *Itgb1* mutant mESC line, identified through Sanger sequencing of PCR amplicons specifically designed to encompass the *Itgb1* second exon. **B** Immunostaining for ITGB1 (blue) in wt (left) and *Itgb1* mutant cells (right). ITGB1 signal in the right panel is from a single wt feeder cell. Co-culture with feeder cells was required to avoid detaching of *Itgb1* mutant cells from the tissue culture plate. Scale bars: 25 μ m.

To avoid universal consequences from a *Itgb1* mutation in all cells of BELAs, I opted to differentiate Epi *Itgb1* mutant and PrE wildtype (wt) separately and then combine them in a ratio of 30-70 upon reseeding. The used ratio mirrors the proportions of the two cell types obtained through transient expression of GATA4 and differentiation in N2B27 (Figure 10A) (Raina et al., 2021). At first glance, BELAs appeared to form relatively normally and within three days after reseeding the induced cells, floating

aggregates became apparent. However, extending the culture for one additional day revealed a notable presence of dying cells within the *Itgb1* mutant Epi compartment, as indicated by Sytox staining, a nucleic acid stain that penetrates only cells with compromised plasma membranes (Figure 16A). Sytox signal intensity was quantified using the middle section of a BELA, measuring the product of intensity mean and area (Figure 16B). Mixed BELAs from Epi and VE wt cells exhibited very low levels of Sytox signal, with many BELAs showing no signal at all, while BELAs derived from *Itgb1* mutant Epi and PrE wt cells displayed significantly higher Sytox intensities mimicking the lethal phenotype in chimeric embryos (Molè et al., 2021).

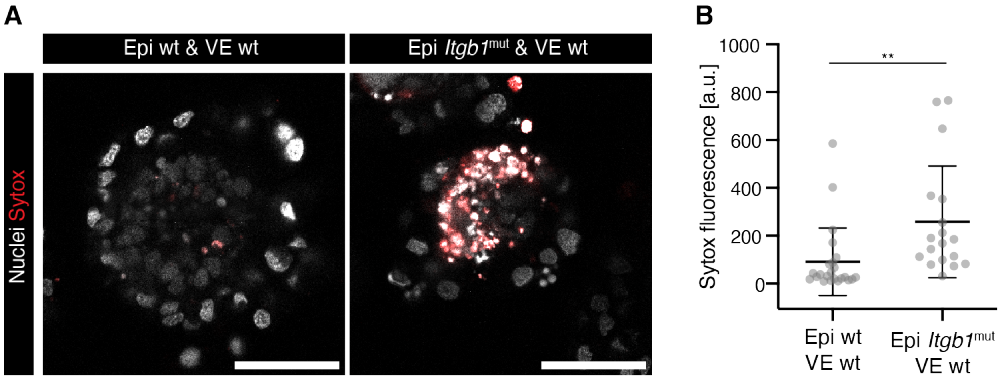

Figure 16: *Itgb1* mutant Epi cells show extensive cell death in BELAs.
A Immunostainings of BELAs shown as sections. BELAs were formed from separately differentiated Epi (wt or *Itgb1*^{mut}) and PrE (wt) cells that were mixed together when reseeded and cultured for four days. Sytox marks dead and dying cells (red). Scale bars: 50 μm. **B** Quantification of Sytox intensity per BELA (Epi wt & VE wt n=23, Epi *Itgb1*^{mut} & VE wt n=18) measured as integrated density in the approximate middle section. Bars indicate mean ±SD. ** indicates $p \leq 0.005$, determined by a two-tailed, unpaired t-test.

To identify an earlier-present phenotype and to see whether there are additional effects from VE cells, I compared *Itgb1* mutant Epi cells in BELAs to cells that were embedded in purified extracellular matrix (Matrigel) and cultured for two days in N2B27(Figure 17). The connection to Matrigel should mimic binding to the extracellular matrix of PrE/VE cells in the absence of other signals. Under these conditions, Epi wildtype cells are reported to form epithelial cysts with a central lumen (Epi cysts) (Bedzhov & Zernicka-Goetz, 2014). iGATA4-induced cells were sorted based on high GATA4-mCherry expression levels before mixing, ensuring that no *Itgb1* wildtype cells contributed from the Epi compartment. The reason was a potential loss of an *Itgb1* mutant

phenotype because mixtures of wildtype and *Itgb1* mutant cells have been reported to support epiblast morphogenesis in the embryo (Fassler & Meyer, 1995).

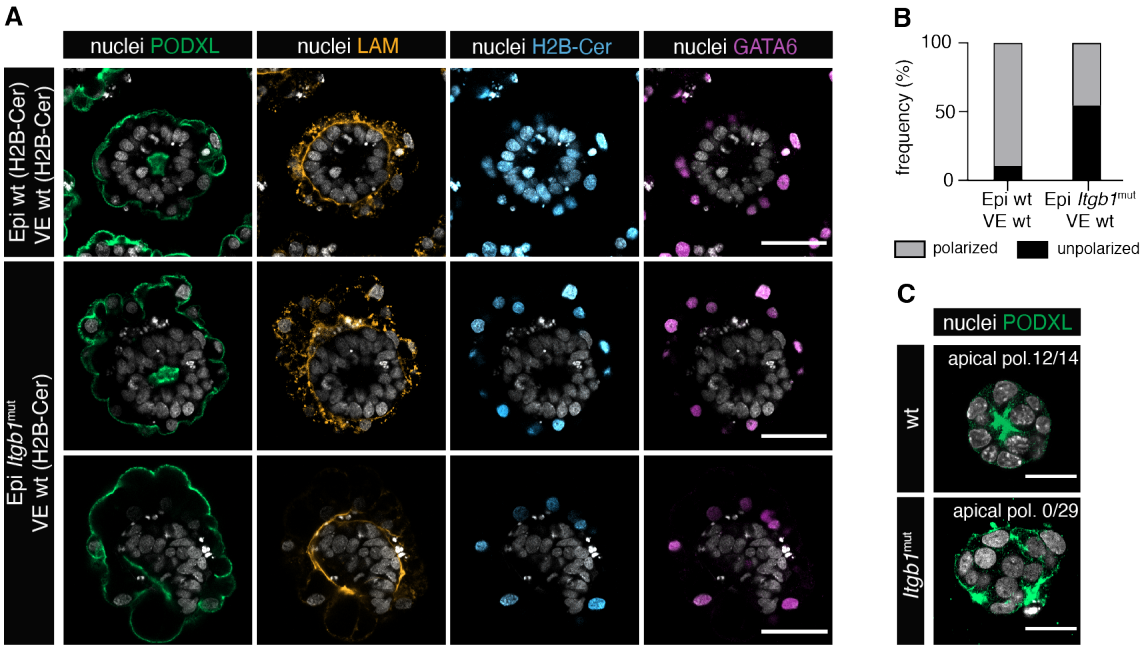

Figure 17: Integrin plays an important role in patterning the Epi cells.
A Immunostainings of BELAs shown as sections. BELAs were formed from separately differentiated Epi (wt or *Itgb1*^{mut}) and PrE (wt) cells that were mixed together when reseeded. PODXL marks the apical polarization (green), LAM marks the extracellular matrix (orange), H2B-Cerulean marks the wildtype cells and GATA6 marks PrE/VE identity. **B** Quantification of the number of BELAs with a polarized Epi compartment. n ≥ 40. **C** Immunostaining of wildtype and *Itgb1*^{mut} iGATA4 mESCs that were embedded as single cells in Matrigel gel and cultured for two days. 12/14 wildtype and 0/29 *Itgb1*^{mut} Epi cysts showed apical polarization facing the inside of the cyst. Scale bars: 25 μm.

Mixing *Itgb1* mutant Epi with wildtype PrE cells resulted in a formation of BELAs with an outer polarized VE layer surrounding the inner Epi cells and visible laminin expression as a ring between the two cell types (Figure 17A). Around 50% of BELAs failed a proper organization of a polarized Epi compartment, compared to only 10% of wildtype BELAs (Figure 17B). However, none of the *Itgb1* mutant Epi cysts showed proper lumenogensis and polarization. Single cells stained positive for the apical marker PODXL could be observed, but the cells seemed to be unable to coordinate their polarization sides collectively towards the inside of the cysts. These results recapitulate the finding that coordination of polarization and lumenogenesis of Epi cells in Matrigel depends on the binding of β1-integrins to the surrounding extracellular matrix (Bedzhov & Zernicka-Goetz, 2014). Since *Itgb1* mutant cells in BELAs couldn't mimic

this phenotype in Matrigel, I speculate that *Itgb1* is important for patterning the Epi compartment, but that there are also additional patterning cues from the VE layer in BELAs that are absent in Matrigel.

3.3 scRNA seq reveals AVE differentiation in BELAs

To investigate a potential influence of Epi and VE cells towards one another and especially AVE differentiation, a single cell RNA sequencing (scRNA seq) experiment was conducted. Three samples were included: BELAs, as well as VE cysts and Epi cysts, serving as controls (Figure 18A). The latter two represent the single compartment of BELAs without any contact of Epi and VE cells. BELAs and PrE cysts were formed as described above. Epi cysts were obtained by first seeding single cells in Matrigel drops in 2i+LIF, followed by media change to pure N2B27 after one day and further culture for three days.

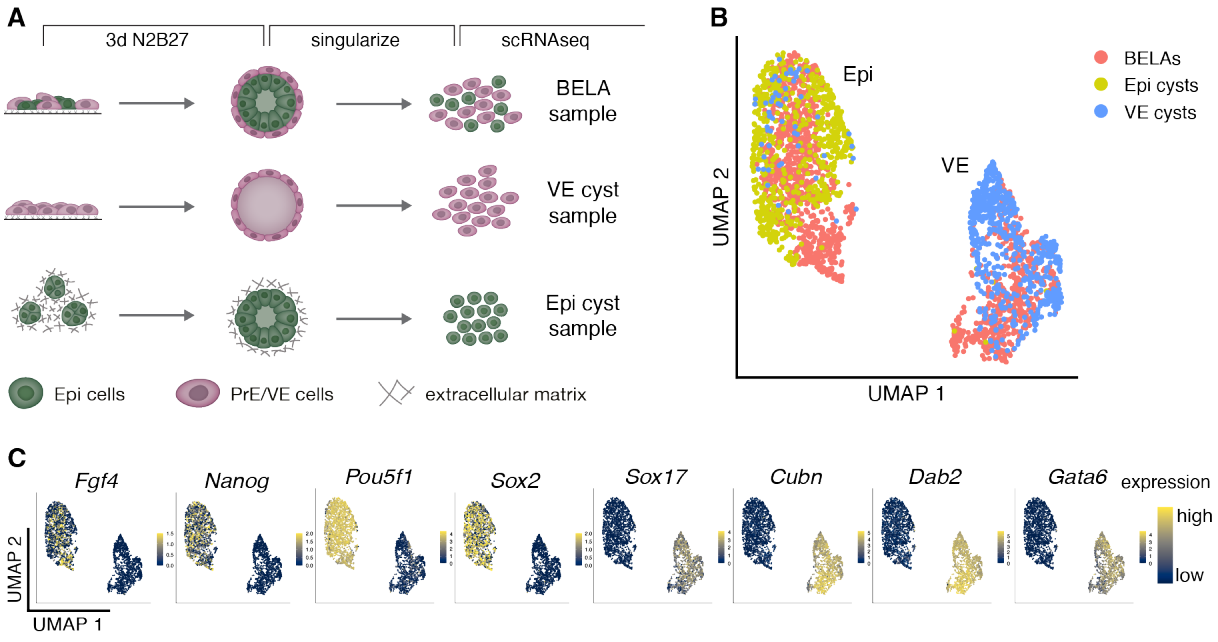

Figure 18: Single cell RNA seq of BELAs and its single compartments.
A Schematic experimental approach of sample preparation that were used for single cell RNA seq. **B** UMAP of single cell transcriptomes from cells prepared as in A. Colors indicate sample's origin. **C** Expression levels of markers for PrE/VE (*Sox17*, *Cubn*, *Dab2* and *Gata6*) and for Epi (*Fgf4*, *Nanog*, *Pou5f1* and *Sox2*). To better visualize the expression of some genes, expression levels above ln ≥ 1.5 for Fgf4 and ln ≥ 2 for Nanog and Sox2 are shown in yellow.

Transcriptome visualization using a UMAP plot displayed two groups of dots, each dot representing the transcriptome of a single cell (Figure 18B). The first group primarily comprised cells from Epi cysts and BELAs, while the second group contained the remaining BELA cells and most of the cells from VE cysts. Looking at marker genes for Epi (*Fgf4*, *Nanog*, *Pou5f1* and *Sox2*) and VE identity (*Sox17*, *Cubn*, *Dab2* and *Gata6*) confirmed the assumption that the cells were separated based on their identity in the UMAP space (Figure 18C). The presence of cells with origin from the VE cysts within the group of Epi cells indicates that some cells were resistant to differentiation towards a PrE identity due to insufficient GATA4-mCherry induction levels (Raina et al., 2021).

3.3.1 VE cells segregate potential AVE cluster

The spatial separation observed in the UMAP plot and the grouping based on Epi or VE identity prompted me to hypothesize that applying Louvain clustering for sorting single-cell transcriptomes into four clusters would primarily segregate BELA cells into Epi and VE categories (Figure 19).

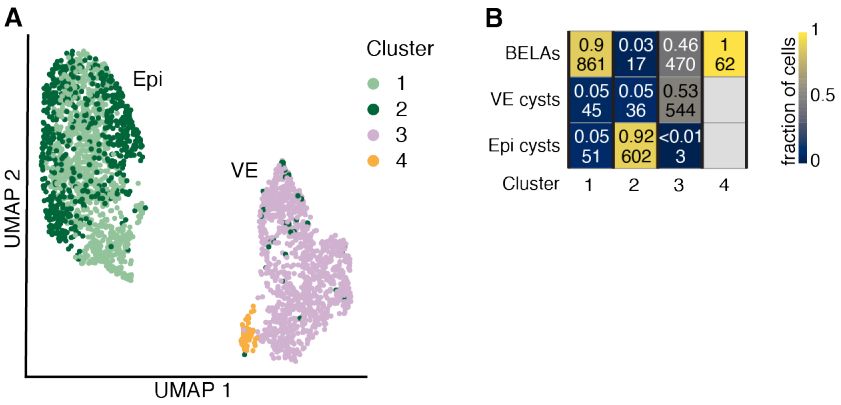

Figure 19: VE cells do not sort based on their origin.
A UMAP representation of single-cell transcriptomes (same as in Figure 18B) after Louvain clustering assigned the cells into four clusters. Colors indicate cluster number. **B** Quantification of the fractions of cells from BELAs, Epi cysts and VE cysts in each of the four different clusters from A.

While this assumption held true for Epi cells, effectively clustering them according to their sample origin (clusters 1 and 2), VE cells followed a different pattern (Figure 19A,B). They separated into a large cluster (cluster 3), containing VE cells from both VE cysts and BELAs, and a notably smaller cluster (cluster 4) comprising 62 BELA VE

cells. This implied that the varying formation methods for Epi cells in Epi cysts, where cells have only contact to an artificial extracellular matrix, and in BELAs, where cells bind to extracellular matrix of VE cells, led to substantial transcriptomic differences, prompting their segregation. In contrast, VE cells from the two samples showed higher similarity and sorted into clusters not exclusively determined by sample origin. Looking into the differentially expressed genes between cluster 3 and 4 (VE clusters) revealed a downregulation in cluster 4 of many genes related to extracellular matrix components such as *Hspg2*, *Spock1*, *P4ha2* and *Fst* (Figure 20A).

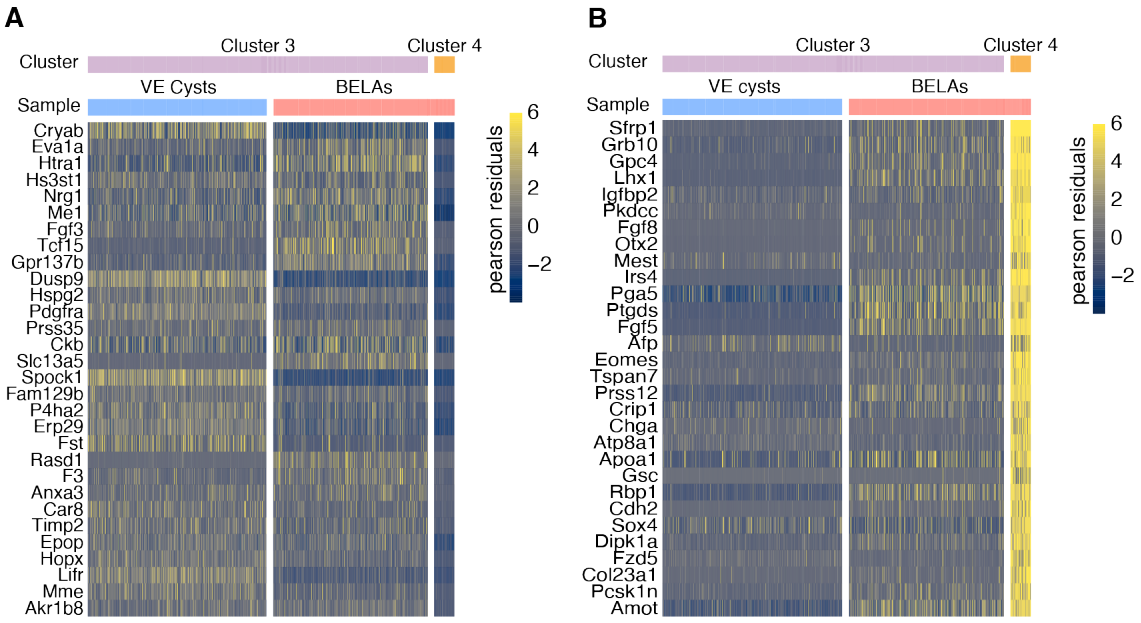

Figure 20: scRNA seq identifies an AVE cluster within VE cells.
A,B Heatmaps showing the 30 most downregulated (A) and upregulated (B) genes between the VE cells of cluster 3 and 4 from Figure 19, ordered by log2-log change. Single-cell expression is shown as the Pearson residual of the normalized counts.

Of particular interest was the collection of upregulated genes in cluster 4, including genes such as *Sfrp1*, *Lhx1*, *Otx2* and *Eomes* (Figure 20B). These genes are typically associated with expression in AVE cells of the embryo, suggesting an adaptation of the cells in cluster 4 toward that specific cell type (Nowotschin et al., 2013; Rivera-Pérez & Hadjantonakis, 2014). Importantly, this suggests that only the VE cells from BELAs, but not from VE cysts, were capable of AVE differentiation, possibly due to their interaction with Epi cells.

3.3.2 AVE cells from BELAs resemble transcriptome of an E6.25 AVE

To validate the discovery that the VE cells of cluster 4 adopted an AVE identity (Figure 19A), the VE cells of BELAs from cluster 3 and 4 were integrated with an embryonic data set focusing specifically on the differentiation of AVE cells from E5.5 and E6.25 (Thowfeequ et al., 2021). UMAP representation after integration revealed that BELA VE cells mostly co-localized with E6.25 Epi-VE and AVE, with a small proportion also co-localizing with E5.5 Epi-VE and AVE (Figure 21A,B). To quantify the resemblance of BELA VE cells to various cell types and developmental stages within the embryo dataset, the cell type and stage labels from the reference dataset were transferred to the BELA VE cells and the frequency plotted as a heatmap (Figure 21C).

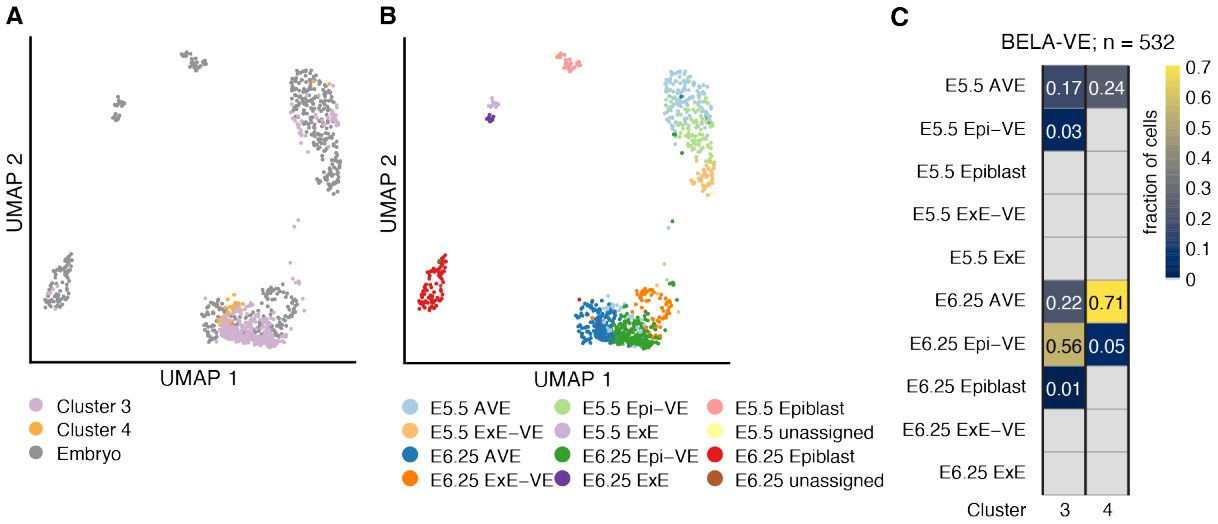

Figure 21: BELA-VE predominantly represents embryonic Epi-VE and AVE from E6.25.
A UMAP of single-cell transcriptomes only from BELA-VE (BELA cells in cluster 3 and 4 from Figure 19A) after integration with scRNAseq data covering the embryonic development, especially AVE differentiation, from E5.5 and E6.25 (Thowfeequ et al., 2021). **B** Same UMAP as in A, but visualizing the different cell types after integration and label transfer according to the cell type annotations from Thowfeequ et al., 2021. **C** Quantification of the fractions of BELA VE cells from cluster 3 and 4 that are assigned to specific cell types and time points from the embryo.

First of all, almost none of the BELA VE cells were labelled as Epiblast, extraembryonic ectoderm (ExE) and not even extraembryonic VE (ExE-VE), confirming their embryonic VE identity. Upon closer examination, as expected, 95% of the cells from cluster 4 were labelled as AVE, with 24% assigned as E5.5 AVE and 71% as E6.25 AVE. Unexpectedly, the cells of cluster 3 were not solely labelled as E5.5 and E6.25 Epi-VE

(3% and 56%, respectively), but also received the label of E5.5 and E6.25 AVE (17% and 22%, respectively). All together, these results indicate that within the VE cells of BELAs, a small proportion differentiates into a heterogenous population of AVE cells.

3.3.3 AVE marker expression is spatially restricted in BELAs

scRNA-seq uncovered the adaption of an AVE identity by some VE cells in BELAs, but it offered no insights into their distribution across individual BELAs. To answer that question, I performed immunostainings to visualize the AVE cells in BELAs (Figure 22A,B). In the embryo, Cer1 specifically marks the AVE, while Otx2 displays a broader expression, encompassing both the AVE and parts of the emVE (Hoshino et al., 2015). Gata6 marks the entire VE. As a consequence, Otx2 and Cer1 expressions are selected as indicators for the broader and more specific AVE regions, respectively. Initially, I stained BELAs for OTX2, which also marks Epi cells, and examined its co-localization with GATA6 which could be seen in 28 out of 33 BELAs (Figure 22A). Additionally, I identified AVE cells as OTX2-expressing cells outside the laminin ring to ascertain that these are not Epi cells.

Using in situ HCR staining allowed for the staining of *Cer1* mRNA, as the protein's expression and immediate secretion outside of the cells make it challenging to stain it directly. Comparable outcomes were achieved through in situ HCR staining for *Otx2* and *Cer1* mRNA, with 27 out of 36 BELAs displaying cells co-expressing *Otx2* and *Gata6* mRNA, and 10 out of 36 BELAs showing cells co-expressing *Cer1* and *Gata6* mRNA pointing to a heterogenous population (Figure 22C). Looking into the temporal dynamics of AVE marker expression in BELAs, revealed the transient nature of the AVE region (Figure 22C). The markers *Cer1* and *Otx2* could first be found two days after reseeding the induced cells and latest on the fourth day. The highest number of BELAs expressing both AVE markers was reached at day three with around 60% expressing *Otx2* and 20% *Cer1*. Overall, it could be seen that most BELAs contain an AVE region and that this AVE region recapitulates the transient nature of the AVE in the embryo (Thowfeequ et al., 2021).

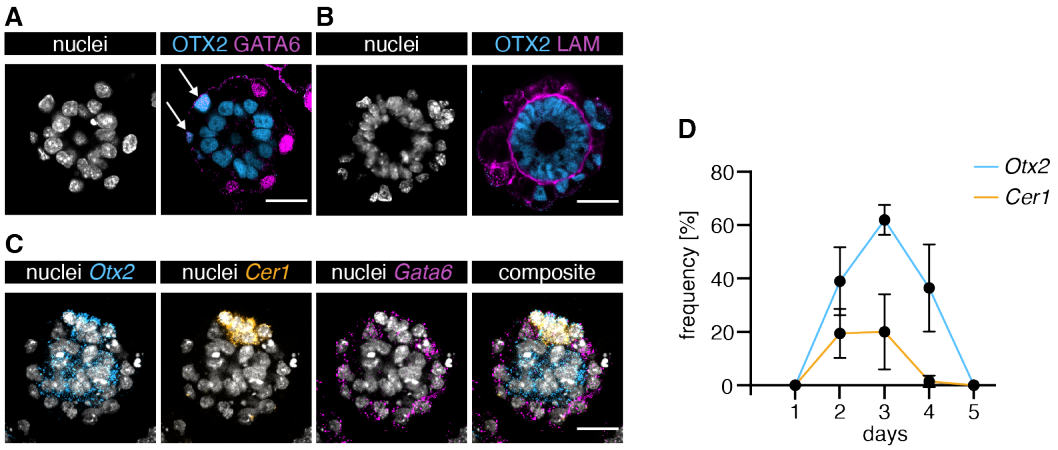

Figure 22: Spatially restricted AVE markers are transiently expressed.
A BELA immunostaining shown as a section for the Epi and AVE marker OTX2 (blue) and the PrE/VE marker GATA6 (magenta). 28/33 showing co-expression of OTX2 with GATA6, arrows pointing to co-expressing cells. Scale bar: 25 μm. **B** BELA immunostaining shown as a section for the Epi and AVE marker OTX2 (blue) and the extracellular matrix marker LAM (magenta) to distinguish the outer layer of VE/AVE cells. Scale bar 25 μm. **C** BELA in situ HCR staining shown as a section for the Epi and AVE marker Otx2, the AVE marker Cer1 and the PrE/VE marker Gata6. 27/36 showing co-expression of *Otx2* with *Gata6* and 10/36 showing co-expression of *Cer1* with *Gata6*. Scale bar: 25 μm. **D** Quantification of number of BELAs that show expression of AVE marker genes in the outer VE cells on different days after reseeding the induced cells. N = 2, n ≥ 18, except for day 1 n = 10. Error bars indicate SD.

To enhance the visualization of the AVE region, particularly CER1, I made an AVE reporter cell line based on the previous design of (Mesnard et al., 2004) within the background of the inducible iGATA4 cell line. The construct featured the reporter H2B-Venus expressed under the control of a 4kb long Cer1 promotor region upstream of its start codon, along with a puromycin resistance cassette for selection controlled by a constituent PGK promoter (Figure 23A). The Cer1:H2B-Venus reporter was validated by co-localization with *Cer1* mRNA (Figure 23B). Light-sheet imaging of Cer1:H2B-Venus reporter BELAs revealed a spatially clustered domain of H2B-Venus expressing cells outside of the POU5F1 expressing Epi compartment (Figure 23C,D). This observation is surprising because, according to the AVE model Epi cells should induce AVE differentiation throughout the VE layer in the absence of an ExE (Rodriguez, 2005; Yamamoto et al., 2009). This prompts the question regarding the specific regulation of AVE differentiation in BELAs.

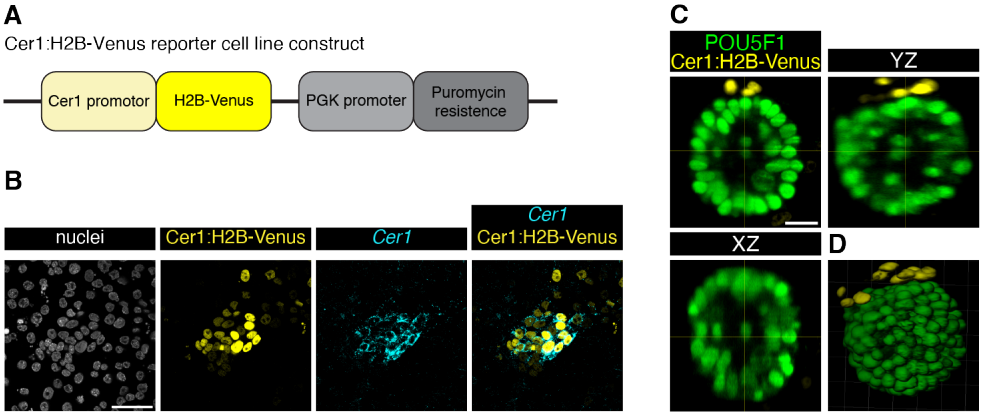

Figure 23: AVE reporter cell line shows spatially restricted AVE cells in BELAs.
A Schematic of Cer1:H2B-Venus reporter construct that was genetically integrated into the iGATA4 mESCs. **B** In situ HCR staining to validate the AVE reporter Cer1:H2B-Venus for Cer1 co-expression. Scale bar: 50 μm. **C,D** Light sheet microscopy recording of a BELA carrying the Cer1:H2B-Venus reporter shown as orthogonal views (C) and 3D volume rendering (D). POU5F1 (green) marks Epi identity. Scale bar: 25 μm.

3.4 Nodal is necessary and sufficient for AVE differentiation

3.4.1 Inhibition or mutation of Nodal abrogates AVE differentiation

In the ebryo, it has been demonstrated that Nodal, secreted from the Epiblast, serves as the essential signal for inducing AVE differentiation in the overlying VE cells (Brennan et al., 2001). To investigate whether Nodal acts in the same manner in BELAs or whether BELAs use a different trajectory to induce an AVE, LIANA, a ligand-receptor analysis framework, was used. This framework matched expressed ligands from the Epi cells with corresponding expressed receptors from VE cells according to consensus database, and the top 20 interactions were plotted (Figure 24A). Among these interactions, ligand-receptor pairs could be identified associated with extracellular matrix, FGF and Eph-Ephrin, as well as Nodal signaling depicted as the Nodal receptors Acvr1b and Acvr2, and the Nodal co-factor Tdgf1 (circled cluster, Figure 24A). Given its critical role in the embryo, I selected Nodal as the primary candidate and formed BELAs in the presence of the Nodal receptor inhibitor SB431542 (SB43). Under this condition, none of the in situ HCR stained BELAs showed any indication of *Otx2*

or *Cer1* expression in the outer VE cells which were marked by *Gata6* expression (Figure 24B,C).

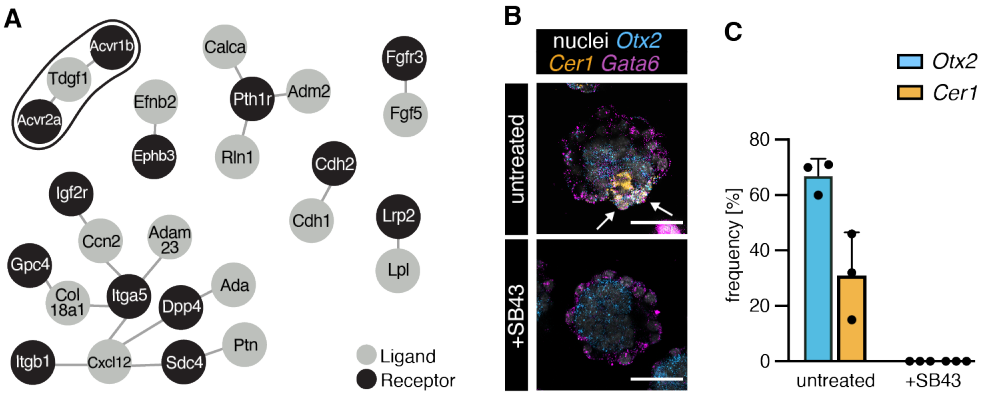

Figure 24: BELAs fail to form an AVE in the presence of Nodal inhibitor.
A Cell communication diagram from a LIANA (Dimitrov et al., 2022) analysis showing the top 20 potential interactions between Epi-expressed ligands and VE-expressed receptors. Circled cluster indicates Nodal signaling. **B** In situ HCR staining of untreated and SB43-treated (Nodal inhibitor) BELAs for the Epi and AVE marker *Otx2* (blue), the AVE marker *Cer1* (orange) and the VE marker *Gata6* (magenta). Arrows indicate co-expression of all three markers. Scale bars: 50 μm. **C** Quantification of number of untreated and SB43-treated BELAs that show expression of the AVE marker genes *Otx2* or *Cer1*. N = 3, n ≥ 20 per condition. Error bars indicate SD.

To further validate the findings, the Nodal locus was mutated in the iGATA4 cell line. Exon 2 was targeted using with two CRISPR guides aimed to excise a fragment exceeding around 200bp (Figure 25A). Subsequent generation of BELAs using these *Nodal* mutant iGATA4 mESCs indeed confirmed the earlier observation. Among the 21 BELAs analyzed, none exhibited OTX2-expressing AVE cells, as assessed by the absence of such cells outside the laminin ring (Figure 25B).

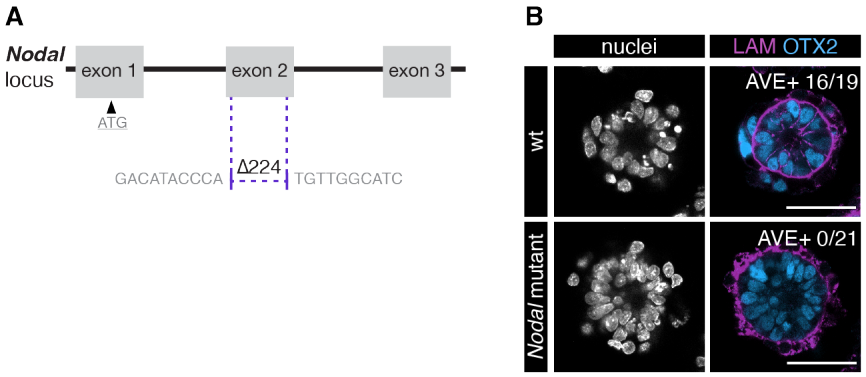

Figure 25: *Nodal* mutant BELAs fail to form an AVE.
A Schematic illustrating the *Nodal* locus mutation present in the iGATA4 mESC line, identified through Sanger sequencing of PCR amplicon specifically designed to encompass the *Nodal* second exon. **B** Immunostaining of BELAs formed from wildtype and *Nodal* mutant iGATA4 mESCs for the Epi and AVE marker OTX2 (blue) and the extracellular matrix marker LAM (magenta). 16/19 wildtype and 0/21 *Nodal* mutant BELAs showed OTX2+ cells outside the laminin ring. Scale bars: 50 μm.

3.4.2 Addition of ActivinA during VE induction triggers AVE differentiation

Having demonstrated the necessity of Nodal for AVE differentiation in BELAs, I sought to investigate whether Nodal signals derived from the Epi cells alone could act as sufficient trigger to induce an AVE. Therefore, the Nodal-secreting Epi cells were substituted with recombinant ActivinA protein to activate the Nodal signaling pathway in a pure culture of PrE cells (Figure 26A). Hence, the iGATA4 mESCs, which carry the Cer1:H2B-Venus reporter, were stimulated with an 8-hour pulse of dox in 2i+LIF medium. Subsequently, the medium was switched to N2B27, with the dox pulse continued in conjunction with FGF4, and different concentrations of ActivinA. FGF4 was used to promote the induction with dox towards the PrE fate and to sustain the viability of the cells. After 16 hours, the cells were reseeded onto a high concentration of fibronectin to generate a 2D VE layer and further cultured for three days in N2B27 supplemented with FGF4 and varying concentrations of ActivinA. Notably, treating the cells with recombinant ActivinA let to the dose-dependent expression of both the reporter Cer1:H2B-Venus and OTX2, with a higher number of cells expressing OTX2 compared to Cer1:H2B-Venus (Figure 26B). However, such expression was absent when no Activin was applied. Interestingly, AVE marker-expressing cells appeared to form clusters

distributed throughout the imaged area featuring a central domain of Cer1:H2B-Venus/OTX2-positive cells which extended into OTX2-single positive cells.

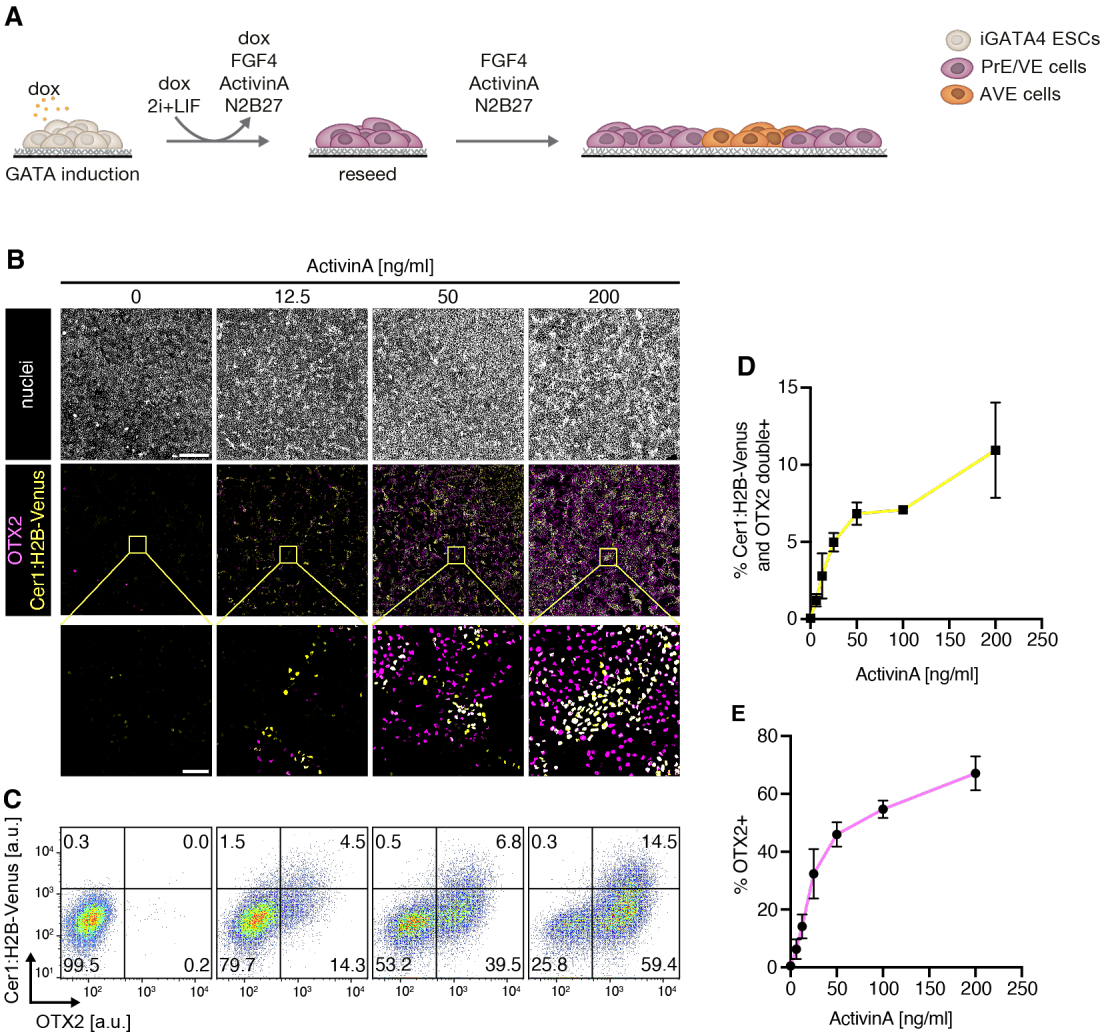

Figure 26: Nodal/Activin signals are sufficient for AVE differentiation.
A Schematic of experimental approach to generate AVE cells via activation of Nodal signaling in a 2D VE layer. **B** Immunostaining of Cer1:H2B-Venus VE cells differentiated as in A that were treated with different concentrations of ActivinA. Cells were stained for OTX2 (magenta) and H2B-Venus (yellow) to mark AVE cells. Scale bars: 500 μm; inset 50 μm. **C** Flow cytometry analysis of Cer1:H2B-Venus iGATA4 cells differentiated and stained as in B. **D** Quantification of percentage of VE that show co-expression of Cer1:H2B-Venus and OTX2 with increasing doses of ActivinA. N = 3. Error bars indicate SD. **E** Same as in D but quantified for OTX2 expressing cells.

I utilized flow cytometry to quantify the frequency of Cer1:H2B-Venus and OTX2 expression in VE cells (Figure 26C-E). The analysis revealed that the number of co-expressing cells exhibited only a modest increase with rising concentrations of ActivinA, while OTX2 expression was detected in approximately two-thirds of the cells at 200

ng/ml ActivinA indicating that the majority of cells have the ability to differentiate into AVE. However, there might be an intrinsic signal within the tissue counteracting this process. For further 2D AVE experiments, 50 ng/ml ActivinA was chosen as the standard concentration.

The observation that not all of the VE cells exhibited OTX2 expression, and within those that did, only a subset displayed Cer1:H2B-Venus expression, aligned with findings from both embryos and BELAs (Figure 27). In these systems, while the majority of VE cells overlaying the Epi cells demonstrated OTX2 expression from which a smaller number of cells exhibited CER/Cer1:H2B-Venus expression, there remained a subset in which expression of either marker was absent (green circled). It seemed that the emVE cells closer to the ExE in the embryo are the ones that do not express any AVE markers such as OTX2 or CER1, indicating a guiding role of the ExE. However, since BELAs typically include a few VE cells that also lack AVE markers, this suggests an additional intrinsic mechanism, independent of ExE cells, to restrict AVE differentiation. In summary, I can conclude that ActivinA/Nodal signals are not only necessary but also sufficient for the differentiation of spatially clustered AVE cells within a population of VE cells.

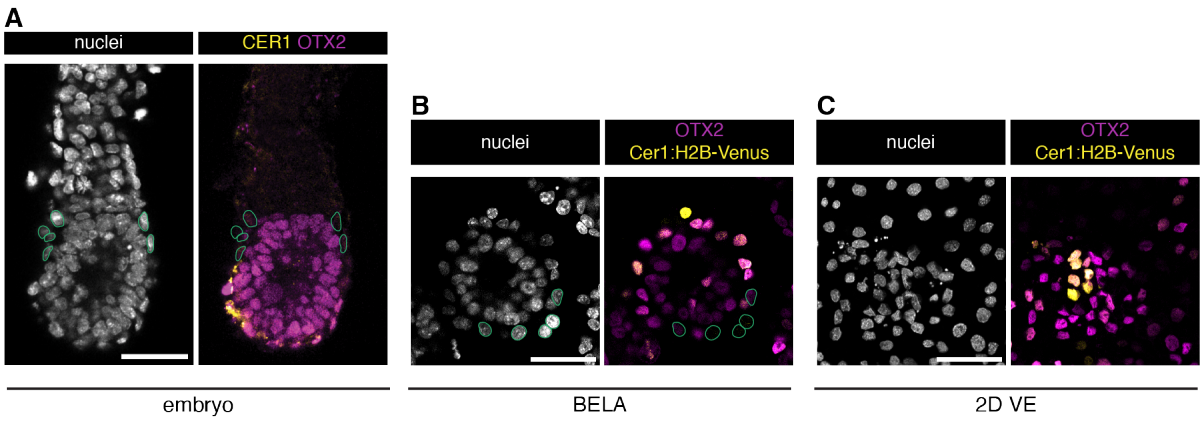

Figure 27: AVE comparison in mouse embryo, BELA and 2D VE.
A-C immunostainings of a mouse embryo (A), BELA (B) and 2D AVE (C) for the Epi and AVE marker OTX2 (magenta) and CER1/Cer1:H2B-Venus (yellow). The embryo was harvested at E5.5. BELAs were formed by an 8-hour pulse of dox in 2i+LIF with subsequent media change to N2B27 and reseeding of the cells on gelatin on the next day. BELAs were collected after three days. For a 2D AVE population, iGATA4 mouse ESCs were induced with an extended dox pulse and treated with FGF4 and 50 ng/ml ActivinA for three days. Green outlines mark nuclei of emVE cells that lack OTX2 in the embryo and BELA. Scale bars: 50 μm.

3.4.3 Nodal and Lefty1 have only minor effects in spatial restriction of AVE cells

Patterns in tissues and different cell identities can emerge from initially almost homogenous conditions in a cell autonomous manner, for example through mechanism such as the reaction-diffusion system proposed by Turing in 1952 (Turing, 1952) or Gierer and Meinhardt in 1972 (Gierer & Meinhardt, 1972). This model involves two interacting diffusible molecules, where one acts as the activator, promoting its own expression and that of its inhibitor. Notably, the inhibitor exhibits a higher diffusion rate than the activator, leading to the formation of concentration gradients (instability) and the emergence of short-range activation centers with long-range inhibition.

Nodal, along with its inhibitor Lefty, represents a reaction-diffusion pair within a Turing system, leveraging self-enhancement and long-range inhibition phenomena to break the symmetry and establish robust left-right asymmetry during embryonic development (Muller et al., 2012; Nakamura et al., 2006). Given that both Nodal and Lefty1 are expressed in the AVE cells in BELAs (Figure 28A), I sought to investigate whether they function similarly within the VE cells to generate a spatially restricted AVE. Consequently, the *Nodal* locus was mutated in the Cer1:H2B-Venus reporter cell line using the CRISPR/Cas9 system and the same guides employed for mutation in the iGATA4 cell line, resulting in a consistent deletion of 224 bp in exon 2 (Figure 25A). Both wildtype and *Nodal* mutant cells were induced into VE cells and treated with 50 ng/ml ActivinA to initiate AVE differentiation (for more details see Figure 26A). After three days, both wildtype and *Nodal* mutant cells had reached similar densities (Figure 28B), indicating that the mutation did not affect cell proliferation. Furthermore, the typical nest formation of Cer1:H2B-Venus- and OTX2-expressing AVE cells was observed. If Nodal and Lefty1 were to function within a reaction-diffusion system to break symmetry, one might anticipate reduced expression of AVE marker due to the absence of activator self-enhancement in the Nodal mutant cells. Quantification of AVE marker-expressing cells revealed that *Nodal* mutant cells exhibited decreased Cer1:H2B-Venus expression compared to wildtype cells, with frequencies decreasing from approximately 15% to 5% respectively, while OTX2 expression of OTX2 remained relatively unchanged (Figure 28C,D). This suggests that mutation in the *Nodal* locus influences the

expression of Cer1:H2B-Venus, potentially due to the absence of the Nodal positive feedback loop. However, OTX2 expression does not appear to be reliant on that self-enhancement mechanism.

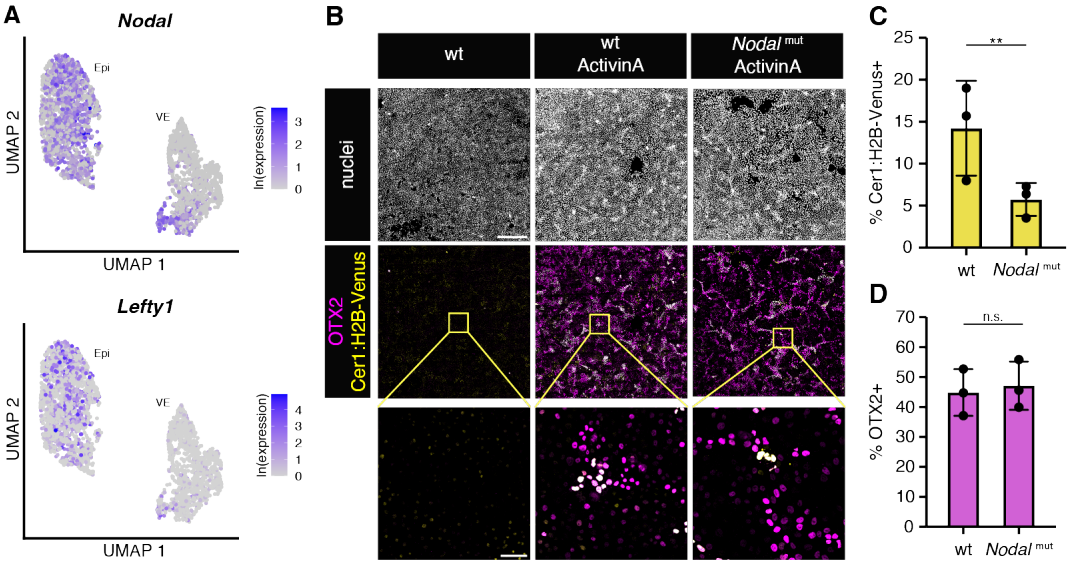

Figure 28: *Nodal* mutation in VE cells affects Cer1 reporter, but not OTX2 expression
A Ln expression levels of *Nodal* and *Lefty1* from single-cell sequencing data set, shown on same UMAP representation as in Figure 18B. **B** Immunostaining of induced wildtype and *Nodal* mutant VE cells treated with 50 ng/ml for AVE differentiation. Wildtype cells without ActivinA treatment served as control. Cells were stained for OTX2 (magenta) and H2B-Venus (yellow) to mark AVE cells. Scale bars: 500 μm; inset 50 μm. **C,D** Quantification via flow cytometry conducted on cells differentiated as described in B to determine the percentage of VE cells expressing Cer1:H2B-Venus (C) and OTX2 (D). N=3. Error bars indicate SD.

To investigate whether Lefty1 functions as the inhibitor in a potential reaction-diffusion system with Nodal, a mutation was induced in the *Lefty1* locus of the Cer1:H2B-Venus reporter cell line using two CRISPR guides to excise the ATG in the first exon (Figure 29A). Two independent clones were used in the subsequent experiment, both carrying substantial deletions in the first exon, measuring 113 bp and 117 bp, respectively. Wildtype cells and the two *Lefty1* mutant clones were induced into VE using an extended dox pulse and FGF4, while concurrently treated with 50 ng/ml ActivinA to initiate AVE differentiation. The anticipated outcome was a higher number of AVE cells in the *Lefty1* mutant condition due to the presence of the activator ActivinA and a functional positive feedback loop with Nodal, without the coupling with the inhibitor Lefty1 to restrain AVE differentiation. The number of Cer1:H2B-Venus expressing cells was

assessed via flow cytometry, revealing that the first clone had a slightly higher mean of Cer1:H2B-Venus expressing cells compared to the control, measuring 8% and 14% respectively, although the difference was not statistically significant. Unexpectedly, the second clone displayed a decrease in the number of Cer1:H2B-Venus expressing cells to only approximately 3%, indicating that neither clone fulfilled the expectation of an increase in AVE marker expressing cells.

The positive Nodal feedback loop appears to play a role in the number of Cer1:H2B-Venus-expressing cells, while the impact of the *Lefty1* mutation may be minimal due to redundancy with other expressed Nodal inhibitors as CER1. Taken together, these results argue against an important role of a Nodal/Lefty activator-inhibitor system in cellular symmetry breaking and patterning during AVE differentiation.

Figure 29: *Lefty1* mutation does not lead to increased AVE induction.
A Schematic illustrating the *Lefty1* locus mutation present in the Cer1:H2B-Venus reporter cell line, identified through Sanger sequencing of PCR amplicon specifically designed to encompass the *Lefty* first exon. **B** Quantification via flow cytometry for Cer1:H2B-Venus expression. wt and *Lefty* mutant cells were induced into VE and treated with 50 ng/ml to differentiate into AVE. N=3. n.s. indicates $p > 0.05$, determined by an ordinary one-way Anova with Bonferroni's multiple testing correction.

3.5 A new counteracting signal for AVE differentiation

3.5.1 BMP4 exhibits only mild effects on AVE differentiation

In the embryo, BMP4 secreted from the ExE is described as the opposing signal for AVE differentiation that positions the AVE to the distal tip of the egg cylinder (Yamamoto et al., 2009). To test the effect of BMP4 on AVE differentiation and whether BMP4 acts as a tissue-intrinsic AVE restriction signal in my 2D AVE model, the Cer1:H2B-Venus reporter cells were induced into VE cells with an extended dox pulse

and FGF4, and treated with 50 ng/ml ActivinA together with 50 ng/ml BMP4 or 100 nM LDN193189 (LDN; BMP receptor inhibitor) during AVE differentiation (Figure 30A). The addition of these molecules had no noticeable effect on cell viability, nor did it significantly alter the expression of the AVE marker, as assessed by fluorescent microscopy examination.

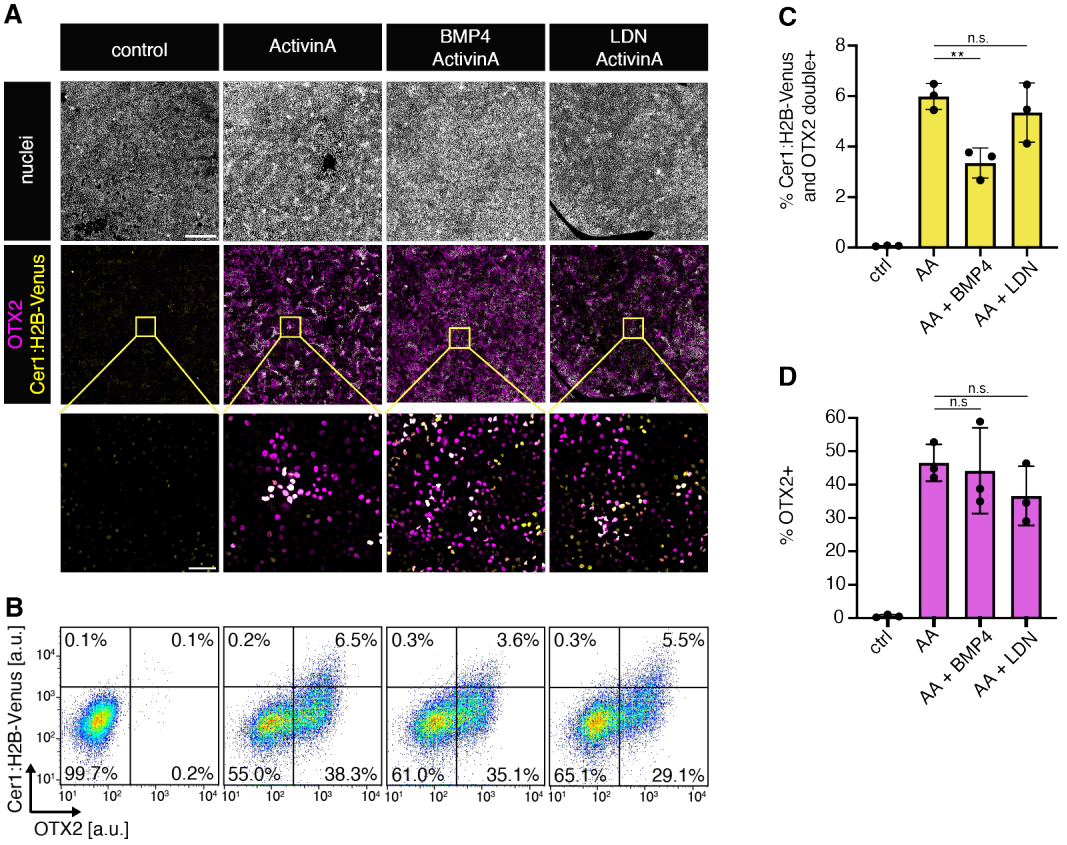

Figure 30: No evidence for BMPs tissue intrinsic restriction of AVE differentiation.
A Immunostaining of Cer1: H2B-Venus VE cells for the AVE markers OTX2 (magenta) and H2B-Venus (yellow). Cells were treated with 50 ng/ml ActivinA together with 50 ng/ml BMP4 or 100 nM LDN193189 (BMP inhibitor). Scale bars 500 μm; inset 50 μm. **B** Flow cytometry analysis of Cer1:H2B-Venus iGATA4 cells differentiated and stained as in A. **C** Quantification of VE cell percentage that co-expresses Cer1:H2B-Venus and OTX2. Cells were differentiated as in A. N = 3. Error bars indicate SD. ** indicates $p \leq 0.005$ respectively and n.s. indicates $p > 0.05$, determined by an ordinary one-way Anova with Bonferroni's multiple testing correction. **D** Same as in C but quantified for OTX2 expressing cells.

Flow cytometry quantification of the AVE marker Cer1:H2B-Venus and OTX2 revealed only marginal changes in expression for the different conditions (Figure 30B-D). The addition of BMP4 led to a slight decrease in the frequency of Cer1:H2B-Venus/OTX2-double positives from approximately 6% to 3%, with no observable effect on the OTX2-

positive cells. However, LDN did not influence the expression of either marker suggesting that there is no tissue intrinsic BMP signaling that could explain the spatial restriction in AVE differentiation. While these results do not rule out BMP4 as a potential restricting signal in the embryo, its influence on restricting AVE differentiation in vitro is limited. This is evident from its minor impact on Cer1:H2B-Venus expression and the lack of response to LDN, suggesting that tissue-intrinsic BMP may not play a significant role.

3.5.2 Tissue-intrinsic Wnt/β-catenin signals counteract AVE differentiation

Looking for another candidate for the tissue-intrinsic antagonizing signal, I decided to prioritize Wnt signaling as the Wnt antagonist *Sfrp1* was the most strongly upregulated gene in AVE cells compared to emVE cells (Figure 20B). Another incentive to investigate Wnt signaling came from TCF:H2B-GFP reporter embryos designed to visualize canonical Wnt activity in cells. These embryos displayed heterogenous reporter activity across the entire VE cells (Figure 31).

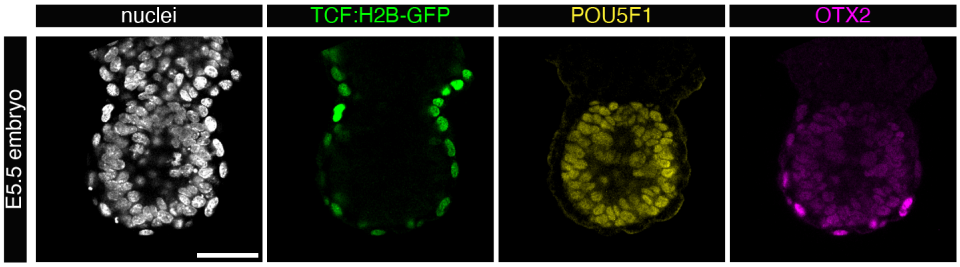

Figure 31: Mouse embryo with TCF/Lef:H2B-GFP reporter expression in the VE.
Immunostaining of an E5.5 embryo for the Wnt/β-catenin reporter TCF/Lef:H2B-GFP (green), the Epi marker POU5F1 (yellow) and the Epi/AVE marker OTX2 (magenta). Scale bar: 50 μm.

I applied a similar experimental approach to that used to investigate BMP4 signaling in AVE differentiation. The dox-induced Cer1:H2B-Venus cells were treated with FGF4 and 50 ng/ml ActivinA in combination with either Wnt/β-catenin agonist Chir99021 (Chiron, Chi) or Wnt/β-catenin antagonists XAV939 (XAV) or IWP2 for AVE differentiation. In contrast to the previous experiment, fluorescent microscopy examination already showed quite clearly that addition of Chiron led to an extensive reduction of

Cer1:H2B-Venus and OTX2 expressing cells, while addition of XAV did exactly the opposite (Figure 32A). There were only mild potential effects of IWP2 on AVE marker expression. Quantification via flow cytometry corroborated the previous findings (Figure 32B-D). Activation of the Wnt signaling pathway with Chiron completely abrogated the expression of Cer1:H2B-Venus and OTX2, while treatment with XAV led to an increase of Cer1:H2B-Venus and OTX2-double positive cells from approximately 8% to 35% and an increase of OTX2-positive cells from approximately 40% to 80%. Inactivation of the Wnt signaling pathway using the Wnt antagonist IWP2 showed only mild effects and mainly on OTX2 expression.

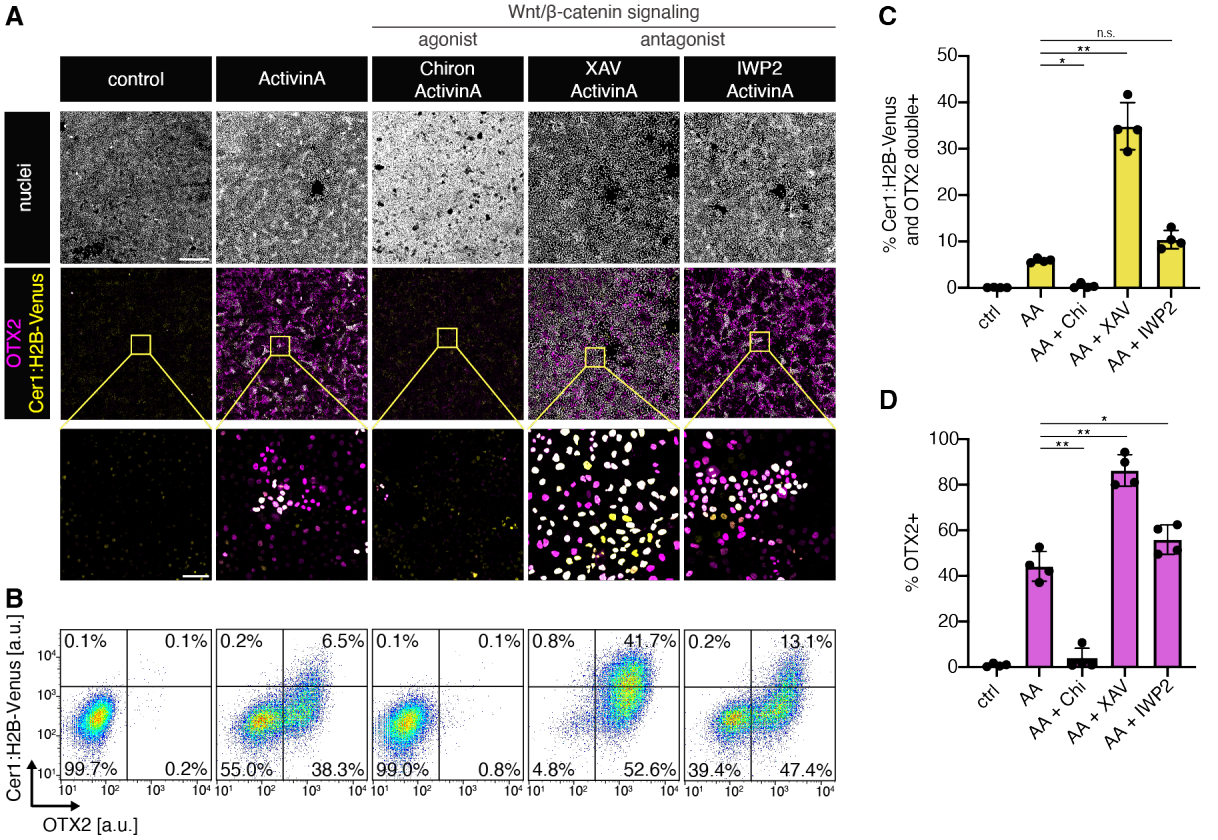

Figure 32: Tissue intrinsic Wnt/β-catenin signaling counteracts AVE differentiation.
A Immunostaining of Cer1:H2B-Venus VE cells for the AVE markers OTX2 (magenta) and H2B-Venus (yellow). Cells were treated with 50 ng/ml ActivinA together with 3 μM Chir99021 (Chiron), 20 μM XAV939 or, or 2 μM IWP2. Scale bars 500 μm; inset 50 μm. **B** Flow cytometry analysis of Cer1:H2B-Venus iGATA4 cells differentiated and stained as in A. **C** Quantification of VE cell percentage co-expressing Cer1:H2B-Venus and OTX2. Cells were differentiated as in A. N = 3. Error bars indicate SD. * and ** indicate $p \leq 0.05$ and $p \leq 0.005$ respectively, n.s. indicates $p > 0.05$, determined by an ordinary one-way Anova with Bonferroni's multiple testing correction. **D** Same as in C but quantified for OTX2 expressing cells.

The discrepancy in outcomes between the two Wnt pathway inhibitors, XAV and IWP2, may be due to their different targets. While XAV inhibits tankyrase 1 and 2 and therefore improves the degradation of β-catenin, IWP2 inhibits the acyltransferase Porcupine, which is necessary for Wnt ligand secretion (Huang et al., 2009; Willert et al., 2003). Collectively, these results suggest that Nodal-driven AVE differentiation is antagonized by tissue intrinsic β-catenin signals, whose localized inhibition may lead to the formation of spatially restricted AVE nests.

To ensure that the impact of Chiron, XAV, or IWP2 on AVE differentiation did not originate from their interference with the differentiation of GATA6-expressing VE cells, I examined the expression of GATA6 in the presumed VE cells (Figure 33).

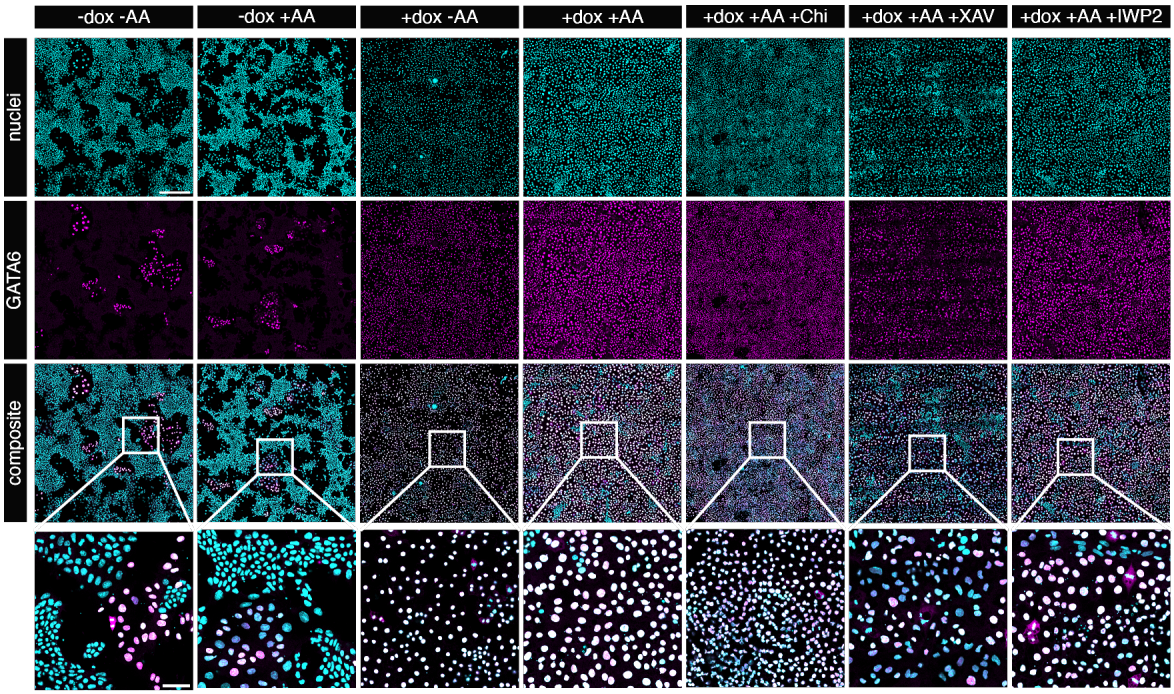

Figure 33: GATA6 expression is independent of ActivinA and Wnt/β-catenin signaling.
Immunostaining of iGATA4 cells cultured for three days in the indicated media conditions without (first two conditions) or with prior dox induction (remaining five conditions) for the VE marker GATA6 (magenta). Cells were treated under various combinations in N2B27, including 50 ng/ml ActivinA with 3 μM Chir99021 (Chiron), 20 μM XAV939 or, or 2 μM IWP2. GATA6 positive cells could also be found without any dox pulse and are likely due to leaky transgene expression and spontaneous differentiation in N2B27. Scale bars 200 μm; inset 50 μm.

Non-induced cells served as a control to evaluate whether the addition of ActivinA alone could stimulate VE differentiation. iGATA4 cells underwent treatment according

to the standard AVE differentiation protocol, with the specific conditions outlined in the figure. Even in conditions where cells were not induced with a dox pulse, isolated spots with GATA6-positive cells appeared, likely due to leaky transgene expression or spontaneous differentiation in N2B27. Nonetheless, homogenous GATA6 expression was observed in all conditions where cells experienced a doxycycline pulse, regardless of subsequent treatment with ActivinA or the Wnt/β-catenin pathway modulators. This result indicates that treatment with Chiron, XAV or IWP2 does not interfere with proper VE differentiation.

3.5.3 Cell density can influence AVE differentiation

Once I confirmed that these cells indeed transitioned from VE into AVE, I looked into a potential effect of cell density on AVE differentiation. Interestingly, VE cells that were treated with XAV predominantly underwent differentiation into AVE cells, but they seemed to exhibit lower cell density within the tissue culture vessel (Figure 32A). To assess whether XAV exerted an independent effect or if reduced density alone could promote AVE differentiation, I manipulated the cell number during reseeding of the induced cells with ActivinA or together with XAV (Figure 34A,B). The cells were titrated down from 50.000 cells to 6.250 cells per cm^2. When fewer VE cells were reseeded and treated with ActivinA alone, there seemed to be an uptick in the number of OTX2 and Cer1:H2B-Venus expressing cells, whereas a higher cell number correlated with reduced AVE marker expression. VE cells treated with additional XAV showed similar trends: a lower cell number did not notably impact the already high number of AVE cells, but a higher count resulted in a diminished AVE differentiation. To capture not only the frequency of AVE marker expression in the cells but also their density, I switched from flow cytometry to a computational approach using the fluorescent images. Cells were segmented based on their nuclear stain signal, and fluorescent intensity was measured (Figure 34C). The average local density was measured as the inverse of the squared distance to the five nearest neighbors of a cells (Figure 34D). Quantification unveiled that the cells treated with ActivinA exhibited the highest proportions of AVE marker expression, roughly 70% OTX2 and 30% Cer1:H2B-Venus,

when only 6.250 cells were reseeded. The AVE marker expression decreased with higher reseeded cell numbers to approximately 25% OTX2 and 10% Cer1:H2B-Venus.

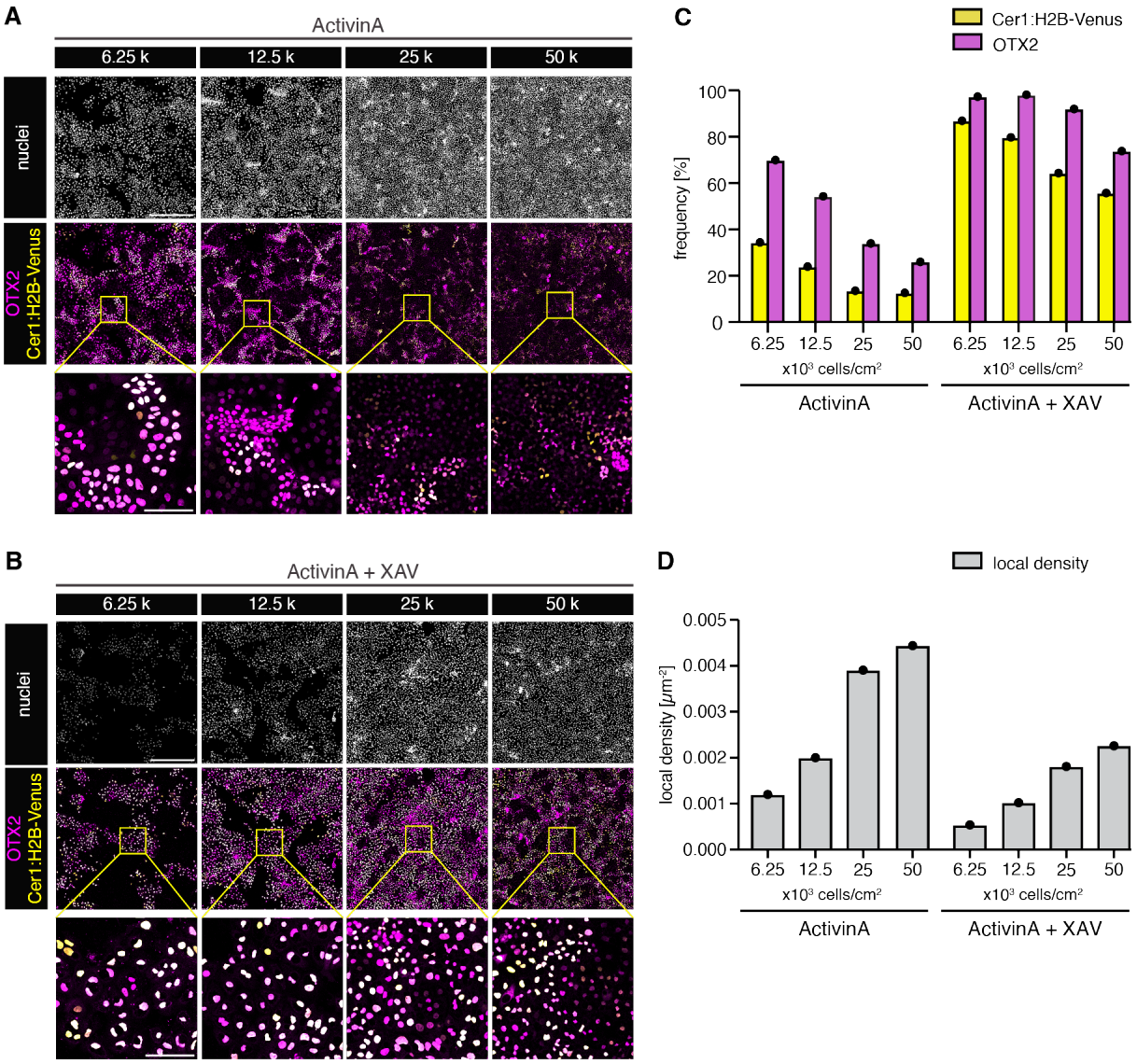

Figure 34: Cell density influences AVE differentiation.
A,B Immunostaining of differentiated Cer1:H2B-Venus VE cells for the AVE markers OTX2 (magenta) and H2B-Venus (yellow). Different numbers of cells were used at the time point of reseeding in the AVE differentiation protocol to generate different densities (cell counts per cm2). Cells were either treated with 50 ng/ml ActivinA alone (A) or together with 20 μM XAV. Scale bars: 500 μm; inset 100 μm. **C** Quantification of VE cell frequency expressing Cer1:H2B-Venus or OTX2 via segmentation and fluorescence measurement of the images in A and B. **D** Local density measured as inverse of squared mean distance to the 5 nearest neighbors.

When VE cells were additional treated with XAV alongside ActivinA at the lowest seeded cell number, over 90% OTX2 and over 80% Cer1:H2B-Venus expressing cells

were observed. There was only a slight decrease to more than 70% OTX2 expressing cells and more than 50% Cer1:H2B-Venus expressing cells when a very high cell number was seeded. Analysis of the average local density values revealed that, indeed, even when the same cell number was seeded, XAV treated cells consistently exhibited lower local density after three days of culture, suggesting that XAV affects cell proliferation. Reseeding 50.000 cells for the XAV condition matched the local density of ActivinA-only treated cells when only 12.500 cells were reseeded, indicating that although both conditions had the same density, XAV resulted in significantly higher cell number in AVE marker expressing cells. Together, this demonstrates that cell density plays a role in AVE differentiation but also reveals an additional effect of XAV independent of density.

3.6 β-catenin acts independently of Wnt ligands

3.6.1 Mutation of single Wnt ligands does not affect AVE differentiation

The previous findings suggest that β-catenin activity plays an important role in AVE differentiation (Figure 32). This activity can be controlled by Wnt ligands in the Wnt/β-catenin signaling pathway or by mechanical forces at the cell adherens junctions (Figure 4). To elucidate the role of Wnt signaling, I examined the expression of all Wnt ligands in the scRNA data set (Figure 35). Among all Wnt ligands, only *Wnt4* and *Wnt11* exhibited reasonable expression profiles in the VE compartment of BELAs (Figure 35). To investigate whether loss of Wnt4 or Wnt11 could replicate the observed phenotype induced by XAV treatment, I genetically mutated the *Wnt4* and *Wnt11* loci in the Cer1:H2B-Venus reporter cell line using two CRISPR guides for each locus to excise a more than 100 bp large fragment (Figure 36A,B). Two clones were selected with a mutation in the *Wnt4* locus. One harboring a mutation of 115 bp, the other one only showing two small deletions sited around the two cutting sides of 7 bp and 15 bp (Figure 36A). Both clones carrying a mutation in the *Wnt11* locus had the same mutation of 160 bp (Figure 36B).

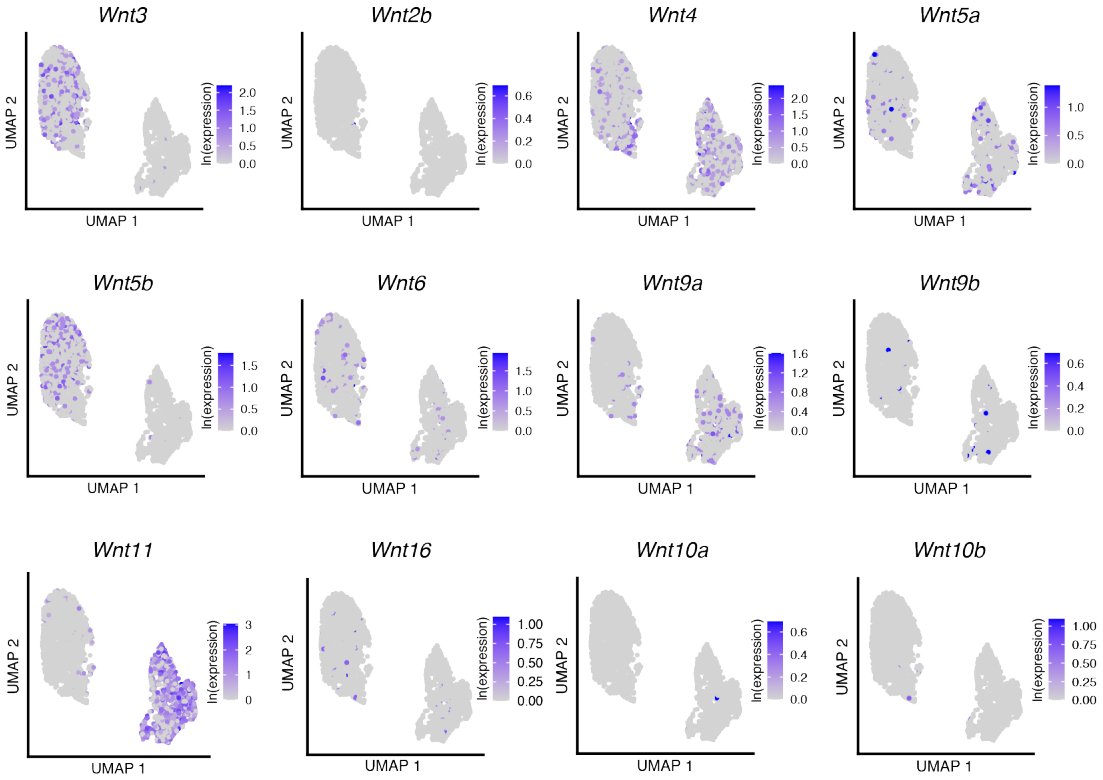

Figure 35: Expression of Wnt ligands in BELAs.
Ln expression levels of Wnt ligands, shown on same UMAP representation as in Figure 18B. Epi cells can be found in the left cluster and VE cells can be found in the right cluster. Wnt1, Wnt2, Wnt3a, Wnt7a, Wnt7b, Wnt8a and Wnt8b are not expressed and therefore not shown in a UMAP plot here.

Wildtype, *Wnt4* mutant, and *Wnt11* mutant cells were induced with an extended doxycycline pulse together with FGF4, and treated with 50 ng/ml ActivinA for AVE differentiation. Additionally, wildtype cells were treated with 20 μM XAV serving as another control for the *Wnt* mutants. Fluorescent microscopy examination indicated no change in expression of the AVE marker Cer1:H2B-Venus and OTX2 between wildtype and Wnt mutants (Figure 36B). Quantification via flow cytometry for expression of the Cer1:H2B-Venus reporter implied no significant differences between wildtype and *Wnt11* or *Wnt4* mutant cells (Figure 36C). Based on these findings, it is unlikely that Wnt4 or Wnt11 are the active Wnt ligands that control β-catenin in counteracting AVE differentiation.

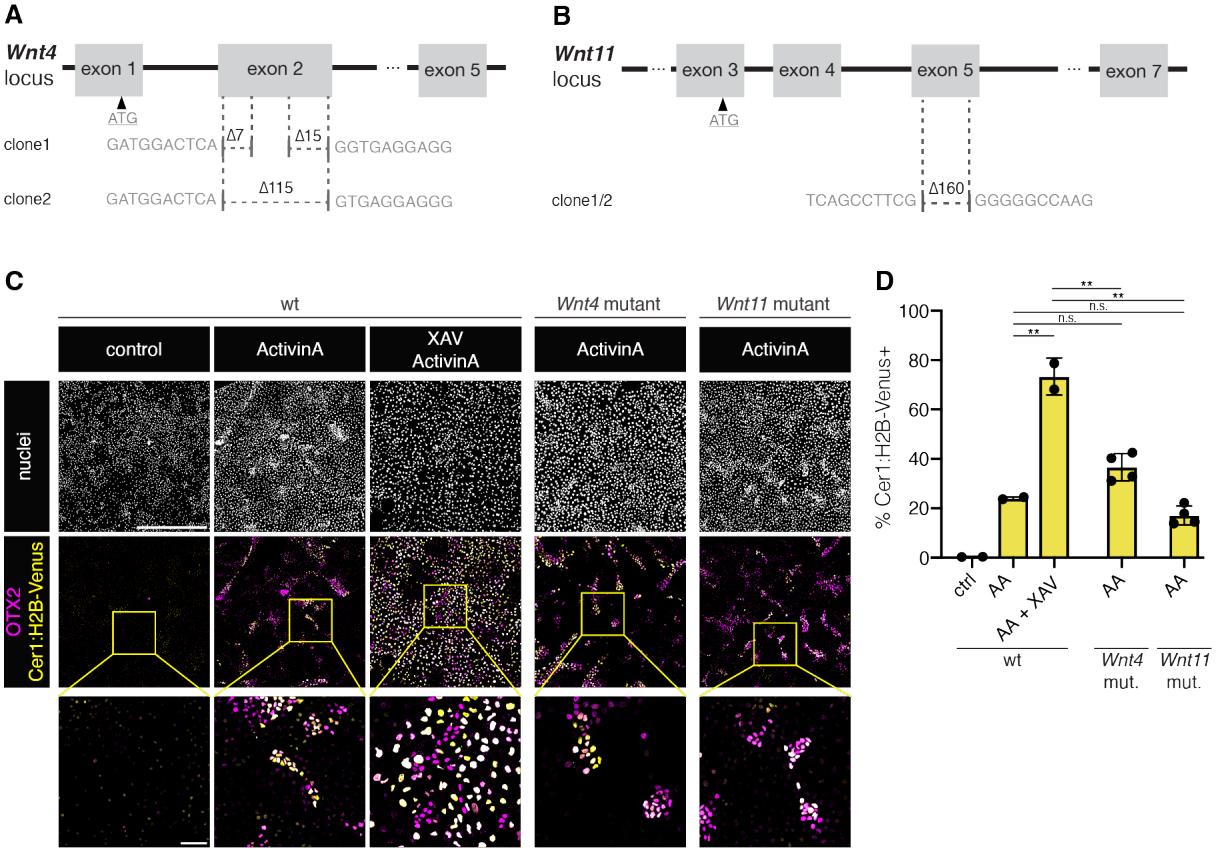

Figure 36: Mutation of *Wnt4* and *Wnt11* cannot recapitulate the phenotype of XAV.
A,B Schematics illustrating the *Wnt4* (A) and *Wnt11* (B) loci mutations present in the Cer1:H2B-Venus reporter cell line, identified through Sanger sequencing of PCR amplicon specifically designed to encompass the *Wnt4* second exon and *Wnt11* fifth exon. **C** Immunostaining of Ce1:H2B-Venus VE wildtype, as well as *Wnt4* and *Wnt11* mutant cells for the AVE markers OTX2 (magenta) and H2B-Venus (yellow). Cells were treated with 5 ng/ml ActivinA together with 20 μM XAV939. Scale bars 500 μm; inset 50 μm. **D** Quantification of VE cell percentage expressing Cer1:H2B-Venus via flow cytometry. Cells were differentiated as in B. N = 2. Two clones were pooled for both *Wnt4* mutant and *Wnt11* mutant condition. For exact mutation see A,B. Error bars indicate SD. ** indicate $p \leq 0.005$ and n.s. indicates $p > 0.05$, determined by multiple comparison one-way Anova with multiple testing correction.

3.6.2 Abrogating Wnt ligand secretion does not affect AVE differentiation

The sequencing of BELAs was conducted at the endpoint, a stage at which the AVE has already formed. It is possible that the Wnt ligands responsible for restricting AVE differentiation exert their influence earlier in development, potentially resulting in reduced expression levels by the time of sequencing. To address this possibility, I introduced mutations in the genetic locus of *Porcn* in the Cer1:H2B-Venus reporter cell line (Figure 37A). Porcn, a membrane bound acyltransferase, plays a critical role for

activation and secretion of Wnt ligands. Consequently, mutating *Porcn* is expected to abolish all Wnt signaling (Proffitt & Virshup, 2012; Willert et al., 2003). Two CRISPR guides were designed to excise a large fragment out of exon 8. However, the second guide appeared ineffective, resulting in only small deletions at the first cutting site. Among the clones generated, one exhibited a 2 bp deletion, with the expectation of inducing a frame shift mutation (Figure 37A). To validate the *Porcn* mutation in the cells, their phenotype was assessed in an orthogonal assay to AVE differentiation (Tsakiridis et al., 2014) (Figure 37B).

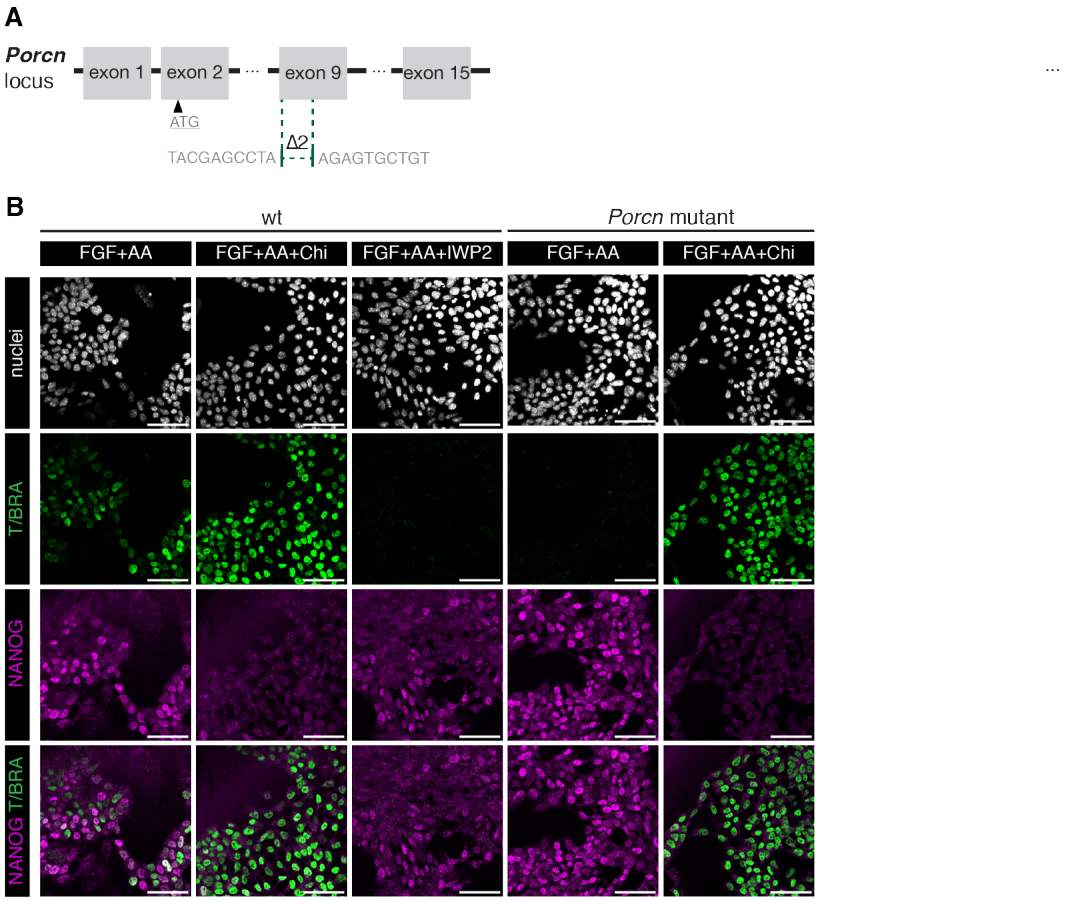

Figure 37: Validation of *Porcn* mutation phenotype.
A Schematic illustrating the *Porcn* locus mutation present in the Cer1:H2B-Venus reporter cell line, identified through Sanger sequencing of PCR amplicon specifically designed to encompass the ninth exon of *Porcn*. **B** Differentiation approach to determine phenotype of the mutation in the *Porcn* locus. Cells were cultured for several passages in N2B27 supplemented with FGF2 and ActivinA to induce Wnt mediated T/Bra expression. The Porcn inhibitor IWP2 was included here to check the activity and to compare to the *Porcn* mutant cell line. As control for T/Bra expression Chiron was added to circumvent the need of secreted Wnt ligands. Scale bars: 50 μm.

The cells were cultured in N2B27 supplemented with FGF2 and ActivinA for several passages, conditions expected to trigger Wnt mediated T/Brachyury (T/BRA) expression. Consistent with expectations for a *Porcn* mutation and Porcn inhibition (IWP2), the mutated cells did not exhibit any T/BRA expression. This phonotype could be rescued when Chiron was added, bypassing the need for secreted Wnt ligands to trigger T/BRA expression (Figure 37B).

As in the experiment for the *Wnt* mutants, the *Porcn* mutant cells as well as wildtype cells were induced with an extended dox pulse together with FGF4 and treated with 50 ng/ml ActivinA or together with XAV to trigger AVE differentiation (Figure 38A).

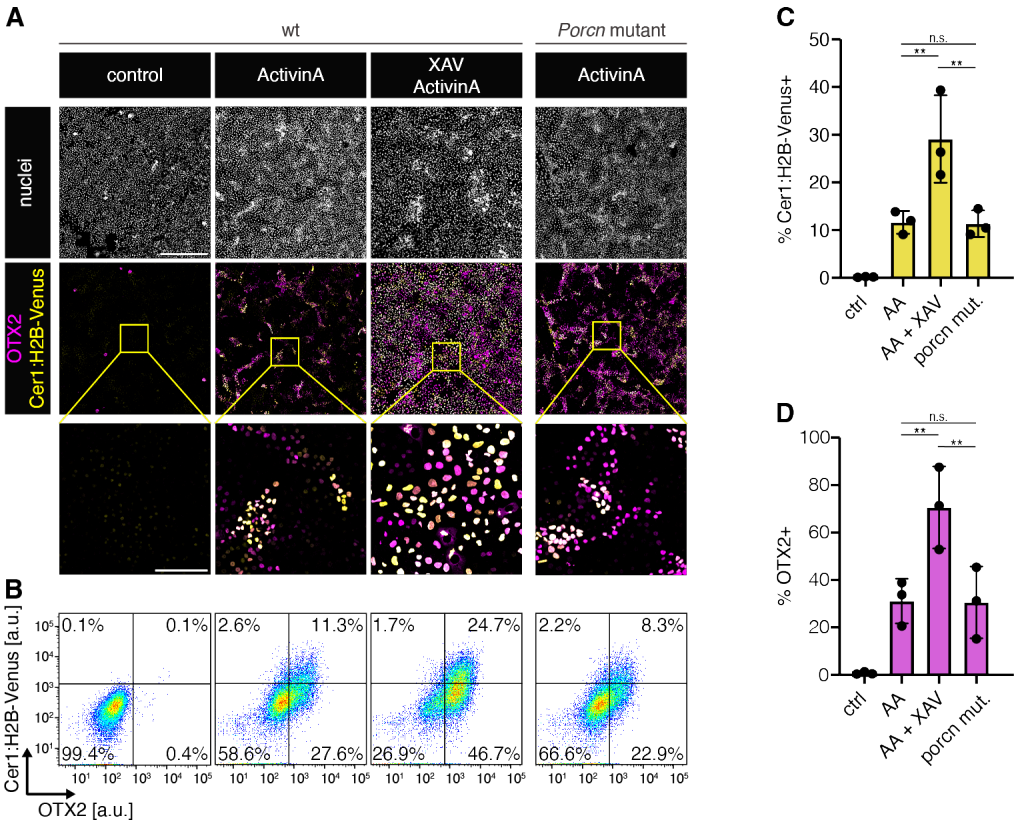

Figure 38: Mutation of *Porcn* indicates Wnt ligand independent β-catenin signaling.
A Immunostaining of Cer1:H2B-Venus VE wildtype and *Porcn* mutant cells for the AVE markers OTX2 (magenta) and H2B-Venus (yellow). Cells were treated with 50 ng/ml ActivinA together with 20 μM XAV939. Scale bars: 500 μm; inset 100 μm. **B** Flow cytometry analysis of Cer1:H2B-Venus iGATA4 cells differentiated and stained as in A. **C** Quantification of VE cell percentage expressing Cer1:H2B-Venus. Cells were differentiated as in A. N = 3. Error bars indicate SD. ** indicates $p \leq 0.005$ and n.s. indicates $p > 0.05$, determined by an ordinary one-way Anova with Bonferroni's multiple testing correction. **D** Same as in C but quantified for OTX2 expressing cells.

Examination of the fluorescent microscopy images indicated no visible difference in the expression of the AVE marker Cer1:H2B-Venus and OTX2 in the *Porcn* mutant cells compared to the wildtype cells. Quantification via flow cytometry confirmed this: there was no significant difference between wildtype and *Porcn* mutant cells in the number of Cer1:H2B-Venus-positve cells nor in OTX2-positive cells (Figure 38B-D). Therefore, the results indicate that β-catenin activity in the VE is not driven by Wnt signaling but rather regulated by other factors.

3.7 Effects of mechanical perturbations on AVE differentiation

Because previous results in manipulating Wnt/β-catenin signaling indicated that β-catenin activity functions independently of Wnt ligands, I will focus on the possibility that β-catenin in adherens junctions is regulated by mechanical forces.

3.7.1 E-cadherin is upregulated in cell junctions upon ActivinA treatment

To explore cell adherens junctions, particularly the localization of E-cadherin (CDH1), and assess potential differences between Cer:H2B-Venus-negative and -positive cells, I performed an immunostaining for E-cadherin on iGATA4 cells induced with an extended dox pulse together with FGF4 and treated with 50 ng/ml ActivinA (Figure 39A). As a control, differentiated VE cell without any ActivinA treatment were used. As expected, the controll cells showed no Cer1:H2B-Venus expression and exhibited just low expression of E-cadherin in the membrane (Figure 39A,B). Conversely, cells that were treated with ActivinA expressed Cer1:H2B-Venus in the typical nests, accompanied by higher expression of E-cadherin in the membrane of those cells corresponding to a higher local density of Cer1:H2B-Venus+ cell (Figure 39C). This suggests that strengthened cell-cell contacts via adhesive junctions are established only after treatment with ActivinA. I conclude, that ActivinA-induced AVE differentiation promotes an

epithelial phenotype in the H2B-Venus-positive cells characterized by enhanced cell adhesion compared to the surrounding H2B-Venus-negative cells.

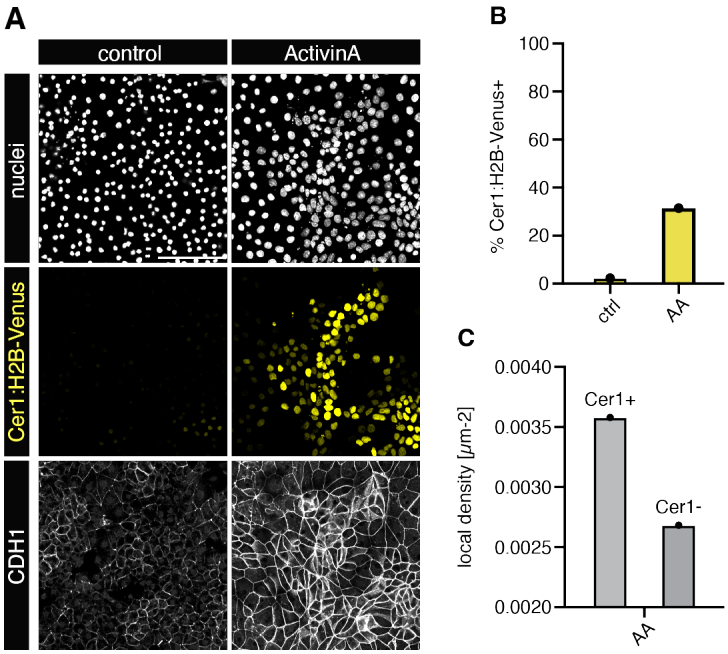

Figure 39: Cells in AVE nests seem to have stronger cell-cell adhesion.
A Representative cutout of a broader field of view. Immunostaining of Cer1:H2B-Venus VE cells for H2B-Venus (yellow) and CDH1 (E-cadherin; gray). Cells were treated with 50 ng/ml ActivinA to induce AVE differentiation. Scale bar: 100 μm. **B** Quantification of VE cell frequency expressing Cer1:H2B-Venus via segmentation and fluorescence measurement of the entire field of view. **C** Local density of the Cer1:H2B-Venus- (Cer1-) and Cer1:H2B-Venus+ (Cer1+) cells measured as inverse of squared mean distance to the 5 nearest neighbors.

3.7.2 Blocking of E-cadherin binding sites promotes AVE differentiation

In my in vitro differentiation system, AVE cells showed enhanced cell-cell adhesion, as evidenced by increased expression of E-cadherin in the membrane. E-cadherin serves as the core transmembrane protein in adherens junctions facilitating the connection between adjacent cells. β-catenin, together with other catenins, mediates the linkage between E-cadherin and the actin cytoskeleton through a catch-bond mechanism (Buckley et al., 2014). Disruption of adherens junctions via treatment with an E-cadherin blocking antibody (DECMA) is expected to release β-catenin from the adherens junctions (Figure 40A). I will therefore investigate the influence of cell-cell adhesion disruption on AVE differentiation.

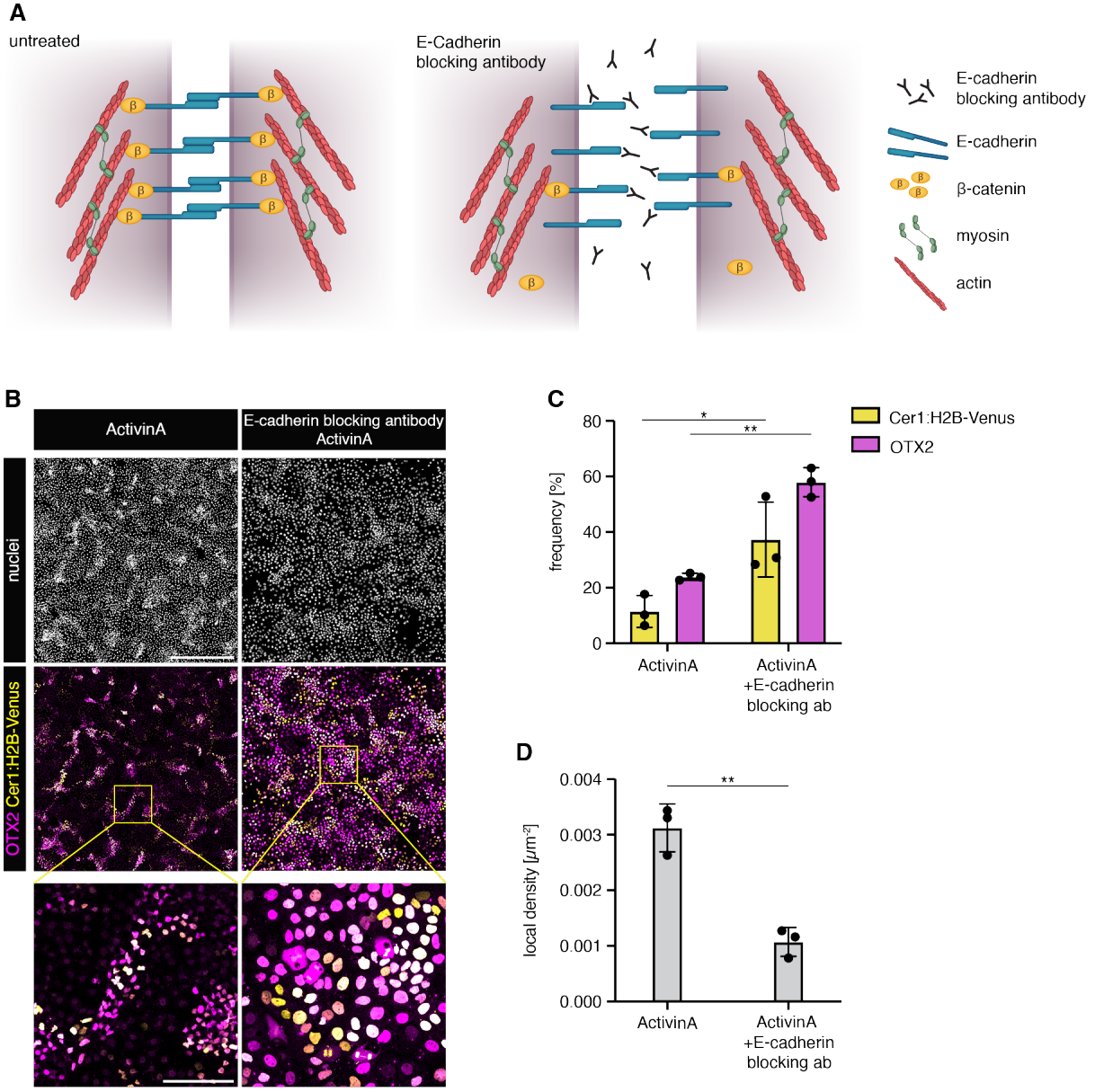

Figure 40: E-cadherin blocking antibody increases number of AVE cells.
A Schematic of simplified adherens junctions manipulated by E-cadherin blocking antibodies**. B** Immunostaining of Cer1:H2B-Venus VE cells for the AVE marker OTX2 (magenta) and H2B-Venus (yellow). Cells were treated with 50 ng/ml ActivinA or together with 10 μg/ml E-cadherin blocking antibody DECMA. Scale bar: 500 μm; inset 100 μm. **C** Quantification of VE cell frequency expressing Cer1:H2B-Venus or OTX2 via segmentation and fluorescence measurement of the images. N = 3. Error bars indicate SD. * and ** indicate $p \leq 0.05$ and $p \leq 0.005$ respectively, determined by a two-tailed, unpaired t-test. **D** Local density of the cells, measured as the mean distance to the 5 nearest neighbors and plotted as the inverse of the area. ** indicates $p \leq 0.005$, determined by a two-tailed two-tailed, unpaired t-test.

Following induction with an extended dox pulse along with FGF4, cells were treated with ActivinA and reseeded in the presence of 10 μg/ml E-cadherin blocking antibody during AVE differentiation for three days. This antibody binds to the outer domain of E-

cadherins, obstructing their ability to bind to other E-cadherins. Notably, immunostaining for the AVE markers Cer1:H2B-Venus, and OTX2, revealed increased expression levels in cells treated with the E-cadherin blocking antibody of both markers when cells were treated with E-cadherin blocking antibody (Figure 40B). Unlike the usual quantification method, which involves examining large numbers of stained cells using flow cytometry, the DECMA treatment at a high concentration allowed only for a limited volume of medium and therefore small tissue culture vessels. Consequently, these cells were quantified computationally using segmented fluorescent measurement (Figure 40C). Both the expression of Cer1:H2B-Venus and OTX2 increased significantly, rising from approximately 10% to nearly 40% and from approximately 20% to almost 60% respectively, but the density decreased to a third accounting probably partly for the high rate of AVE cells. This finding suggests that mechanical perturbation, achieved by disrupting cell-cell adhesion with E-cadherin blocking antibodies, may promote AVE differentiation. Disruption of cell-cell adhesion might have let to the release of β-catenin from the adherens junctions, therefore impairing the cells' ability to sense and react to force.

3.7.3 Lowering cell contractility promotes AVE differentiation

To confirm the findings obtained with the E-cadherin blocking antibody treatment, indicating that a reduced cell-cell adhesion promotes AVE differentiation, I used a similar strategy by applying Blebbistatin (Figure 41A). Blebbistatin is a small molecule inhibitor for non-muscle myosin II ATPase that impedes cell contractility upon tension from cell-cell interactions (Kovács et al., 2004). Therefore, β-catenin should be released from the adherens junctions as predicted from the catch-bond mechanism.

Cer1:H2B-Venus cells were induced with an extended dox pulse together with FGF4 and treated with 50 ng/ml ActivinA together with various concentrations of Blebbistatin during AVE differentiation. To evaluate Blebbistatin's impact on AVE differentiation and its potential to mimic effects of XAV, induced cells were treated with 50 ng/ml ActivinA alone or in combination with 20 μM XAV, serving as controls (Figure 41B). Treating the induced cells with ActivinA alone resulted in the formation of typical AVE nests

characterized by an inner core of Cer1:H2B-Venus- and OTX2-expressing cells, extending into a domain of OTX2-single positive cells. Addition of XAV led the majority of cells convert into an AVE state (Figure 41B). Combining a titration series of Blebbistatin with ActivinA increased the number of AVE-converting cells similar to XAV but also induced potential failure in proliferation at high concentrations of Blebbistatin (Figure 41C). Computational quantification of cells expressing AVE markers was necessary due to the low cell numbers in the high Blebbistatin conditions (Figure 41D). This analysis enabled measurement of local densities to determine if they played a role in AVE differentiation (Figure 41E). Computational analysis of fluorescent intensities for the AVE markers, along with local cell densities, revealed that higher concentrations of Blebbistatin correlated with an increase in the number of AVE marker-expressing cells but also with a decrease in their local density.

This raised the question of whether Blebbistatin independently influenced AVE differentiation or if the observed effects were due to a lower cell density prompting more cells to convert into an AVE state. Comparison with the control group, that was treated with ActivinA alone, showed a similar local density when 6.25 μM Blebbistatin was added (Figure 41E, dotted line). However, cells treated with Blebbistatin exhibited a higher frequency of AVE marker expressing cells, with approximately 70% expressing OTX2 and 40% expressing Cer1:H2B-Venus, compared to the ActivinA control, which showed a frequency of only 30% OTX2 and 10% Cer1:H2B-Venus (Figure 41D, dotted line).

Taken together, the findings indicate that Blebbistatin treatment, aimed at reducing cell contractility, promotes differentiation into AVE cells, mirroring the effect seen with XAV. A reduction in cell contractility is supposed to release β-catenin from the adheres junction as proposed by the catch-bond mechanism and therefore might result in β-catenin degradation. Mechanical perturbations, by downregulation of cell-cell adhesion and contractility caused by treatment with an E-cadherin blocking antibody and Blebbistatin, therefore seems to promote AVE differentiation.

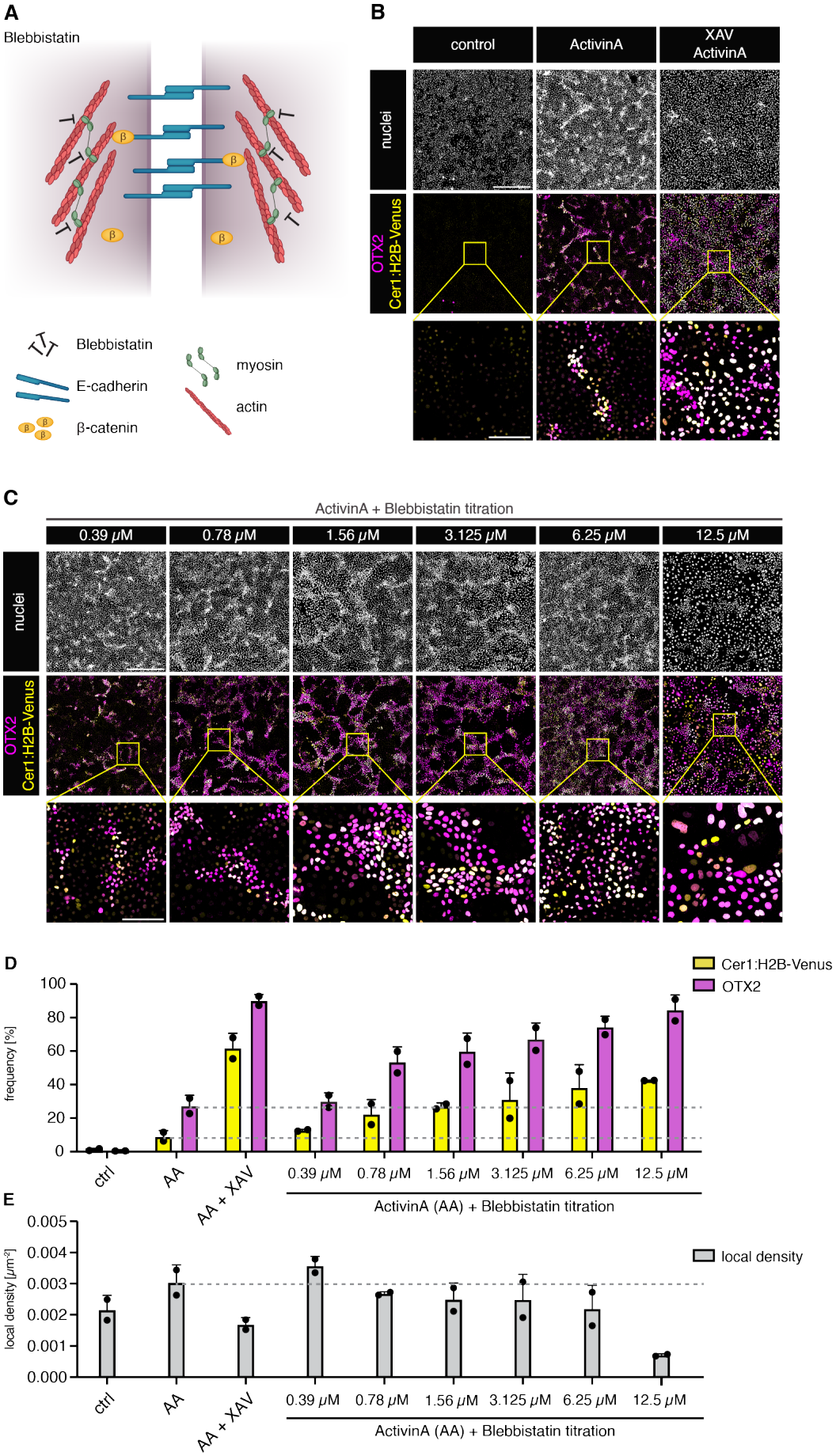
A
Blebbistatin
Blebbistatin
E-cadherin
β-catenin
myosin
actin
B
control
ActivinA
XAV ActivinA
nuclei
OTX2 Cer1:H2B-Venus
C
ActivinA + Blebbistatin titration
0.39 μM
0.78 μM
1.56 μM
3.125 μM
6.25 μM
12.5 μM
nuclei
OTX2 Cer1:H2B-Venus
D
Cer1:H2B-Venus
OTX2
frequency [%]
100
80
60
40
20
0
ctrl
AA
AA + XAV
0.39 μM
0.78 μM
1.56 μM
3.125 μM
6.25 μM
12.5 μM
ActivinA (AA) + Blebbistatin titration
E
local density
local density [μm⁻²]
0.005
0.004
0.003
0.002
0.001
0.000
ctrl
AA
AA + XAV
0.39 μM
0.78 μM
1.56 μM
3.125 μM
6.25 μM
12.5 μM
ActivinA (AA) + Blebbistatin titration

Figure 41: Blebbistatin increases number of AVE cells.
A Schematic of simplified adherens junctions manipulated by treatment with Blebbistatin**. B** Immunostaining of Cer1:H2B-Venus VE cells for the AVE marker OTX2 (magenta) and H2B-Venus (yellow). Cells were treated with 50 ng/ml ActivinA or together with 20 μM XAV939. Scale bar: 500 μm; inset 100 μm. **C** Same immunostaining as in A but cells were treated with 50 ng/ml ActivinA and different concentrations of Blebbistatin. Scale bar: 500 μm; inset 100 μm. **D** Quantification of VE cell frequency expressing Cer1:H2B-Venus or OTX2 via segmentation and fluorescence measurement of the images in B and C. N = 2. **E** Local density of the cells, measured as the mean distance to the 5 nearest neighbors and plotted as the inverse of the area.

4 Discussion

In this thesis, I investigated the mechanism of AVE differentiation with a particular focus on exploring a hidden self-organization mechanism. First, I established a bilayered embryo-like aggregate (BELA) system made solely from stem cells to mimic the Epi and VE compartment of the embryo at the time point of AVE differentiation. In contrast to the prevailing model for AVE differentiation, which suggests that an external inhibitory gradient spatially restricts and positions the AVE region, I found that BELAs differentiated a proper AVE region in their VE layer without the presence of the external inhibitory gradient. This surprising observation prompted me to investigate the minimal signals required to induce AVE differentiation using the BELA system. I demonstrated that Nodal signals from the Epi are both necessary and sufficient for initiating AVE differentiation. Subsequently, I developed a 2D AVE differentiation model in a pure population of VE cells, in which I observed that VE cells use a so far unknown tissue-intrinsic mechanism to spatially restrict AVE differentiation. Testing the role of various potential signaling pathways known to be pivotal in the embryo during the time of AVE differentiation, I identified β-catenin as a novel tissue-intrinsic signal within VE cells that acts to counterbalance AVE differentiation.

4.1 Establishment of an embryo-like aggregate model

In this thesis, I used a previously described mESC line containing a GATA4-inducible gene construct, known to differentiate upon transient GATA4 induction into robust proportions of Epi and PrE cells, the precursors of the VE (Raina et al., 2021). By seeding this cell mixture together onto a substrate with low adhesion properties, such as a low concentration of gelatin, cell-cell interactions were supported and the cells transformed from a 2D layer into floating aggregates (Figure 10B). These aggregates exhibited organized structures, comprising an inner Epi core surrounding a lumen, enveloped by an outer VE layer (Figure 11A,B). This approach closely mimics the differentiation trajectory in the embryo, where both Epi and PrE cells derive from the same precursor line. Similar models focusing on the Epi and VE compartment have been reported before, underscoring the interest in the niche of Epi and VE cells. While these models

share the structural composition of BELAs, they differ in their formation methods and the sources of VE cells. These models were generated by mixing mESCs with established XEN cell lines (Zhang et al., 2019), GATA-induced ESCs (Amadei et al., 2021), or chemically converted PrE cells (Vrij et al., 2022). Despite their various origins, all these combinations result in bilayered aggregates, demonstrating a significant similarity among different XEN and differentiated VE lines. However, their formation is typically induced through suspension aggregation or microcavity culture. Consequently, the dynamic interplay between the two cell types and the morphogenetic potential, especially of the PrE/VE cells, might be overlooked when they spontaneously transition from a 2D layer of cells into floating, organized aggregates.

Exploring the factors responsible for the morphogenetic event of BELA formation, I employed the previously established protocol to generate pure populations of induced PrE cells (Raina et al., 2021), unveiling the critical role of FGF4 secreted from the Epi cells in promoting PrE/VE cell survival and facilitating the unexpected formation of cystic structures (Figure 12B,C, Figure 13A). Remarkably, these VE cysts exhibited characteristics akin to the outer VE compartment in BELAs, featuring an inverted polarity for a cystic structure, where the apical domain faces outward and extracellular matrix secretion occurs towards the inside (Figure 14A-C). I speculate that the secretion of extracellular matrix proteins might play a role in the cyst formation. In which the extracellular short arms of laminin might polymerize and form a network (Li et al., 2003), that constrains the basal side of the cells resulting in the cyst formation. However, we made the observation in our lab that common XEN cell lines do not exhibit similar behavior upon FGF4 treatment suggesting potential differences in their cell identities of induced VE and tissue culture derived XEN cells (Schumacher et al., 2023; unpublished).

The inverted polarity of VE cells was found to be essential for the inner Epi cells in BELAs. Due to this polarity, the basal side with the secreted extracellular matrix proteins of the PrE/VE cells faces the Epi cells, enabling their attachment to the extracellular matrix. I further demonstrated that Epi cell survival and proper polarization, leading to lumen formation, depend on contact with extracellular matrix proteins via integrin receptors (Figure 16A,B, Figure 17C), consistent with the reported

phenotype in the embryo (Fassler & Meyer, 1995). However, while *Itgb1* mutant Epi cells failed to organize directed polarization in Matrigel (Epi cysts) (Bedzhov & Zernicka-Goetz, 2014), approximately 50% of BELAs with an *Itgb1* mutant Epi compartment exhibited normal morphogenesis. Recent work by (Molè et al., 2021) demonstrated that an *Itgb1* mutation does not prevent polarization itself but rather disrupts its maintenance, a defect that can be rescued with a combination of different factors. I speculate that PrE/VE cells may provide such additional factors to Epi cells, which are absent in Matrigel, potentially improving proper polarization.

Based on the findings regarding the morphogenetic potential of Epi and PrE/VE cells, I propose the following hypothesis concerning the aggregate formation process: The high motility of PrE cells, potentially influenced by short-range signals such as FGF4 secreted by Epi cells (Raina et al., 2021), contributes to the active aggregation of Epi and PrE cells into a specific 3D conformation. Subsequently, the connection of the Epi cells to the extracellular matrix of the PrE/VE cells facilitates polarization and lumenogenesis within the Epi compartment. Furthermore, I suggest that BELAs, along with Epi and VE cysts as controls, provide a unique model palette for further investigating the impact of communication between Epi and PrE/VE cells on aggregate formation and patterning.

4.2 AVE differentiation in BELAs

Epi and PrE/VE cells have demonstrated significant morphogenetic potential, prompting me to look into their potential for differentiation in BELAs. Therefore, single-cell RNA sequencing was employed, revealing a bifurcation among the VE cells, a phenomenon not observed in the Epi cells (Figure 19). Specifically, a subset of VE cells expressed genes characteristic of the anterior visceral endoderm (AVE), a unique feature exclusive to BELAs and not present in VE cysts, suggesting the necessity of Epi cells in inducing these marker expressions (Figure 20B). Integration of BELA scRNA seq data with a dataset focusing on AVE differentiation in the embryo (Thowfeequ et al., 2021) indicated that this cell subset closely resembled an AVE at E6.25 (Figure 21C). Surprisingly, these cells were confined to a coherent domain within the outer VE

layer in BELAs (Figure 22A-C, Figure 23C), reminiscent of distinct domains observed in the embryonic VE, with a smaller CER1-expressing domain inside a broader OTX2-expressing domain neighboring double-negative cells (Figure 27A,B) (Hoshino et al., 2015). These findings contrast with the conventional AVE model, which proposes restriction of AVE differentiation by an external BMP4 gradient from the ExE (Yamamoto et al., 2009), suggesting the existence of a previously unknown mechanism for AVE differentiation that may operate in addition to the gradient. The lack of bifurcation in Epi cells indicates the absence of differentiation signals, potentially including BMP from the ExE, which has been shown to be essential for mesoderm formation (Winnier et al., 1995).

In recent studies, AVE differentiation has been observed in models incorporating stem cell lines representing all three lineages and the morphology of the peri-implantation embryo (Amadei et al., 2021; Langkabel et al., 2021; Sozen et al., 2018; Zhang et al., 2019). These models consistently positioned AVE cells at the distal tip within the VE cells, farthest from the ExE. However, in cases where the embryo model contained minimal extraembryonic ectoderm, the AVE region extended (Langkabel et al., 2021). These embryo models also displayed a change in shape, adopting a round structure with a larger Epi and smaller ExE population inside. It remained uncertain whether the extension of the AVE region resulted from the smaller ExE domain size or their altered shape.

Furthermore, aggregates resembling the structure of BELAs, comprising only Epi and VE compartments, have been investigated for AVE differentiation. Aggregates formed from mESCs and XEN cells have been reported to express AVE marker genes such as *Lefty1* in their outer VE cells (Zhang et al., 2019). However, *Lefty1* expression appeared random and broad, with no *Otx2* expression detected in *Lefty1*-negative cells, suggesting an abnormal composition of the VE and AVE domains (Hoshino et al., 2015). Moreover, a cross-paper comparison of (Sozen et al., 2018) and (Amadei et al., 2021), both from the lab of Magdalena Zernicka-Goetz, revealed that GATA-induced PrE/VE cells, compared to XEN cells, more closely resemble the differentiation potential observed in embryos, including that for AVE. Additionally, chemically induced PrE cells in a PrE-/Epi-niche system, which closely resembles BELAs, did not provide clear

evidence for AVE differentiation based on single-cell RNA sequencing analysis (Vrij et al., 2022).

Collectively, these studies suggest that the AVE differentiation potential largely depends on the type of VE cells present in the system, with GATA-inducible PrE/VE cells demonstrating the highest AVE differentiation potential. It is speculated that XEN cells adopt a parietal endoderm character instead of a VE character, as evidenced by the absence of E-cadherin expression (Julio et al., 2011; Paca et al., 2012; Schumacher et al., 2023; unpublished). However, XEN cells were shown to transition to a VE-like state when exposed to recombinant Nodal protein (Julio et al., 2011) or BMP4 (Paca et al., 2012). BMP4 induced a mesenchymal-to-epithelial transition with upregulation of E-cadherin, converting the cell to an exVE, but not emVE identity. It would be insightful to conduct a comparative study of gene expression analysis for different XEN cells and induced VE cells to investigate potential differences corresponding to their potential for AVE differentiation.

4.3 A 2D AVE differentiation system

Investigating the signal responsible for inducing AVE differentiation in BELAs, Nodal, secreted throughout the epiblast, was identified as the crucial signal necessary for transitioning PrE into an embryonic VE identity (Vrij et al., 2022). Subsequently, Nodal drives AVE differentiation in the overlying VE (Brennan et al., 2001). Consistent with this, inhibition of Nodal signaling using the Nodal receptor inhibitor SB43 or mutation of the endogenous *Nodal* gene resulted in a complete loss of the AVE markers Otx2 and Cer1 (Figure 24B,C, Figure 25B).

I this thesis, I reported that activation of the Nodal signaling pathway alone, by using recombinant ActivinA, is sufficient to trigger AVE differentiation in VE cells (Figure 26). Within the VE layer, patches of AVE clusters formed that were patterned within themselves with a broader OTX+ domain and within a smaller CER1+ domain reminiscent of the composition observed in the VE of BELAs and the emVE of an embryo (Hoshino et al., 2015) (Figure 20B, Figure 26B). The clustered expression of AVE markers resulting from homogenous ActivinA treatment, points to a so far unknown tissue-intrinsic

mechanism in the VE cells to spatially restrict AVE differentiation. To the best of my knowledge, this is the first reported 2D model for AVE differentiation, presenting a valuable instrument to investigate the fundamental mechanisms underlying AVE differentiation in mice, with potential relevance to other mammalian species.

4.4 Signaling control of spatially restricted AVE differentiation

Next, I delved into the mechanism and signaling of the VE cells responsible for clustered AVE differentiation. Tissue differentiation and patterning can generally arise through two main concepts: an externally generated gradient of a signaling molecule, like a morphogen, which creates varying concentrations across a tissue (Wolpert, 1969), or through self-organization within the tissue itself (Gierer & Meinhardt, 1972; Green & Sharpe, 2015; Turing, 1952). The prevailing model in AVE differentiation suggests that an external gradient of BMP4 patterns the VE cells, spatially constraining and positioning the AVE region (Yamamoto et al., 2009). This mechanism is believed to involve a common receptor for NODAL-dependent AVE induction and BMP-dependent spatial restriction, which activates different intracellular signaling transducers: SMAD1 for BMP and SMAD2 for Nodal signaling.

However, in my 2D AVE differentiation system, where no external gradient is present, all indications point towards a self-organizing system. To explore this further at the molecular level, I investigated the role of three major signaling networks.

4.4.1 The effect of BMP on AVE differentiation

Although BMP4 does not operate as an external gradient in my system, I investigated the impact of recombinant BMP4 on my 2D AVE differentiation model. Additionally, I explored whether endogenous VE BMP signaling contributes to the restriction of AVE differentiation. Treating embryos with BMP4 from E5.2 to E5.5 resulted in the loss of AVE markers such as Hex, Lefty1, and Cer1, while the BMP4 inhibitor Noggin extended AVE marker expression (Yamamoto et al., 2009). Removal of the ExE led to

the loss of pSMAD1 signal and an extension of the AVE, but this expansion could be inhibited by culturing the explants in the presence of BMP4 (Rodriguez, 2005; Yamamoto et al., 2009).

In my 2D AVE system, I expected that BMP4 treatment would result in a loss of AVE marker expression similar to what was observed in embryos, assuming that the AVE differentiation model was correct. However, when VE cells induced with ActivinA to differentiate into AVE cells were additionally treated with BMP4, the number of AVE marker expressing cells decreased but was not completely lost (Figure 30). This observation partially aligns with the effects of the BMP4 gradient in embryos, which restricts AVE differentiation (Yamamoto et al., 2009). The enhanced impact of BMP4 treatment observed in embryos could be attributed to a potential alteration in the Epiblast induced by BMP4. This alteration might result in a stop of AVE induction, as evidenced by previous studies showing that BMP4 treatment of Epiblast stem cells induces the expression of T-Brachyury, a marker associated with the primitive streak (Kurek et al., 2015). Nonetheless, the fact that BMP4 treatment only reduced the number of AVE marker expressing cells without completely abolishing AVE differentiation suggests the presence of an additional tissue-intrinsic mechanism for AVE restriction.

BMP4 is predominantly expressed in the ExE during the period of AVE differentiation in embryos, while BMP2 is expressed in the visceral endoderm (Coucouvanis & Martin, 1999), prompting me to explore whether BMP2 might act as the intrinsic antagonistic signal for AVE differentiation. Consequently, I conducted tests using the BMP receptor inhibitor LDN (Figure 30). However, treatment with LDN did not result in any significant changes, indicating the absence of intrinsic BMP signaling in counteracting AVE differentiation.

Based on these results, it can be argued that BMP4 secreted as a gradient from the ExE may play a role in constraining AVE differentiation, as evidenced by its negative effect on AVE differentiation observed in my 2D model system. However, the finding that BMP4 treatment did not completely abolish AVE differentiation indicates the presence of an additional tissue-intrinsic mechanism. This mechanism adds robustness to the system and may aid in correctly positioning the AVE in the embryo.

4.4.2 Nodal and Lefty as activator-inhibitor pair

Given that BMP does not seem to be involved in the self-organizing patterning of the VE, another potential candidate pathway is the Nodal signaling pathway itself. Nodal, along with Lefty, has been identified as a potential activator-inhibitor pair in patterning systems (Gierer & Meinhardt, 1972; Muller et al., 2012; Turing, 1952). In this system, Nodal promotes its own expression while also inducing the expression of its inhibitor, Lefty1. However, their distinct diffusion rates result in a pattern of short-range activation combined with long-range inhibition.

To test the role of the endogenous Nodal and Lefty1 in the 2D AVE model, with respect to their function in a reaction-diffusion system, I applied ActivinA on *Nodal* and *Lefty1* mutant VE cells to trigger AVE differentiation (Figure 28B-D, Figure 29B). The expectation regarding a *Nodal* mutant was somewhat uncertain due to the constant activation of the Nodal signaling pathway by recombinant ActivinA protein. However, the mutation of *Lefty1* should certainly lead to an increase in AVE differentiation, potentially resulting in the overall conversion of all VE into an AVE fate due to the absence of the restriction signal. Loss of endogenous *Nodal* reduced slightly the number of Cer1:H2B-Venus/OTX2-double positive cells, yet had no significant effect on the complete number of OTX2+ cells and therefore did not completely disrupt AVE differentiation. Similar findings were reported by Kumar and colleagues (Kumar et al., 2015) where VE *Nodal* conditional mutants displayed failures of a proper AVE formation due to migration failure but showed proper induction of a DVE at the distal tip. This phenotype might be due to their observation that Nodal signaling from the VE is required to maintain Nodal signaling in the epiblast, potentially leading to an imbalance in the proposed BMP and Nodal antagonism during AVE induction (Yamamoto et al., 2009). Without the positive feedback of Nodal expression in the VE and therefore reduced Nodal expression in the epiblast, BMP4 expression may expand, potentially resulting in migration defects and a failure to recruit new AVE cells, as it is reported from Takaoka and colleagues (Takaoka et al., 2011).

Mutation of the endogenous *Lefty1* gene did not yield the expected outcome in the context of a reaction-diffusion system, as its mutation did not lead to an expansion in the number of Cer1:H2B-Venus expressing cells (Figure 29B). This finding aligns with

the reported *Lefty1* mutant overmigration phenotype in the embryo, where proper DVE induction occurs (Trichas et al., 2011). To speculate, the limited effect of *Lefty1* mutation on AVE specification could be attributed to functional redundancy of LEFTY1 and CER1 as both inhibit Nodal signaling (Aykul et al., 2015). This notion is supported by observations that expression of the AVE marker Hex was slightly expanded in *Lefty1*- and *Cer1*-double mutants (Yamamoto et al., 2004).

In summary, while the positive feedforward loop of Nodal expression may contribute to AVE differentiation, it does not appear to be essential as long as there is an external source of Nodal signaling activation, such as ActivinA in the 2D AVE model. Further investigation is needed to assess the impact of shorter treatments with ActivinA on the number of AVE cells. Moreover, to elucidate the potential functional redundancy of Lefty1 with factors like Cer1 and other antagonistic signals, additional mutations could provide valuable insights.

4.4.3 β-catenin as new antagonist for AVE differentiation

Given that BMP signaling and a Nodal/Lefty1 reaction-diffusion system failed to meet the criteria as the tissue-intrinsic signal spatially restricting AVE differentiation in VE cells, I shifted my attention to Wnt/β-catenin signaling. This decision was motivated by expression of a TCF/LEF:H2B-GFP reporter throughout the VE of embryos at the time of AVE specification (Figure 31) (Ferrer-Vaquer et al., 2010). The expression of several Wnt antagonists in the AVE as Sfrp1, Sfrp5 and Dkk1, further supported this idea (Rivera-Pérez & Hadjantonakis, 2014). Through experiments involving the activation or inhibition of β-catenin transcriptional activity with small molecules, I identified β-catenin as a strong negative regulator of AVE differentiation (Figure 32). This result is corroborated by findings in $Apc^{Min/Min}$ embryos, where APC, a component of the destruction complex responsible for directing the degradation of β-catenin via the proteasomal pathway (Valenta et al., 2012), is mutated, leading to hyperactivity of β-catenin (Chazaud & Rossant, 2006). In these embryos, a failure of DVE specification was observed, potentially due to posteriorization of the epiblast and subsequent failure of the same to induce an AVE. Chimeric embryos with a wildtype epiblast were also

unable to express the AVE marker genes *Lefty1* and *Cer1* in the DVE. Further support for this comes from reports showing that mutation of *β-catenin* leads to an increase in CER1 expression within the VE (Morkel et al., 2003).

Typically, β-catenin is considered the transducer for Wnt signals. However, in this case, mutation of the expressed Wnt ligands, *Wnt4* and *Wnt11*, resulted not in the expected phenotype of an expansion of AVE marker expression in the VE. Even inhibiting (Figure 32) or mutating Porcn (Figure 38), a small acyltransferase crucial for Wnt ligand modification and secretion, did not alter AVE marker expression. This outcome aligns with findings from (Biechele et al., 2013), who also observed unaffected AVE marker expression in *Porcn* mutant embryos. This result was unexpected, as the inhibition or mutation of Porcn was anticipated to disrupt any Wnt-mediated β-catenin signaling indicating that the activity of β-catenin was not controlled by Wnt ligands.

I speculated that if β-catenin is not controlled by Wnt ligands, it might be subject to mechanical regulation. This hypothesis was inspired by β-catenin's other role in cell adherens junctions, where it participates with other catenins in catch bonds, connecting the cytosolic tails of cadherins to the actin cytoskeleton. These catch bonds strengthen and elongate their lifetime in response to force (Wang et al., 2022). Therefore, I sought to modulate cell mechanics in adherens junctions to test its influence on AVE differentiation (Figure 40, Figure 41). Blocking E-cadherin binding sites with antibodies, preventing cell attachment and force application, increased the number of AVE-marker expressing cells (Figure 40). Similarly, treatment with the contractility inhibitor blebbistatin yielded comparable results. Blebbistatin does not inhibit cell binding but impedes their response to force, thereby inhibiting the catch bond (Figure 41).

These findings suggest that manipulating cell mechanics can influence AVE differentiation. While reducing cell-cell adhesion with E-cadherin blocking antibodies increased differentiation, a study demonstrated that stabilizing cell-cell adhesion prevented differentiation and symmetry breaking in gastruloids (Cermola et al., 2022). Additionally, I observed that cell density played a role in AVE differentiation (Figure 34). Lower cell density promoted differentiation, whereas higher cell density hindered

it, likely due to increased cell-cell contacts and higher mechanical stress at higher confluency, which may inhibit differentiation.

Recent studies in zebrafish embryos have shown that Nodal signaling promotes cell contact formation mediated by E-cadherins and creates a positive feedback loop between cell-cell contact duration and Nodal signaling, which can influence cell fate determination (Barone et al., 2017). This finding aligns with my observations that AVE marker-expressing cells, which also express Nodal, exhibit higher levels of E-cadherin compared to surrounding cells that do not express AVE markers (Figure 39). Furthermore, mechanical forces have been proposed as a significant signal in embryonic self-organization functioning akin to Turing's molecular reaction-diffusion system (Caldarelli et al., 2021; Turing, 1952). In this model, contractility acts as a local activator, while induced tension serves as a long-range inhibitor. Analogous to a Turing model, this system can support the spontaneous emergence and stable maintenance of domains of high and low contractility

In the future, investigating the concept of a mechanical Turing system within the 2D AVE model and its implications for embryonic development could provide valuable insights into this complex biological process of AVE differentiation. It may offer new avenues for deepening our understanding of embryonic patterning and development within this field.

4.5 Conclusions and future directions

In this thesis, I investigated a potential self-organization aspect in AVE differentiation in contrast to the current model stating that an external gradient is necessary to position the AVE. I established an aggregate system that resembles the Epi and VE compartments of the embryo and found that this system can form a spatially restricted AVE region without the presence an external inhibitory gradient. After identifying Nodal signaling as the necessary AVE induction signal from the Epi, I established a 2D AVE, where VE cells differentiate clusters of AVE cells upon homogenous treatment with recombinant ActivinA to induce Nodal signaling. This result showed that the VE cells have a tissue intrinsic mechanism to self-organize the spatial restriction of an AVE.

The primary advantage of this 2D AVE model lies in its minimal complexity and lack of communication with other tissues, in contrast to more complex systems like BELAs or iETX embryoids (Amadei et al., 2021). Treating an entire embryo with small inhibitors can often pose challenges in deciphering whether the inhibitor directly affects AVE differentiation or interferes with Epi cells, preventing the initiation of AVE differentiation altogether. By applying such small inhibitors to the 2D AVE system, I identified β-catenin as a counteracting signal for AVE differentiation, regulated not by Wnt signaling but by mechanics within adherens junctions. This discovery suggests that the symmetry-breaking event underlying AVE differentiation may be orchestrated through a mechanical rather than a chemical patterning system.

This novel aspect of self-organization in AVE differentiation may complement the existing inhibitory gradient mechanism in the mouse embryo as guided symmetry breaking system. In this intricate interplay, both external and intrinsic mechanisms collaborate to regulate AVE differentiation, thereby enhancing the robustness of the patterning system.

Continuing this research, I aim to investigate whether the spatial positioning of cells within a colony contributes to AVE differentiation as they experience different strengths of cell-cell adhesion. To accomplish this, I propose applying the 2D AVE differentiation protocol to VE cells seeded on micropatterns with different sizes. If cells with lower cell adhesion are designated to become the AVE, I anticipate that only the cells positioned at the outer edges of the micropatterns will undergo AVE differentiation. Furthermore, integrating time-lapse imaging with the AVE reporter Cer1:H2B-Venus during AVE differentiation will facilitate the tracking of initial reporter expression in cell locations and enable observation of whether these cells subsequently induce neighboring cells with slightly different positions. Moreover, adjusting the sizes of these micropatterns will offer valuable insights into determining the minimal distance required for multiple AVE inductions. In addition to examining cell position, considering the role of cell contractility in AVE differentiation, I suggest utilizing beads soaked in Calyculin A or H1152 to modulate myosin II activity, as outlined by (Caldarelli et al., 2021). To explore whether a mechanical reaction-diffusion mechanism governs the spatial restriction of AVE differentiation, beads can be employed to locally enhance cell contractility through

increased myosin II activity. This enhancement can induce ectopic contraction foci, potentially leading to AVE formation around the bead.

Thinking further than the mouse embryo and with regard to the rapidly growing field of human embryo models, it would be an enticing prospect to extend the 2D AVE differentiation protocol to human and other mammalian cells. Given the different shape of human embryos compared to mice, it is plausible that human embryos lack an external gradient for spatially constraining AVE differentiation. Thus, a pressing question in the field pertains how the human embryo orchestrates AVE differentiation and positioning. Notably, differentiation methods for human VE (called hypoblast) have already been established utilizing a GATA-inducible system similar to that used in mouse models and also in this thesis (Okubo et al., 2024; Weatherbee et al., 2023). This presents an excellent opportunity to investigate whether these human cells can also be induced to form a pure layer of hypoblast cells (corresponding to VE in mouse) and whether similar induction and restriction mechanism govern the formation of a spatially restricted anterior hypoblast (corresponding to AVE in mouse). This exploration would provide great insight into whether activating the Nodal signaling pathway in human induced hypoblast cells is sufficient to induce an anterior character, akin to findings in the mouse model in this thesis. Furthermore, investigating whether human hypoblast cells harbor a tissue-intrinsic mechanism for spatially constraining AVE differentiation, and whether this mechanism is influenced by β-catenin as proposed for mice, holds significant scientific interest. Such comparative studies between species could shed light on conserved developmental processes and contribute to our understanding of human embryonic development.

5 References

Acampora, D., Mazan, S., Lallemand, Y., Avantaggiato, V., Maury, M., Simeone, A., & Brûlet, P. (1995). Forebrain and midbrain regions are deleted in *Otx2* −/− mutants due to a defective anterior neuroectoderm specification during gastrulation. *Development*, *121*(10), 3279–3290. https://doi.org/10.1242/dev.121.10.3279

Albano, R. M., Groome, N., & Smith, J. C. (1993). Activins are expressed in preimplantation mouse embryos and in ES and EC cells and are regulated on their differentiation. *Development*, *117*(2), 711–723. https://doi.org/10.1242/dev.117.2.711

Amadei, G., Handford, C. E., Qiu, C., De Jonghe, J., Greenfeld, H., Tran, M., Martin, B. K., Chen, D.-Y., Aguilera-Castrejon, A., Hanna, J. H., Elowitz, M. B., Hollfelder, F., Shendure, J., Glover, D. M., & Zernicka-Goetz, M. (2022). Embryo model completes gastrulation to neurulation and organogenesis. *Nature*, *610*(7930), 143–153. https://doi.org/10.1038/s41586-022-05246-3

Amadei, G., Lau, K. Y. C., De Jonghe, J., Gantner, C. W., Sozen, B., Chan, C., Zhu, M., Kyprianou, C., Hollfelder, F., & Zernicka-Goetz, M. (2021). Inducible Stem-Cell-Derived Embryos Capture Mouse Morphogenetic Events In Vitro. *Developmental Cell*, *56*(3), 366-382.e9. https://doi.org/10.1016/j.devcel.2020.12.004

Anton, R., Kestler, H. A., & Kühl, M. (2007). β-Catenin signaling contributes to stemness and regulates early differentiation in murine embryonic stem cells. *FEBS Letters*, *581*(27), 5247–5254. https://doi.org/10.1016/j.febslet.2007.10.012

Arnold, S. J., & Robertson, E. J. (2009). Making a commitment: cell lineage allocation and axis patterning in the early mouse embryo. *Nature Reviews Molecular Cell Biology*, *10*(2), 91–103. https://doi.org/10.1038/nrm2618

Aykul, S., Ni, W., Mutatu, W., & Martinez-Hackert, E. (2015). Human Cerberus Prevents Nodal-Receptor Binding, Inhibits Nodal Signaling, and Suppresses Nodal-Mediated Phenotypes. *PLOS ONE*, *10*(1), e0114954. https://doi.org/10.1371/journal.pone.0114954

Barone, V., Lang, M., Krens, S. F. G., Pradhan, S. J., Shamipour, S., Sako, K., Sikora, M., Guet, C. C., & Heisenberg, C.-P. (2017). An Effective Feedback Loop between Cell-Cell Contact Duration and Morphogen Signaling Determines Cell Fate. *Developmental Cell*, *43*(2), 198-211.e12. https://doi.org/10.1016/j.devcel.2017.09.014

Beccari, L., Moris, N., Girgin, M., Turner, D. A., Baillie-Johnson, P., Cossy, A.-C., Lutolf, M. P., Duboule, D., & Arias, A. M. (2018). Multi-axial self-organization properties of mouse embryonic stem cells into gastruloids. *Nature*, *562*(7726), 272–276. https://doi.org/10.1038/s41586-018-0578-0

Beddington, R. S. P. (1990). Clonal analysis of cell lineages. *Postimplantation Mammalian Embryos, A Practical Approach*, 267–291. https://cir.nii.ac.jp/crid/1573950399407665920.bib?lang=en

Bedzhov, I., & Zernicka-Goetz, M. (2014). Self-organizing properties of mouse pluripotent cells initiate morphogenesis upon implantation. *Cell*, *156*(5), 1032–1044. https://doi.org/10.1016/j.cell.2014.01.023

Bérenger-Currias, N. M. L. P., Mircea, M., Adegeest, E., Berg, P. R. van den, Feliksik, M., Hochane, M., Idema, T., Tans, S. J., & Semrau, S. (2020). Early neurulation recapitulated in assemblies of embryonic and extraembryonic cells. *BioRxiv*, 2020.02.13.947655. https://doi.org/10.1101/2020.02.13.947655

Bevilacqua, E. M., & Abrahamsohn, P. A. (1989). Trophoblast invasion during implantation of the mouse embryo. *Archivos de Biologia y Medicina Experimentales*, *22*(2), 107–118.

Bhatt, S., Diaz, R., & Trainor, P. A. (2013). Signals and Switches in Mammalian Neural Crest Cell Differentiation. *Cold Spring Harbor Perspectives in Biology*, *5*(2), a008326–a008326. https://doi.org/10.1101/cshperspect.a008326

Biechele, S., Cockburn, K., Lanner, F., Cox, B. J., & Rossant, J. (2013). Porcn-dependent Wnt signaling is not required prior to mouse gastrulation. *Development (Cambridge, England)*, *140*(14), 2961–2971. https://doi.org/10.1242/dev.094458

Blau, H. M., Brazelton, T. R., & Weimann, J. M. (2001). The Evolving Concept of a Stem Cell. *Cell*, *105*(7), 829–841. https://doi.org/10.1016/S0092-8674(01)00409-3

Bouvard, D., Brakebusch, C., Gustafsson, E., Aszódi, A., Bengtsson, T., Berna, A., & Fässler, R. (2001). Functional Consequences of Integrin Gene Mutations in Mice. *Circulation Research*, *89*(3), 211–223. https://doi.org/10.1161/hh1501.094874

Brennan, J., Lu, C. C., Norris, D. P., Rodriguez, T. A., Beddington, R. S. P., & Robertson, E. J. (2001). Nodal signalling in the epiblast patterns the early mouse embryo. *Nature*, *411*(6840), 965–969. https://doi.org/10.1038/35082103

Brown, N. H. (2011). Extracellular matrix in development: insights from mechanisms conserved between invertebrates and vertebrates. *Cold Spring Harbor Perspectives in Biology*, *3*(12). https://doi.org/10.1101/cshperspect.a005082

Buckley, C. D., Tan, J., Anderson, K. L., Hanein, D., Volkmann, N., Weis, W. I., Nelson, W. J., & Dunn, A. R. (2014). The minimal cadherin-catenin complex binds to actin filaments under force. *Science*, *346*(6209). https://doi.org/10.1126/science.1254211

Burdon, T., Stracey, C., Chambers, I., Nichols, J., & Smith, A. (1999). Suppression of SHP-2 and ERK Signalling Promotes Self-Renewal of Mouse Embryonic Stem Cells. *Developmental Biology*, *210*(1), 30–43. https://doi.org/10.1006/dbio.1999.9265

Caldarelli, P., Chamolly, A., Alegria-Prévot, O., Gros, J., & Corson, F. (2021). Self-organized tissue mechanics underlie embryonic regulation. *BioRxiv*, 2021.10.08.463661. https://doi.org/10.1101/2021.10.08.463661

Cermola, F., Amoroso, F., Saracino, F., Ibello, E., De Cesare, D., Fico, A., Cobellis, G., Scalera, E., Casiraghi, C., D'Aniello, C., Patriarca, E. J., & Minchiotti, G. (2022). Stabilization of cell-cell adhesions prevents symmetry breaking and locks in pluripotency in 3D gastruloids. *Stem Cell Reports*, *17*(11), 2548–2564. https://doi.org/10.1016/j.stemcr.2022.09.013

Chazaud, C., & Rossant, J. (2006). Disruption of early proximodistal patterning and AVE formation in Apc mutants. *Development (Cambridge, England)*, *133*(17), 3379–3387. https://doi.org/10.1242/dev.02523

Chen, C., & Shen, M. M. (2004). Two Modes by which Lefty Proteins Inhibit Nodal Signaling. *Current Biology*, *14*(7), 618–624. https://doi.org/10.1016/j.cub.2004.02.042

Chng, Z., Vallier, L., & Pedersen, R. (2011). *Activin/Nodal Signaling and Pluripotency* (pp. 39–58). https://doi.org/10.1016/B978-0-12-385961-7.00003-2

Choi, H. M. T., Schwarzkopf, M., Fornace, M. E., Acharya, A., Artavanis, G., Stegmaier, J., Cunha, A., & Pierce, N. A. (2018). Third-generation in situ hybridization chain reaction: multiplexed, quantitative, sensitive, versatile, robust. *Development*, *145*(12), dev165753. https://doi.org/10.1242/dev.165753

Conlon, F. L., Lyons, K. M., Takaesu, N., Barth, K. S., Kispert, A., Herrmann, B., & Robertson, E. J. (1994). A primary requirement for *nodal* in the formation and maintenance of the primitive streak in the mouse. *Development*, *120*(7), 1919–1928. https://doi.org/10.1242/dev.120.7.1919

Constam, D. B. (2014). Regulation of TGFβ and related signals by precursor processing. *Seminars in Cell & Developmental Biology*, *32*, 85–97. https://doi.org/10.1016/j.semcdb.2014.01.008

Coucouvanis, E., & Martin, G. R. (1999). BMP signaling plays a role in visceral endoderm differentiation and cavitation in the early mouse embryo. *Development*, *126*(3), 535–546. https://doi.org/10.1242/dev.126.3.535

Daniels, D. L., & Weis, W. I. (2005). β-catenin directly displaces Groucho/TLE repressors from Tcf/Lef in Wnt-mediated transcription activation. *Nature Structural & Molecular Biology*, *12*(4), 364–371. https://doi.org/10.1038/nsmb912

Dimitrov, D., Türei, D., Garrido-Rodriguez, M., Burmedi, P. L., Nagai, J. S., Boys, C., Ramirez Flores, R. O., Kim, H., Szalai, B., Costa, I. G., Valdeolivas, A., Dugourd, A., & Saez-Rodriguez, J. (2022). Comparison of methods and resources for cell-cell communication inference from single-cell RNA-Seq data. *Nature Communications*, *13*(1), 3224. https://doi.org/10.1038/s41467-022-30755-0

Doench, J. G., Fusi, N., Sullender, M., Hegde, M., Vaimberg, E. W., Donovan, K. F., Smith, I., Tothova, Z., Wilen, C., Orchard, R., Virgin, H. W., Listgarten, J., & Root, D. E. (2016). Optimized sgRNA design to maximize activity and minimize off-target effects of CRISPR-Cas9. *Nature Biotechnology*, *34*(2), 184–191. https://doi.org/10.1038/nbt.3437

Driever, W., & Nüsslein-Volhard, C. (1988). A gradient of bicoid protein in Drosophila embryos. *Cell*, *54*(1), 83–93. https://doi.org/10.1016/0092-8674(88)90182-1

Dupont, C., Schäffers, O. J. M., Tan, B. F., Merzouk, S., Bindels, E. M., Zwijsen, A., Huylebroeck, D., & Gribnau, J. (2023). Efficient generation of ETX embryoids that recapitulate the entire window of murine egg cylinder development. *Science Advances*, *9*(3). https://doi.org/10.1126/sciadv.add2913

Evans, M. J., & Kaufman, M. H. (1981). Establishment in culture of pluripotential cells from mouse embryos. *Nature*, *292*(5819), 154–156. https://doi.org/10.1038/292154a0

Fassler, R., & Meyer, M. (1995). Consequences of lack of beta 1 integrin gene expression in mice. *Genes & Development*, *9*(15), 1896–1908. https://doi.org/10.1101/gad.9.15.1896

Ferrer-Vaquer, A., Piliszek, A., Tian, G., Aho, R. J., Dufort, D., & Hadjantonakis, A.-K. (2010). A sensitive and bright single-cell resolution live imaging reporter of Wnt/ß-catenin signaling in the mouse. *BMC Developmental Biology*, *10*(1), 121. https://doi.org/10.1186/1471-213X-10-121

Fu, J., Warmflash, A., & Lutolf, M. P. (2021). Stem-cell-based embryo models for fundamental research and translation. *Nature Materials*, *20*(2), 132–144. https://doi.org/10.1038/s41563-020-00829-9

Fujikura, J., Yamato, E., Yonemura, S., Hosoda, K., Masui, S., Nakao, K., Miyazaki, J., & Niwa, H. (2002). Differentiation of embryonic stem cells is induced by GATA factors. *Genes & Development*, *16*(7), 784–789. https://doi.org/10.1101/gad.968802

Fujiwara, T., Dehart, D. B., Sulik, K. K., & Hogan, B. L. M. (2002). Distinct requirements for extra-embryonic and embryonic bone morphogenetic protein 4 in the formation of the node and primitive streak and coordination of left-right asymmetry in the mouse. *Development*, *129*(20), 4685–4696. https://doi.org/10.1242/dev.129.20.4685

Furtado, M. B., Solloway, M. J., Jones, V. J., Costa, M. W., Biben, C., Wolstein, O., Preis, J. I., Sparrow, D. B., Saga, Y., Dunwoodie, S. L., Robertson, E. J., Tam, P. P. L., & Harvey, R. P. (2008). BMP/SMAD1 signaling sets a threshold for the left/right pathway in lateral plate mesoderm and limits availability of SMAD4. *Genes & Development*, *22*(21), 3037–3049. https://doi.org/10.1101/gad.1682108

Gierer, A., & Meinhardt, H. (1972). A theory of biological pattern formation. *Kybernetik*, *12*(1), 30–39. https://doi.org/10.1007/BF00289234

Goldberger, J., Hinton, G. E., Roweis, S., & Salakhutdinov, R. R. (2004). Neighbourhood Components Analysis. In L. Saul, Y. Weiss, & L. Bottou (Eds.), *Advances in Neural Information Processing Systems* (Vol. 17). MIT Press. https://proceedings.neurips.cc/paper_files/paper/2004/file/42fe880812925e520249e808937738d2-Paper.pdf

Green, J. B. A., & Sharpe, J. (2015). Positional information and reaction-diffusion: two big ideas in developmental biology combine. *Development (Cambridge, England)*, *142*(7), 1203–1211. https://doi.org/10.1242/dev.114991

Gritsman, K., Zhang, J., Cheng, S., Heckscher, E., Talbot, W. S., & Schier, A. F. (1999). The EGF-CFC Protein One-Eyed Pinhead Is Essential for Nodal Signaling. *Cell*, *97*(1), 121–132. https://doi.org/10.1016/S0092-8674(00)80720-5

Habas, R., & Dawid, I. B. (2005). Dishevelled and Wnt signaling: is the nucleus the final frontier? *Journal of Biology*, *4*(1), 2. https://doi.org/10.1186/jbiol22

Hao, Y., Hao, S., Andersen-Nissen, E., Mauck, W. M., Zheng, S., Butler, A., Lee, M. J., Wilk, A. J., Darby, C., Zager, M., Hoffman, P., Stoeckius, M., Papalexi, E., Mimitou, E. P., Jain, J., Srivastava, A., Stuart, T., Fleming, L. M., Yeung, B., … Satija, R. (2021). Integrated analysis of multimodal single-cell data. *Cell*, *184*(13), 3573-3587.e29. https://doi.org/10.1016/j.cell.2021.04.048

Hislop, J., Song, Q., Keshavarz F., K., Alavi, A., Schoenberger, R., LeGraw, R., Velazquez, J. J., Mokhtari, T., Taheri, M. N., Rytel, M., Chuva de Sousa Lopes, S. M., Watkins, S., Stolz, D., Kiani, S., Sozen, B., Bar-Joseph, Z., & Ebrahimkhani, M. R. (2024). Modelling post-implantation human development to yolk sac blood emergence. *Nature*, *626*(7998), 367–376. https://doi.org/10.1038/s41586-023-06914-8

Hooper, M., Hardy, K., Handyside, A., Hunter, S., & Monk, M. (1987). HPRT-deficient (Lesch-Nyhan) mouse embryos derived from germline colonization by cultured cells. *Nature*, *326*(6110), 292–295. https://doi.org/10.1038/326292a0

Hoshino, H., Shioi, G., & Aizawa, S. (2015). AVE protein expression and visceral endoderm cell behavior during anterior–posterior axis formation in mouse embryos: Asymmetry in OTX2 and DKK1 expression. *Developmental Biology*, *402*(2), 175–191. https://doi.org/10.1016/J.YDBIO.2015.03.023

Huang, S.-M. A., Mishina, Y. M., Liu, S., Cheung, A., Stegmeier, F., Michaud, G. A., Charlat, O., Wiellette, E., Zhang, Y., Wiessner, S., Hild, M., Shi, X., Wilson, C. J., Mickanin, C., Myer, V., Fazal, A., Tomlinson, R., Serluca, F., Shao, W., … Cong, F. (2009). Tankyrase inhibition stabilizes axin and antagonizes Wnt signalling. *Nature*, *461*(7264), 614–620. https://doi.org/10.1038/nature08356

Iannaccone, P. M., Zhou, X., Khokha, M., Boucher, D., & Kuehn, M. R. (1992). Insertional mutation of a gene involved in growth regulation of the early mouse embryo. *Developmental Dynamics*, *194*(3), 198–208. https://doi.org/10.1002/aja.1001940305

Johnston, D. St., Driever, W., Berleth, T., Richstein, S., & Nüsslein-Volhard, C. (1989). Multiple steps in the localization of *bicoid* RNA to the anterior pole of the *Drosophila* oocyte. *Development*, *107*(Supplement), 13–19. https://doi.org/10.1242/dev.107.Supplement.13

Julio, M. K., Alvarez, M. J., Galli, A., Chu, J., Price, S. M., Califano, A., & Shen, M. M. (2011). Regulation of extra-embryonic endoderm stem cell differentiation by Nodal and Cripto signaling. *Development*, *138*(18), 3885–3895. https://doi.org/10.1242/dev.065656

Kim, Y. S., & Bedzhov, I. (2022). Mechanisms of formation and functions of the early embryonic cavities. *Seminars in Cell & Developmental Biology*, *131*, 110–116. https://doi.org/10.1016/j.semcdb.2022.04.020

Kimelman, D., & Martin, B. L. (2012). Anterior–posterior patterning in early development: three strategies. *WIREs Developmental Biology*, *1*(2), 253–266. https://doi.org/10.1002/wdev.25

Kimura, C., Yoshinaga, K., Tian, E., Suzuki, M., Aizawa, S., & Matsuo, I. (2000). Visceral Endoderm Mediates Forebrain Development by Suppressing Posteriorizing Signals. *Developmental Biology*, *225*(2), 304–321. https://doi.org/10.1006/dbio.2000.9835

Kumar, A., Lualdi, M., Lyozin, G. T., Sharma, P., Loncarek, J., Fu, X.-Y., & Kuehn, M. R. (2015). Nodal signaling from the visceral endoderm is required to maintain Nodal gene expression in the epiblast and drive DVE/AVE migration. *Developmental Biology*, *400*(1), 1–9. https://doi.org/10.1016/j.ydbio.2014.12.016

Kunath, T., Saba-El-Leil, M. K., Almousailleakh, M., Wray, J., Meloche, S., & Smith, A. (2007). FGF stimulation of the Erk1/2 signalling cascade triggers transition of pluripotent embryonic stem cells from self-renewal to lineage commitment. *Development*, *134*(16), 2895–2902. https://doi.org/10.1242/dev.02880

Kurek, D., Neagu, A., Tastemel, M., Tüysüz, N., Lehmann, J., van de Werken, H. J. G., Philipsen, S., van der Linden, R., Maas, A., van IJcken, W. F. J., Drukker, M., & ten Berge, D. (2015). Endogenous WNT Signals Mediate BMP-Induced and Spontaneous Differentiation of Epiblast Stem Cells and Human Embryonic Stem Cells. *Stem Cell Reports*, *4*(1), 114–128. https://doi.org/10.1016/j.stemcr.2014.11.007

Langkabel, J., Horne, A., Bonaguro, L., Hesse, T., Knaus, A., Riedel, Y., Händler, K., Bassler, K., Reusch, N., Yeghiazarian, L. H., Pecht, T., Aschenbrenner, A. C., Kaiser, F., Kubaczka, C., Schultze, J. L., & Schorle, H. (2021). Induction of peri-implantation stage synthetic embryos using reprogramming paradigms in ESCs. *BioRxiv*, 2021.01.25.428068. https://doi.org/10.1101/2021.01.25.428068

Lau, K. Y. C., Rubinstein, H., Gantner, C. W., Hadas, R., Amadei, G., Stelzer, Y., & Zernicka-Goetz, M. (2022). Mouse embryo model derived exclusively from embryonic stem cells undergoes neurulation and heart development. *Cell Stem Cell*, *29*(10), 1445-1458.e8. https://doi.org/10.1016/j.stem.2022.08.013

Levine, A. J., & Brivanlou, A. H. (2006). GDF3, a BMP inhibitor, regulates cell fate in stem cells and early embryos. *Development*, *133*(2), 209–216. https://doi.org/10.1242/dev.02192

Li, S., Edgar, D., Fässler, R., Wadsworth, W., & Yurchenco, P. D. (2003). The role of laminin in embryonic cell polarization and tissue organization. *Developmental Cell*, *4*(5), 613–624. https://doi.org/10.1016/s1534-5807(03)00128-x

Liu, J., Xiao, Q., Xiao, J., Niu, C., Li, Y., Zhang, X., Zhou, Z., Shu, G., & Yin, G. (2022). Wnt/β-catenin signalling: function, biological mechanisms, and therapeutic opportunities. *Signal Transduction and Targeted Therapy*, *7*(1), 3. https://doi.org/10.1038/s41392-021-00762-6

Matzuk, M. M., Kumar, T. R., & Bradley, A. (1995). Different phenotypes for mice deficient in either activins or activin receptor type II. *Nature*, *374*(6520), 356–360. https://doi.org/10.1038/374356a0

Mège, R. M., & Ishiyama, N. (2017). Integration of Cadherin Adhesion and Cytoskeleton at *Adherens* Junctions. *Cold Spring Harbor Perspectives in Biology*, *9*(5), a028738. https://doi.org/10.1101/cshperspect.a028738

Mesnard, D., Filipe, M., Belo, J. A., & Zernicka-Goetz, M. (2004). The anterior-posterior axis emerges respecting the morphology of the mouse embryo that changes and aligns with the uterus before gastrulation. *Current Biology : CB*, *14*(3), 184–196. https://doi.org/10.1016/j.cub.2004.01.026

Mesnard, D., Guzman-Ayala, M., & Constam, D. B. (2006). Nodal specifies embryonic visceral endoderm and sustains pluripotent cells in the epiblast before overt axial patterning. *Development*, *133*(13), 2497–2505. https://doi.org/10.1242/dev.02413

Mihajlović, A. I., & Bruce, A. W. (2017). The first cell-fate decision of mouse preimplantation embryo development: integrating cell position and polarity. *Open Biology*, *7*(11), 170210. https://doi.org/10.1098/rsob.170210

Mitalipov, S., & Wolf, D. (2009). Totipotency, Pluripotency and Nuclear Reprogramming. In *Engineering of Stem Cells* (pp. 185–199). Springer Berlin Heidelberg. https://doi.org/10.1007/10_2008_45

Molè, M. A., Coorens, T. H. H., Shahbazi, M. N., Weberling, A., Weatherbee, B. A. T., Gantner, C. W., Sancho-Serra, C., Richardson, L., Drinkwater, A., Syed, N., Engley, S., Snell, P., Christie, L., Elder, K., Campbell, A., Fishel, S., Behjati, S., Vento-Tormo, R., & Zernicka-Goetz, M. (2021). A single cell characterisation of human embryogenesis identifies pluripotency transitions and putative anterior hypoblast centre. *Nature Communications*, *12*(1), 3679. https://doi.org/10.1038/s41467-021-23758-w

Morgani, S. M., Saiz, N., Garg, V., Raina, D., Simon, C. S., Kang, M., Arias, A. M., Nichols, J., Schröter, C., & Hadjantonakis, A.-K. (2018). A Sprouty4 reporter to monitor FGF/ERK signaling activity in ESCs and mice. *Developmental Biology*, *441*(1), 104–126. https://doi.org/10.1016/j.ydbio.2018.06.017

Moris, N., Anlas, K., van den Brink, S. C., Alemany, A., Schröder, J., Ghimire, S., Balayo, T., van Oudenaarden, A., & Martinez Arias, A. (2020). An in vitro model of early anteroposterior organization during human development. *Nature*, *582*(7812), 410–415. https://doi.org/10.1038/s41586-020-2383-9

Morkel, M., Huelsken, J., Wakamiya, M., Ding, J., van de Wetering, M., Clevers, H., Taketo, M. M., Behringer, R. R., Shen, M. M., & Birchmeier, W. (2003). β-Catenin regulates Cripto- and Wnt3-dependent gene expression programs in mouse axis and mesoderm formation. *Development*, *130*(25), 6283–6294. https://doi.org/10.1242/dev.00859

Müller-Wille, S. (2010). Cell theory, specificity, and reproduction, 1837–1870. *Studies in History and Philosophy of Science Part C: Studies in History and Philosophy of Biological and Biomedical Sciences*, *41*(3), 225–231. https://doi.org/10.1016/j.shpsc.2010.07.008

Müller, P., & Nüsslein-Volhard, C. (2016). Obituary: Hans Meinhardt (1938-2016). *Development*. https://doi.org/10.1242/dev.137414

Muller, P., Rogers, K. W., Jordan, B. M., Lee, J. S., Robson, D., Ramanathan, S., & Schier, A. F. (2012). Differential Diffusivity of Nodal and Lefty Underlies a Reaction-Diffusion Patterning System. *Science*, *336*(6082). https://doi.org/10.1126/science.1221920

Nakamura, T., Mine, N., Nakaguchi, E., Mochizuki, A., Yamamoto, M., Yashiro, K., Meno, C., & Hamada, H. (2006). Generation of Robust Left-Right Asymmetry in the Mouse Embryo Requires a Self-Enhancement and Lateral-Inhibition System. *Developmental Cell*, *11*(4), 495–504. https://doi.org/10.1016/j.devcel.2006.08.002

Niakan, K. K., Schrode, N., Cho, L. T. Y., & Hadjantonakis, A.-K. (2013). Derivation of extraembryonic endoderm stem (XEN) cells from mouse embryos and embryonic stem cells. *Nature Protocols*, *8*(6), 1028–1041. https://doi.org/10.1038/nprot.2013.049

Nowotschin, S., Costello, I., Piliszek, A., Kwon, G. S., Mao, C., Klein, W. H., Robertson, E. J., & Hadjantonakis, A.-K. (2013). The T-box transcription factor Eomesodermin is essential for AVE induction in the mouse embryo. *Genes & Development*, *27*(9), 997–1002. https://doi.org/10.1101/gad.215152.113

Nusse, R., Brown, A., Papkoff, J., Scambler, P., Shackleford, G., McMahon, A., Moon, R., & Varmus, H. (1991). A new nomenclature for int-1 and related genes: the Wnt gene family. *Cell*, *64*(2), 231. https://doi.org/10.1016/0092-8674(91)90633-a

Okubo, T., Rivron, N., Kabata, M., Masaki, H., Kishimoto, K., Semi, K., Nakajima-Koyama, M., Kunitomi, H., Kaswandy, B., Sato, H., Nakauchi, H., Woltjen, K., Saitou, M., Sasaki, E., Yamamoto, T., & Takashima, Y. (2024). Hypoblast from human pluripotent stem cells regulates epiblast development. *Nature*, *626*(7998), 357–366. https://doi.org/10.1038/s41586-023-06871-2

Oldak, B., Wildschutz, E., Bondarenko, V., Comar, M.-Y., Zhao, C., Aguilera-Castrejon, A., Tarazi, S., Viukov, S., Pham, T. X. A., Ashouokhi, S., Lokshtanov, D., Roncato, F., Ariel, E., Rose, M., Livnat, N., Shani, T., Joubran, C., Cohen, R., Addadi, Y., … Hanna, J. H. (2023). Complete human day 14 post-implantation embryo models from naive ES cells. *Nature*. https://doi.org/10.1038/s41586-023-06604-5

Orietti, L. C., Rosa, V. S., Antonica, F., Kyprianou, C., Mansfield, W., Marques-Souza, H., Shahbazi, M. N., & Zernicka-Goetz, M. (2021). Embryo size regulates the timing and mechanism of pluripotent tissue morphogenesis. *Stem Cell Reports*, *16*(5), 1182–1196. https://doi.org/10.1016/j.stemcr.2020.09.004

Paca, A., Séguin, C. A., Clements, M., Ryczko, M., Rossant, J., Rodriguez, T. A., & Kunath, T. (2012). BMP signaling induces visceral endoderm differentiation of XEN cells and parietal endoderm. *Developmental Biology*, *361*(1), 90–102. https://doi.org/10.1016/j.ydbio.2011.10.013

Papanayotou, C., & Collignon, J. (2014). Activin/Nodal signalling before implantation: setting the stage for embryo patterning. *Philosophical Transactions of the Royal Society of London. Series B, Biological Sciences*, *369*(1657). https://doi.org/10.1098/rstb.2013.0539

Porcher, A., & Dostatni, N. (2010). The Bicoid Morphogen System. *Current Biology*, *20*(5), R249–R254. https://doi.org/10.1016/j.cub.2010.01.026

Preibisch, S., Saalfeld, S., & Tomancak, P. (2009). Globally optimal stitching of tiled 3D microscopic image

acquisitions. *Bioinformatics (Oxford, England)*, *25*(11), 1463–1465. https://doi.org/10.1093/bioinformatics/btp184

Proffitt, K. D., & Virshup, D. M. (2012). Precise Regulation of Porcupine Activity Is Required for Physiological Wnt Signaling. *Journal of Biological Chemistry*, *287*(41), 34167–34178. https://doi.org/10.1074/jbc.M112.381970

Raina, D., Bahadori, A., Stanoev, A., Protzek, M., Koseska, A., & Schroter, C. (2021). Cell-cell communication through FGF4 generates and maintains robust proportions of differentiated cell types in embryonic stem cells. *Development (Cambridge)*, *148*(21), dev199926. https://doi.org/10.1242/dev.199926

Ran, F. A., Hsu, P. D., Wright, J., Agarwala, V., Scott, D. A., & Zhang, F. (2013). Genome engineering using the CRISPR-Cas9 system. *Nature Protocols*, *8*(11), 2281. https://doi.org/10.1038/NPROT.2013.143

Rivera-Pérez, J. A., & Hadjantonakis, A.-K. (2014). The Dynamics of Morphogenesis in the Early Mouse Embryo. *Cold Spring Harbor Perspectives in Biology*, *7*(11), a015867. https://doi.org/10.1101/cshperspect.a015867

Roberts, R. M., Ezashi, T., Temple, J., Owen, J. R., Soncin, F., & Parast, M. M. (2022). The role of BMP4 signaling in trophoblast emergence from pluripotency. *Cellular and Molecular Life Sciences*, *79*(8), 447. https://doi.org/10.1007/s00018-022-04478-w

Robertson, E. J. (2014). Dose-dependent Nodal/Smad signals pattern the early mouse embryo. *Seminars in Cell & Developmental Biology*, *32*, 73–79. https://doi.org/10.1016/J.SEMCDB.2014.03.028

Rodriguez, T. A. (2005). Induction and migration of the anterior visceral endoderm is regulated by the extra-embryonic ectoderm. *Development*, *132*(11), 2513–2520. https://doi.org/10.1242/dev.01847

Rossant, J., & Tam, P. P. L. (2021). Opportunities and challenges with stem cell-based embryo models. *Stem Cell Reports*, *16*(5), 1031–1038. https://doi.org/10.1016/j.stemcr.2021.02.002

Rossant, J., & Tam, P. P. L. (2022). Early human embryonic development: Blastocyst formation to gastrulation. *Developmental Cell*, *57*(2), 152–165. https://doi.org/10.1016/j.devcel.2021.12.022

Saiz, N., & Plusa, B. (2013). Early cell fate decisions in the mouse embryo. *REPRODUCTION*, *145*(3), R65–R80. https://doi.org/10.1530/REP-12-0381

Sanson, K. R., Hanna, R. E., Hegde, M., Donovan, K. F., Strand, C., Sullender, M. E., Vaimberg, E. W., Goodale, A., Root, D. E., Piccioni, F., & Doench, J. G. (2018). Optimized libraries for CRISPR-Cas9 genetic screens with multiple modalities. *Nature Communications*, *9*(1), 5416. https://doi.org/10.1038/s41467-018-07901-8

Schier, A. F. (2003). Nodal Signaling in Vertebrate Development. *Annual Review of Cell and Developmental Biology*, *19*(1), 589–621. https://doi.org/10.1146/annurev.cellbio.19.041603.094522

Schmidt, U., Weigert, M., Broaddus, C., & Myers, G. (2018). *Cell Detection with Star-Convex Polygons* (pp. 265–273). https://doi.org/10.1007/978-3-030-00934-2_30

Schumacher, S., Fernkorn, M., Marten, M., Kim, Y. S., Bedzhov, I., & Schröter, C. (2023). Tissue-intrinsic Wnt signals antagonize Nodal-driven AVE differentiation. *BioRxiv*, 2023.05.19.541432. https://doi.org/10.1101/2023.05.19.541432

Sekine, R., Shibata, T., & Ebisuya, M. (2018). Synthetic mammalian pattern formation driven by differential diffusivity of Nodal and Lefty. *Nature Communications*, *9*(1), 5456. https://doi.org/10.1038/s41467-018-07847-x

Simon, C. S., Hadjantonakis, A.-K., & Schröter, C. (2018). Making lineage decisions with biological noise: Lessons from the early mouse embryo. *Wiley Interdisciplinary Reviews. Developmental Biology*, *7*(4), e319. https://doi.org/10.1002/wdev.319

Smith, E. R. A. N., & Fox, R. L. (2001). The Electoral Fortunes of Women Candidates for Congress. *Political Research*

Quarterly, *54*(1), 205. https://doi.org/10.2307/449215

Sozen, B., Amadei, G., Cox, A., Wang, R., Na, E., Czukiewska, S., Chappell, L., Voet, T., Michel, G., Jing, N., Glover, D. M., & Zernicka-Goetz, M. (2018). Self-assembly of embryonic and two extra-embryonic stem cell types into gastrulating embryo-like structures. *Nature Cell Biology*, *20*(8), 979–989. https://doi.org/10.1038/s41556-018-0147-7

Srinivas, S., Rodriguez, T., Clements, M., Smith, J. C., & Beddington, R. S. P. (2004). Active cell migration drives the unilateral movements of the anterior visceral endoderm. *Development*, *131*(5), 1157–1164. https://doi.org/10.1242/dev.01005

Stamos, J. L., & Weis, W. I. (2013). The β-catenin destruction complex. *Cold Spring Harbor Perspectives in Biology*, *5*(1), a007898. https://doi.org/10.1101/cshperspect.a007898

Stower, M. J., & Srinivas, S. (2018). The Head's Tale: Anterior-Posterior Axis Formation in the Mouse Embryo. *Current Topics in Developmental Biology*, *128*, 365–390. https://doi.org/10.1016/bs.ctdb.2017.11.003

Sullivan, A. E., & Santos, S. D. (2023). The ever-growing world of gastruloids: autogenous models of mammalian embryogenesis. *Current Opinion in Genetics & Development*, *82*, 102102. https://doi.org/10.1016/j.gde.2023.102102

Takahashi, K., & Yamanaka, S. (2006). Induction of Pluripotent Stem Cells from Mouse Embryonic and Adult Fibroblast Cultures by Defined Factors. *Cell*, *126*(4), 663–676. https://doi.org/10.1016/j.cell.2006.07.024

Takaoka, K., Yamamoto, M., & Hamada, H. (2011). Origin and role of distal visceral endoderm, a group of cells that determines anterior–posterior polarity of the mouse embryo. *Nature Cell Biology*, *13*(7), 743–752. https://doi.org/10.1038/ncb2251

Tarazi, S., Aguilera-Castrejon, A., Joubran, C., Ghanem, N., Ashouokhi, S., Roncato, F., Wildschutz, E., Haddad, M., Oldak, B., Gomez-Cesar, E., Livnat, N., Viukov, S., Lokshtanov, D., Naveh-Tassa, S., Rose, M., Hanna, S., Raanan, C., Brenner, O., Kedmi, M., … Hanna, J. H. (2022). Post-gastrulation synthetic embryos generated ex utero from mouse naive ESCs. *Cell*, *185*(18), 3290-3306.e25. https://doi.org/10.1016/J.CELL.2022.07.028

Thomas, P., & Beddington, R. (1996). Anterior primitive endoderm may be responsible for patterning the anterior neural plate in the mouse embryo. *Current Biology*, *6*(11), 1487–1496. https://doi.org/10.1016/S0960-9822(96)00753-1

Thowfeequ, S., Fiorentino, J., Hu, D., Solovey, M., Ruane, S., Whitehead, M., Vanhaesebroeck, B., Scialdone, A., & Srinivas, S. (2021). Characterisation of the transcriptional dynamics underpinning the function, fate, and migration of the mouse Anterior Visceral Endoderm. *BioRxiv*, 2021.06.25.449902. https://doi.org/10.1101/2021.06.25.449902

Tkačik, G., & Gregor, T. (2021). The many bits of positional information. *Development*, *148*(2). https://doi.org/10.1242/dev.176065

Trichas, G., Joyce, B., Crompton, L. A., Wilkins, V., Clements, M., Tada, M., Rodriguez, T. A., & Srinivas, S. (2011). Nodal Dependent Differential Localisation of Dishevelled-2 Demarcates Regions of Differing Cell Behaviour in the Visceral Endoderm. *PLoS Biology*, *9*(2), e1001019. https://doi.org/10.1371/journal.pbio.1001019

Tsakiridis, A., Huang, Y., Blin, G., Skylaki, S., Wymeersch, F., Osorno, R., Economou, C., Karagianni, E., Zhao, S., Lowell, S., & Wilson, V. (2014). Distinct Wnt-driven primitive streak-like populations reflect *in vivo* lineage precursors. *Development*, *141*(6), 1209–1221. https://doi.org/10.1242/dev.101014

Turing, A. (1952). The chemical basis of morphogenesis. *Philosophical Transactions of the Royal Society of London. Series B, Biological Sciences*, *237*(641), 37–72. https://doi.org/10.1098/rstb.1952.0012

Turlier, H., & Maître, J.-L. (2015). Mechanics of tissue compaction. *Seminars in Cell & Developmental Biology*, *47–48*, 110–117. https://doi.org/10.1016/j.semcdb.2015.08.001

Valenta, T., Hausmann, G., & Basler, K. (2012). The many faces and functions of β-catenin. *The EMBO Journal*, *31*(12), 2714–2736. https://doi.org/10.1038/emboj.2012.150

van der Wal, T., & van Amerongen, R. (2020). Walking the tight wire between cell adhesion and WNT signalling: a balancing act for β-catenin. *Open Biology*, *10*(12). https://doi.org/10.1098/rsob.200267

Vassalli, A., Matzuk, M. M., Gardner, H. A., Lee, K. F., & Jaenisch, R. (1994). Activin/inhibin beta B subunit gene disruption leads to defects in eyelid development and female reproduction. *Genes & Development*, *8*(4), 414–427. https://doi.org/10.1101/gad.8.4.414

Vrij, E. J., Scholte op Reimer, Y. S., Fuentes, L. R., Guerreiro, I. M., Holzmann, V., Aldeguer, J. F., Sestini, G., Koo, B.-K., Kind, J., van Blitterswijk, C. A., & Rivron, N. C. (2022). A pendulum of induction between the epiblast and extra-embryonic endoderm supports post-implantation progression. *Development*, *149*(20). https://doi.org/10.1242/dev.192310

Waldrip, W. R., Bikoff, E. K., Hoodless, P. A., Wrana, J. L., & Robertson, E. J. (1998). Smad2 Signaling in Extraembryonic Tissues Determines Anterior-Posterior Polarity of the Early Mouse Embryo. *Cell*, *92*(6), 797–808. https://doi.org/10.1016/S0092-8674(00)81407-5

Wamaitha, S. E., del Valle, I., Cho, L. T. Y., Wei, Y., Fogarty, N. M. E., Blakeley, P., Sherwood, R. I., Ji, H., & Niakan, K. K. (2015). Gata6 potently initiates reprograming of pluripotent and differentiated cells to extraembryonic endoderm stem cells. *Genes & Development*, *29*(12), 1239–1255. https://doi.org/10.1101/gad.257071.114

Wang, S., Garcia-Ojalvo, J., & Elowitz, M. B. (2022). Periodic spatial patterning with a single morphogen. *Cell Systems*, *13*(12), 1033-1047.e7. https://doi.org/10.1016/J.CELS.2022.11.001

Wang, W., Lin, C., Lu, D., Ning, Z., Cox, T., Melvin, D., Wang, X., Bradley, A., & Liu, P. (2008). Chromosomal transposition of PiggyBac in mouse embryonic stem cells. *Proceedings of the National Academy of Sciences*, *105*(27), 9290–9295. https://doi.org/10.1073/pnas.0801017105

Weatherbee, B. A. T., Gantner, C. W., Iwamoto-Stohl, L. K., Daza, R. M., Hamazaki, N., Shendure, J., & Zernicka-Goetz, M. (2023). Pluripotent stem cell-derived model of the post-implantation human embryo. *Nature*, *622*(7983), 584–593. https://doi.org/10.1038/s41586-023-06368-y

Wilder, P. J., Kelly, D., Brigman, K., Peterson, C. L., Nowling, T., Gao, Q. S., McComb, R. D., Capecchi, M. R., & Rizzino, A. (1997). Inactivation of the FGF-4 gene in embryonic stem cells alters the growth and/or the survival of their early differentiated progeny. *Developmental Biology*, *192*(2), 614–629. https://doi.org/10.1006/dbio.1997.8777

Willert, K., Brown, J. D., Danenberg, E., Duncan, A. W., Weissman, I. L., Reya, T., Yates, J. R., & Nusse, R. (2003). Wnt proteins are lipid-modified and can act as stem cell growth factors. *Nature*, *423*(6938), 448–452. https://doi.org/10.1038/nature01611

Winnier, G., Blessing, M., Labosky, P. A., & Hogan, B. L. (1995). Bone morphogenetic protein-4 is required for mesoderm formation and patterning in the mouse. *Genes & Development*, *9*(17), 2105–2116. https://doi.org/10.1101/gad.9.17.2105

Wolf, F. A., Angerer, P., & Theis, F. J. (2018). SCANPY: large-scale single-cell gene expression data analysis. *Genome Biology*, *19*(1), 15. https://doi.org/10.1186/s13059-017-1382-0

Wolpert, L. (1969). Positional information and the spatial pattern of cellular differentiation. *Journal of Theoretical Biology*, *25*(1), 1–47. https://doi.org/10.1016/S0022-5193(69)80016-0

Wolpert, L., Tickle, C., Martinez Arias, A., Lawrence, P., & Locke, J. (2019). *Principles of development* (Sixth edit). Oxford University Press.

Yamamoto, M., Beppu, H., Takaoka, K., Meno, C., Li, E., Miyazono, K., & Hamada, H. (2009). Antagonism between Smad1 and Smad2 signaling determines the site of distal visceral endoderm formation in the mouse

embryo. *Journal of Cell Biology*, *184*(2), 323–334. https://doi.org/10.1083/jcb.200808044

Yamamoto, M., Saijoh, Y., Perea-Gomez, A., Shawlot, W., Behringer, R. R., Ang, S.-L., Hamada, H., & Meno, C. (2004). Nodal antagonists regulate formation of the anteroposterior axis of the mouse embryo. *Nature*, *428*(6981), 387–392. https://doi.org/10.1038/nature02418

Ying, Q.-L., Wray, J., Nichols, J., Batlle-Morera, L., Doble, B., Woodgett, J., Cohen, P., & Smith, A. (2008). The ground state of embryonic stem cell self-renewal. *Nature*, *453*(7194), 519–523. https://doi.org/10.1038/nature06968

Zagris, N. (2022). Aristotle (384-322 BC): the beginnings of Embryology. *The International Journal of Developmental Biology*, *66*(1-2–3), 5–8. https://doi.org/10.1387/ijdb.220040nz

Zhang, S., Chen, T., Chen, N., Gao, D., Shi, B., Kong, S., West, R. C., Yuan, Y., Zhi, M., Wei, Q., Xiang, J., Mu, H., Yue, L., Lei, X., Wang, X., Zhong, L., Liang, H., Cao, S., Belmonte, J. C. I., … Han, J. (2019). Implantation initiation of self-assembled embryo-like structures generated using three types of mouse blastocyst-derived stem cells. *Nature Communications*, *10*(1), 496. https://doi.org/10.1038/s41467-019-08378-9

Zhu, Q., Ge, J., Liu, Y., Xu, J.-W., Yan, S., & Zhou, F. (2023). Decoding anterior-posterior axis emergence among mouse, monkey, and human embryos. *Developmental Cell*, *58*(1), 63-79.e4. https://doi.org/10.1016/j.devcel.2022.12.004

6 Acknowledgements

This journey would not have been possible without the unwavering support, guidance, and encouragement of my mentor and advisor Dr. Christan Schröter. I'd like to thank you for believing in me, convincing me of the potential of the BELA project and pushing it to a limit I've never dreamt of.

I would like to thank Prof. Dr. Philippe Bastiaens for having me in this incredible department with these incredible people. Thank you for providing the endless resources, scientific exchanges on numerous meetings and challenging discussions that helped me and my project grow.
A thanks also to Dr. Peter Bieling and to my TAC members Prof. Dr. Andreas Musacchio and Dr. Vikas Trivedi for your invaluable contributions and advice throughout the project.

To Christa and Lucia, I'd like to thank you for your immense work with the IMPRS. I totally appreciated the enormous number of offers for courses to shape my skills and your endless support in really everything. Your offered helped without the necessity asking for it.

A special thanks to all members of department II. Thanks for keeping the department running and flourishing, for all your support and scientific input, your kindness and encouragement and for making my time in this department so memorable. A special thanks for all the cakes and sweets from your home countries and holidays, I really enjoyed them. I'd also like to thank the people for giving me the best of lunch breaks with really abstruse conversations, much laughter and the weirdest stories I've ever heard of.

To my beloved SchröterGroup. I wish to thank all of the students, Marcel, Sarah and Pauliine and Pablo, for their contributions to my project and their enrichment for the team. To all members and previous members of the SchröterLab Dhruv, Fiorella, Marina, Michelle, Max, Julia: you are simply the best. It has been a pleasure working alongside you. Thanks for creating the best work atmosphere I will probably ever have and for making the office a safe space for the weirdest of ideas, the free expression of creativity and the courage to addiction. Michelle, Max and Julia thank you for your friendships and all the great moments we shared together. I hope they will never TGA. Michelle I'd like to thank you especially, for teaching me basically everything I know in the lab and for your endless patience especially with FACS experiment.

To my dearest friends, and especially my Fabian group Kristina, Mareke, Sofie and Wiebke. Thanks for your friendship, your support and encouragement, and countless distractions from my work that gave the necessary balance to my life.

To Kevin – thank you for being by my side during this journey. Your keen eye for design and your insights in illustrations has greatly enhanced the visual appeal of this thesis. It simply wouldn't be the same without your contributions. Thank you for always lending me your ear and showing immense patience during the most stressful moments. Your support, particularly during the thesis writing phase, enabled me to concentrate fully on my work by taking care of other responsibilities.

Zum Schluss möchte ich noch meiner ganzen Familie danken und besonders meinen Eltern, die mir diesen Weg ermöglicht haben vom Beginn meines Studiums bis zum Abschluss meiner Promotion. Danke, dass ihr immer hinter mir standet. Und damit ist meine Doktorarbeit fertig.

Eidesstattliche Versicherung (Affidavit)

Schumacher, Sina
Name, Vorname
(Surname, first name)

224288
Matrikel-Nr.
(Enrolment number)

Belehrung:

Wer vorsätzlich gegen eine die Täuschung über Prüfungsleistungen betreffende Regelung einer Hochschulprüfungsordnung verstößt, handelt ordnungswidrig. Die Ordnungswidrigkeit kann mit einer Geldbuße von bis zu 50.000,00 € geahndet werden. Zuständige Verwaltungsbehörde für die Verfolgung und Ahndung von Ordnungswidrigkeiten ist der Kanzler/die Kanzlerin der Technischen Universität Dortmund. Im Falle eines mehrfachen oder sonstigen schwerwiegenden Täuschungsversuches kann der Prüfling zudem exmatrikuliert werden, § 63 Abs. 5 Hochschulgesetz NRW.

Die Abgabe einer falschen Versicherung an Eides statt ist strafbar.

Wer vorsätzlich eine falsche Versicherung an Eides statt abgibt, kann mit einer Freiheitsstrafe bis zu drei Jahren oder mit Geldstrafe bestraft werden, § 156 StGB. Die fahrlässige Abgabe einer falschen Versicherung an Eides statt kann mit einer Freiheitsstrafe bis zu einem Jahr oder Geldstrafe bestraft werden, § 161 StGB.

Die oben stehende Belehrung habe ich zur Kenntnis genommen:

Official notification:

Any person who intentionally breaches any regulation of university examination regulations relating to deception in examination performance is acting improperly. This offence can be punished with a fine of up to EUR 50,000.00. The competent administrative authority for the pursuit and prosecution of offences of this type is the chancellor of the TU Dortmund University. In the case of multiple or other serious attempts at deception, the candidate can also be unenrolled, Section 63, paragraph 5 of the Universities Act of North Rhine-Westphalia.

The submission of a false affidavit is punishable.

Any person who intentionally submits a false affidavit can be punished with a prison sentence of up to three years or a fine, Section 156 of the Criminal Code. The negligent submission of a false affidavit can be punished with a prison sentence of up to one year or a fine, Section 161 of the Criminal Code.

I have taken note of the above official notification.

Dortmund,03.04.2024
Ort, Datum
(Place, date)

Unterschrift
(Signature)

Titel der Dissertation:
(Title of the thesis):

Tissue-intrinsic control of AVE differentiation in stem cell models

Ich versichere hiermit an Eides statt, dass ich die vorliegende Dissertation mit dem Titel selbstständig und ohne unzulässige fremde Hilfe angefertigt habe. Ich habe keine anderen als die angegebenen Quellen und Hilfsmittel benutzt sowie wörtliche und sinngemäße Zitate kenntlich gemacht.
Die Arbeit hat in gegenwärtiger oder in einer anderen Fassung weder der TU Dortmund noch einer anderen Hochschule im Zusammenhang mit einer staatlichen oder akademischen Prüfung vorgelegen.

I hereby swear that I have completed the present dissertation independently and without inadmissible external support. I have not used any sources or tools other than those indicated and have identified literal and analogous quotations.

The thesis in its current version or another version has not been presented to the TU Dortmund University or another university in connection with a state or academic examination.*

*Please be aware that solely the German version of the affidavit ("Eidesstattliche Versicherung") for the PhD thesis is the official and legally binding version.

Dortmund, 03.04.2024
Ort, Datum
(Place, date)

Unterschrift
(Signature)